

The 17th Nano Bio Info Chemistry Symposium

The 10th Japanese–Russian Seminar on Chemical Physics
of Molecules and Polyfunctional Materials

December 9-11, 2020

The 17th Nano Bio Info Chemistry Symposium

The 10th Japanese-Russian Seminar on Chemical Physics of Molecules and Polyfunctional Materials

Overview: The 17th Nano Bio Info Chemistry Symposium and The 10th Japanese-Russian Seminar on Chemical Physics of Molecules and Polyfunctional Materials will be held online, December 9-11, 2020.

Notice: Due to the outbreak of COVID-19 and for the safety of our participants, this symposium has been changed to Online Conference.

The online Symposium consists of two parts:

- 1) Oral Presentation with a pre-recorded video (mp4 files) or real time presentation via Zoom
- 2) Discussion via Zoom

Organizers

The Chemical Society of Nano Bio Info
Physics Faculty of Orenburg State University

Co-organizers

The Chugoku Shikoku Branch, The Chemical Society of Japan
The Chugoku Shikoku Branch, The Society of Synthetic Organic Chemistry,
Japan
The Chugoku Shikoku Branch, The Japan Society for Analytical Chemistry
The Chugoku Shikoku Branch, The Spectroscopical Society of Japan

Contributions

The Hiroshima Chemistry Alumni Association
Micron Technology Foundation, Inc.

2020 December 9 th Wednesday		
Japan Time	Russian Time	
12:45:00	08:45:00	Online Site Open
13:00:00	09:00:00	Opening Address
Chairman: Katsuya INOUE		
13:10:00	09:10:00	Vitaly BERDINSKIY
		Hyperfine interactions of magnetic isotope nuclei in molecules and molecular complexes
13:45:00	09:45:00	Jun MANABE
		Band-filling control of [Ni(dmit) ₂] salt by the solid state Ion exchange function ☆
14:00:00	10:00:00	Anton BAKAEV
		Problems and prospects of using positron emission tomography ☆
14:15:00	10:15:00	Break
Chairman: Michael KUCHERENKKO		
14:30:00	10:30:00	Alexander RUSINOV
		Effect of plasmonic nanoparticles with various surface charge on the nonlinear absorption of methylene blue solutions
14:45:00	10:45:00	Ildar ALIMBEKOV
		Delayed fluorescence of molecules on the surface of ferroplasmonic nanoparticles ☆
15:00:00	11:00:00	Shogo MEIJI
		Surface-enhanced infrared absorption spectroscopy of lanthanide complexes with N-donor or O-donor ligands on Au surface ☆
15:15:00	11:15:00	Break
Chairman: Aik NIKIYAN		
15:30:00	11:30:00	Masayuki MORIE
		Guest Binding Behaviors of the Calix[4]arene Based Triple-Stranded Helicate in Water ☆
15:45:00	11:45:00	Azamat ISHEMGULOV
		Inactivation of bacteria with shock acoustic waves generated by thermal sensitizers ★
16:00:00	12:00:00	Quy Dat LUONG
		Laser-induced crystallization of amino acids at the chiral ionic liquid/water interface ☆
16:15:00	12:15:00	

IL: Invited Lecture (35 min including Q&A, Zoom)

b: Oral presentation b (15 min including Q&A, Zoom)

★☆☆: Candidate to the student and young scientist award

2020 December 10 th Thursday		
Japan Time	Russian Time	
13:00:00	09:00:00	Online Site Open
Chairman: Katsuya INOUE		
13:15:00	09:15:00	2A1b Marsel ARIFULLIN Pulse spin manipulations with high spin ions for quantum computing
13:30:00	09:30:00	2A2b Ikuya MATSUMOTO Aggregation and disaggregation behavior of nanographene ☆
13:45:00	09:45:00	2A3b Alexander YUDIN Determination of the phase composition of bentonite powders used for the sorption of nickel ions ☆
14:00:00	10:00:00	2A4b Akane KATO Steric effect by substituents on spin state of iron(II) assembled complexes using low symmetry bis(4-pyridyl)benzene derivatives ☆
14:15:00	10:15:00	Break
Chairman: Ulyana LETUTA		
14:35:00	10:35:00	2B1b Shozo MATSUMAE Synthesis and characterization of a digallane gold complex with a 12-electron auride center ☆
14:50:00	10:50:00	2B2b Dmitrii TSIURKO Generation and propagation of acoustic waves in condensed matter ☆
15:05:00	11:05:00	2B3b Masaya YOSHIDA Self-assembling behaviors of platinum(II) complexes possessing hydrophilic triethylene glycol chains ☆
15:20:00	11:20:00	2B4b Nikita KRUCHININ Molecular dynamic simulation of the conformational structure rearrangement of polyampholyte polypeptides on the surface of a metal nanoparticle in an ultrahigh-frequency electric field
15:35:00	11:35:00	Break
Chairman: Goulven COSQUER		
15:50:00	11:50:00	2C1b Airi OGURI Attempts to synthesize antiaromatic σ -dimer: Silyl group conversion of cobalt complex ☆
16:05:00	12:05:00	2C2IL Michael KUCHERENKO Radiation and radiationless molecular processes in a near field of 2D-gratings with plasmonic nanoelements
16:40:00	12:40:00	

IL: Invited Lecture (35 min including Q&A, Zoom)

b: Oral presentation b (15 min including Q&A, Zoom)

★☆: Candidate to the student and young scientist award

2020 December 11th Friday

Japan Time	Russian Time		
12:45:00	08:45:00	Online Site Open	
		Chairman: Satoru MURAMATSU	
13:00:00	09:00:00	3A1b	Olga KANYGINA
			Microwave activation of phyllosilicate adsorption on kaolin clays
13:15:00	09:15:00	3A2b	Hike NIKIYAN
			Morphology and biological activity of Co and Zn oxide nanoparticles and ferrates
13:30:00	09:30:00	3A3b	Yuki TANIMOTO
			Rate coefficients and branching ratio for quenching of O(2p ³ 3p ³ P ₁) by collisions with He ☆
13:45:00	09:45:00	3A4b	Ulyana G. LETUTA
			Magnetic-dependent metabolism of bacteria E. coli
14:00:00	10:00:00	3A5b	Jialun LI
			Transition metal-free borylation reaction using 1,8-diaminonaphthalene-substituted borane [H-B(dan)] as a B(dan) electrophile ☆
14:15:00	10:15:00	Break	
		Chairman: Vitaliy BERDINSKIY	
14:30:00	10:30:00	3B1a	Shin-nosuke KINOSHITA
			Experimental and theoretical study on the nonradiative decay process of cinnamates aimed for the development of effective sunscreen reagents ☆
14:50:00	10:50:00	3B2b	Sergey PENKOV
			Spin-dependent quenching of triplet excitons by doublet centers in a nanoparticle ★
15:05:00	11:05:00	3B3b	Mikinao KOISHI
			Direct Suzuki–Miyaura Cross-Coupling of 1,8-Diaminonaphthalene (dan)-Substituted Organoboron Compounds ☆
15:20:00	11:20:00	3B4b	Tatsuya KANASAKI
			Internal Selective Borylations of Terminal Alkynes with Lewis Acidity-Decreased Boron Reagents ☆
15:35:00	11:35:00	Closing of the Symposium	
15:50:00	11:50:00		

a: Oral presentation a (20 min including Q&A, Zoom)

b: Oral presentation b (15 min including Q&A, Zoom)

★☆☆: Candidate to the student and young scientist award

Hyperfine interactions of magnetic isotope nuclei in molecules and molecular complexes

Kaepkulova Elina, Berdinskiy Vitaly

Department of Physics, Orenburg University, Russia

E-mail: 79378363895@mail.ru

Stable magnetic isotopes-isotopes with nuclear spin and nuclear magnetic moment, for example, ^{13}C , ^{25}Mg , ^{29}Si , ^{31}P , ^{67}Zn , etc., allow recording nuclear magnetic resonance (NMR) spectra and are used in radio spectroscopy. In stable and free radicals – "fragments" of molecules – the magnetic moments of atomic nuclei interact with the magnetic moments of unpaired electrons. This interaction is called the hyperfine interaction (STV). It leads to splitting of the electron paramagnetic resonance (EPR) lines and makes it possible to identify the spatial and electronic structure of radicals [1]. In radical pairs and ion-radical pairs, STV induces singlet-triplet conversion, which changes the reactivity of radicals with respect to cellular and extracellular recombination in liquids [2]. Subsequently, the influence of the magnetic moments of the atomic nuclei of the isotopes ^{25}Mg , ^{67}Zn , and others was discovered and proved. on the rate of enzymatic processes *in vitro* and *in vivo* [3-5].

The spin Hamiltonian of hyperfine interactions \hat{H}_{cn} assumes the interaction of the nuclear spin I with only one electron spin $S = 1/2$ with the interaction constant a

$$\hat{H}_{\text{cn}} = a \cdot \hat{S} \cdot \hat{I}$$

At first glance, this form of the Hamiltonian \hat{H} does not allow hyperfine interactions in diamagnetic molecules with filled electron shells and with total electron spin $S = S_1 + S_2 = 0$. However, the antisymmetry of the total wave function $\Psi(r_1, r_2)$ of diamagnetic molecules requires a separate description of the interactions of individual electrons with the nuclear spin I . The "full" Hamiltonian of hyperfine interactions must include both spin and space variables r_1 and r_2 and initially have the form [1]

$$\hat{H} = \left(\frac{8\pi}{3} \right) g_n \beta_n g_e \beta_e [\vec{S}_1 \delta(\vec{r}_1 - \vec{r}_A) + \vec{S}_2 \delta(\vec{r}_2 - \vec{r}_A)] \quad (1)$$

Here r_A -coordinates of the core of the magnetic isotope, $\delta(r_i - r_A)$ - δ -function. Calculations of matrix elements of the Hamiltonian (1)

$$\langle \Psi_T(r_1, r_2) | \hat{H} | \Psi_S(r_1, r_2) \rangle$$

with the spatial wave functions of the singlet

$$\Psi_S(r_1, r_2) = 2^{-1/2} \varphi_1(r_1) \varphi_1(r_2) |S\rangle$$

and triplet states

$$\Psi_T(r_1, r_2) = 2^{-1/2} [\varphi_1(r_1) \varphi_2(r_2) - \varphi_2(r_1) \varphi_1(r_2)] |T_{\pm 0}\rangle$$

prove that the hyperfine interaction can transfer the system from the singlet to the triplet state, and the spin Hamiltonian must have the form

$$\hat{H}_{\text{CTB}} = a_1 (\hat{S}_1 - \hat{S}_2) \hat{I}, \quad (2)$$

here a_1 is the new HFI constant

$$a_1 = (8\pi/3)g\beta g_n \beta_n \varphi_u(r_A) \varphi_g(r_A).$$

It is proved that the spin Hamiltonian of the hyperfine interaction (2) is able to "mix" singlet and triplet states in diamagnetic molecules and molecular complexes and induce singlet triplet conversion in the active centers of enzymes in magnetic fields corresponding to the quasi-level crossing of triplet and singlet terms.

- [1] Kerrington A., Mc-Lachlan E. Magnetic resonance and its application in chemistry. – Moscow. Mir, 1969. – 448 p.
- [2] Buchachenko A.L. Beauty and Fascination of Science.– Singapore. Springer Nature Ltd, 2020.–188 p
- [3] Buchachenko A.L. Magnetic Isotope Effect in Chemistry and Biochemistry. – New York: Nova Science, 2009. – 149 p.
- [4] Letuta U.G., Berdinskiy V.L. Magnetosensitivity of bacteria E. coli: Magnetic isotope and magnetic field effects // Bioelectromagnetics. – 2017. - № 38- P. 581–591.
- [5] Magnetic isotope effect of magnesium ²⁵Mg on E. coli resistance to antibiotics / U.G. Letuta, A.S. Vekker, T.A. Kornilova et. al. // Doklady Biochem. Biophys. – 2016. - № 469. -C. 281–283.

Band-filling control of [Ni(dmit)₂] salt by the solid state ion exchange function

Jun Manabe,¹ Katsuya Ichihashi,¹ Daisuke Konno,¹ Goulven Cosquer,^{1,2}
Katsuya Inoue,^{1,2,3} Tomoyuki Akutagawa,⁴ Takayoshi Nakamura,⁵
Sadafumi Nishihara^{1,2,3,6}

¹ Department of Chemistry, Graduate School of Science, Hiroshima University

² Chirality Research Center (CResCent), Hiroshima University

³ Institute for Advanced Materials Research, Hiroshima University

⁴ Institute of Multidisciplinary Research for Advanced Materials, Tohoku University

⁵ Research Institute for Electronic Science, Hokkaido University

⁶ JST, PRESTO

In recent years, organic semiconductors have been expected to be used in light and flexible electronic devices. Although the electronic state of the semiconductor can be controlled by carrier density, distortions of the crystal structure are often caused by carrier doping due to the small crystallization energy in molecular crystals. Thus, we aimed to achieve the control of the band-filling by using solid state ion exchange function in the crystal, instead of the traditional method.

For achieving this purpose, we focused on the molecular crystal $\text{Li}_2([\text{18}]\text{crown-6})_3[\text{Ni}(\text{dmit})_2]_2(\text{H}_2\text{O})_4$ (**Li salt**, Figure 1), which contain ion channel composed of Li^+ ion, [18]crown-6, and crystalline water molecules. Li^+ ion conduction in this ion channels was observed.^[1] When the crystals of **Li salt** was soaked in a KCl aqueous solution, the complete ion exchange of Li^+ by K^+ ion occurred, maintaining crystallinity.^[2] In this study, we aimed to control the electronic state of **Li salt** by utilizing the solid-state ion exchange function. As example, introduction of Cu^{2+} ion in the crystal through the ion channel can induce an electron transfer from $[\text{Ni}(\text{dmit})_2]^-$ to Cu^{2+} . This exchange decreased the electrical resistivity of the crystal by six orders of magnitude (**Li**→**Cu salt**, Figure 2). Furthermore, control of the band filling in **Li salt** by introduction of Cu^{2+} and Ca^{2+} ions, which do not cause electron transfer, at the same time to the crystals (**Li**→**CuCa salt**) was investigated. The resistivity of this sample exhibited a lower value than **Li**→**Cu salt**. In this presentation, the physical properties will be discussed in detail.

[1] S. Nishihara *et al.*, *Chem. Mater.* **2018**, 30, 7130.

[2] S. Nishihara *et al.*, *Angew. Chem. Int. Ed.* **2019**, 58, 4169.

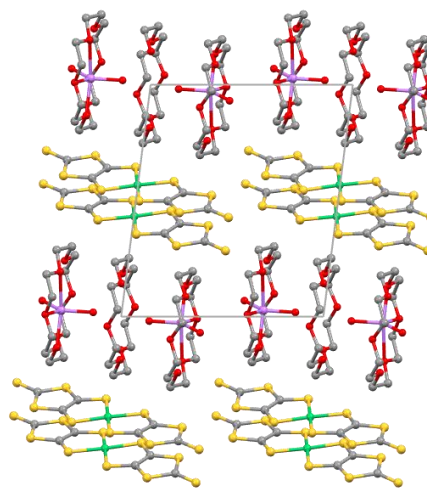


Figure 1. The crystal structure of **Li salt** viewed along the *a*-axis.

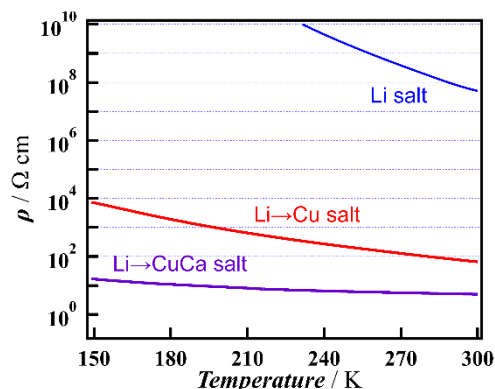


Figure 2. Temperature dependence of the resistivities of **Li salt**, **Li**→**Cu salt** and **Li**→**CuCa salt**.

1A3b

Problems and prospects of using positron emission tomography

Bakaev Anton, Strelalovskaya Alevtina, Baranova_Oksana_
Orenburg University, Russia

Positron emission tomography is currently the most accurate radionuclide method for studying internal organs of a person and one of the most informative methods for early diagnosis of oncological, neurological and cardiological diseases. The Orenburg region is ranked 6th in terms of cancer in the Volga Federal district and 21st in Russia. According to the Association of health organizers in Oncology, in the first half of 2019, the death rate from cancer in Russia was 204.5 people per 100 thousand population. The fact that the rate of cancer-related deaths decreased by 3.9% in the first half of 2020 indicates that the Ministry of health's "Fight against cancer" project approved in 2019 has been successfully implemented, but there is still a need to solve many problems, primarily by updating and expanding the fleet of medical equipment in regional health institutions.

Keywords: PET, Oncology, radiopharmaceuticals, diagnostics, radiology

The method of positron emission tomography is known as two-photon emission tomography, since it is based on the registration of a pair of gamma quanta created during the annihilation of positrons with electrons [3]. In turn, positrons are created during the beta decay of a special radionuclide that is previously introduced into the patient's body.

Positron emission tomography allows you to track the distribution of biologically active compounds in the body using radiopharmaceuticals, which, in turn, make it possible to study a variety of processes: metabolism, gene expression, substance transport, and many others.

The procedure uses modern equipment that increases its productivity. The advantages of the method include [4]:

- 1) increased research accuracy;
- 2) ability to replace several different diagnostics;
- 3) non-invasiveness;
- 4) the absence of pain;
- 5) ability to examine multiple organs and systems in a single procedure;
- 6) the absence of harmful factors.

The main task of the diagnostic method is to obtain an image in color, so that you can clearly see any change.

There are several varieties of such drugs, presented in detail in figure 1.

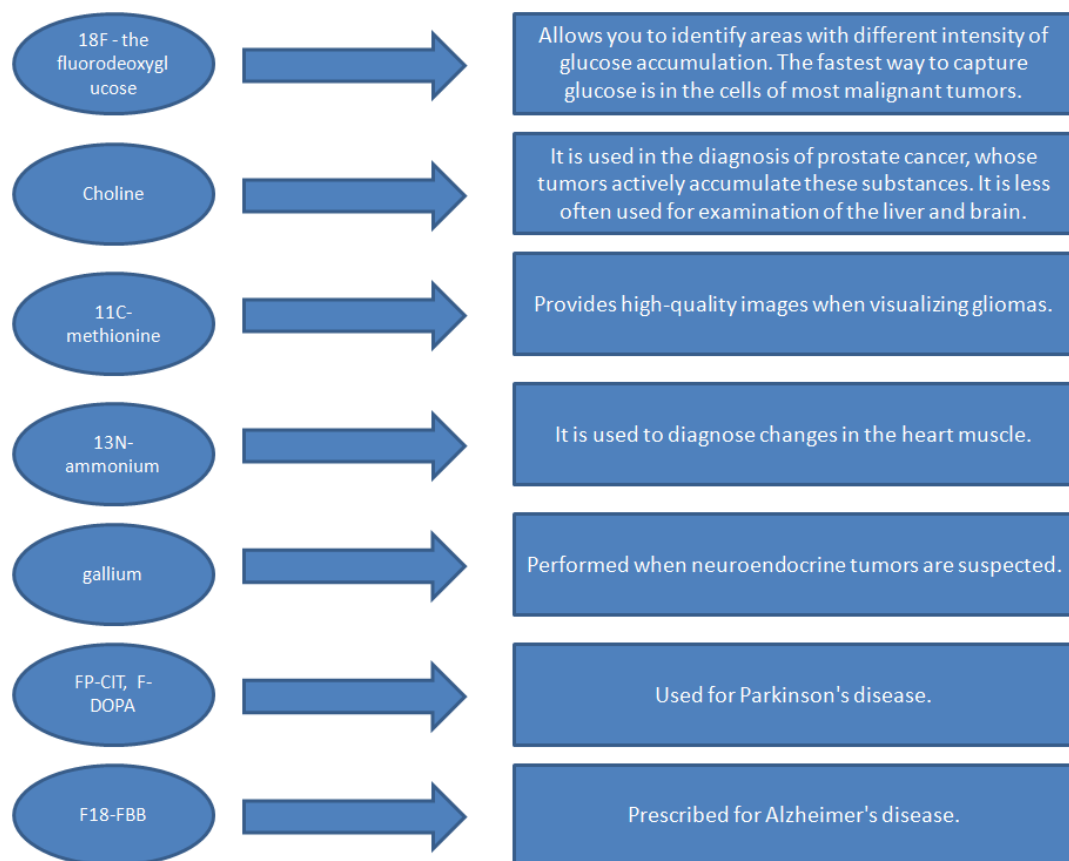


Figure 1 - types of radiopharmaceuticals, their effects and applications.

Positron emission tomography, the main field of application of which is the diagnosis of malignant formations, is rightly called the most advanced and promising method of research in Oncology, since it has a number of advantages over other methods:

- 1) the ability to detect disorders of the organ or tissue in its earliest stage before the appearance of structural changes;
- 2) determination of the presence and localization of metastases;
- 3) if necessary, it is also possible to differentiate the recurrence or progression of the tumor with necrosis that developed due to radiation;
- 4) evaluation of the result of chemotherapy at the beginning of the course of treatment.

Neurology is another area of use for positron-emission tomography.

Based on the results of the examination, neurologists can assess the condition of the arteries that feed the brain and their role in the violation of cerebral circulation, determine the cause of dementia, diagnose Alzheimer's disease, as well as degenerative diseases of the Central nervous system [3].

Less often, positron emission tomography is used in cardiology. In such studies, a temporary adaptive decrease in the volume of work of the heart muscle is diagnosed, the zones of myocardial ischemia are accurately determined, and areas of post-infarction cardiosclerosis are identified.

According to the head of the Department of radioisotope diagnostics of the national medical research center named after AK. Meshalkin, candidate of medical Sciences

StanislavMikhailovichMinin: "Nuclear medicine is one of the fastest growing areas. In 2018, the market for consumption of radionuclide services approached 25 billion dollars.

Experts expect that by 2030, this consumption will increase by 3-5 times. The main users of such services today are the United States, Japan, and European countries, which account for 80-90 %.

Russia is significantly inferior to them, although there are highly qualified personnel, research institutes, and a well-developed infrastructure of nuclear technologies."

According to analysts at the national research nuclear University MEPHI, the global market for nuclear medicine will reach \$24 billion in 2020 and \$43 billion in 2030. The Russian market will grow to \$1.2 billion. at the end of 2020 and will reach \$3.5-4 billion in 2030. Both the government and individual companies are interested in the development of nuclear medicine [5]. Despite the fact that Russia is one of the five largest producers of raw medical isotopes in the world, as well as grandiose plans for the development of this industry, there are a number of significant problems, including those related to hardware capacity.

According to the standards of the world Health Organization, 1 million people should have one positron emission tomograph, that is, 140 devices per country [1]. In 2013, there were 23 devices in the country, in 2016-only 4 more.

To date, there are about 29 active medical centers in Russia, of which 8 are located in Moscow, and 6-in St. Petersburg.

It is also worth noting that the total operational indicators of the industry do not even reach the targets of the Ministry of health: in 2016, according to the program "health Development", 316.5 thousand radionuclide studies were planned in the country, but only 266.9 thousand were completed.

64 thousand patients were going to be treated, but it turned out to be half as many – 27.7 thousand. At the same time, by the end of 2020, these indicators, according to the Agency's plans, should reach 320.5 thousand studies and 68 thousand cases of treatment, respectively.

As is known, positron emission tomography is a rather expensive process, largely due to the use of import equipment, a service that annually accounts for about 15 % of the main cost of equipment, as well as expensive consumables [2]. Thus, the first priority is to solve the problem of import substitution of nuclear medicine equipment through our own developments, which will make research more accessible.

To date, thanks to the implementation of the program of the Ministry of industry and trade until 2022, funding for new developments, including some medical equipment, has begun. Currently, a number of organizations are conducting research on generators, radiopharmaceuticals, and tomographs. Do not forget about the need to train appropriate personnel: radiochemists, medical physicists, quality control specialists, radiologists and medical equipment engineers.

Bibliographic list:

1. Golikova, T. A. // Draft report of the Minister of health and social development of the Russian Federation on the development of nuclear medicine at the meeting Of the Commission on modernization and technological development under the President of the Russian Federation – 2016.

2. Kostylev, V. A., Ryzhikov, O. A., Sergienko, V. B. // Status and prospects of development of methods of positron emission tomography in Russia - the Association of medical physicists of Russia, Moscow, 2 Russian cardiology research and production complex MH RF, Moscow, 2015. – p. 5-16.
3. Mokin, E. D. // Stages of development, areas of modern application, safety aspects of positron emission tomography // Youth scientific forum: Natural and medical science: elec. collection of articles on the Mat. XVIII inter-dunar.stud. nauch-prakt. konf. № 11(17) - 2014. – p. 42-52.
4. Narkevich, B. Ya., Kostylev, V. A. // Medical and physical bases of radionuclide therapy. etc. Textbook. - M., 2006. – p. 59.
5. The VII international Forum "Innovations in medicine: modern stages of formation and development" is a satellite event of the TechnoProm-2019 technological development Forum. "On the implementation of the Federal project" fight against cancer "of the national project" health care " in the constituent entities of the Russian Federation – members of the AMIS».

1B1b

Effect of plasmonic nanoparticles with various surface charge on the nonlinear absorption of methylene blue solutions

Rusinov Alexander, Kucherenko Michael

Orenburg University,
Center of Laser and Information Biophysics, Orenburg, Russia
E-mail:sano232@mail.ru

Abstract: The nonlinear light absorption of aqueous and alcohol solutions of methylene blue has been studied by the method of Z-scanning under continuous pumping. It is shown that the mechanisms of optical nonlinearity of these solutions vary depending on the dye concentration and type of solvent. The dependence of the amplitude of nonlinear absorption of dye molecules on the concentration and sign of the surface charge of gold and silver nanoparticles in solution is revealed.

Keywords: nonlinear light absorption, Z-scanning method, plasmon nanoparticles

Introduction

The nonlinear properties of optical materials associated with incoherent absorption saturation, multiphoton processes, thermal or Kerr nonlinearity are of undoubted interest for modern physics and its applications.

Among the wide range of experimental methods for studying the nonlinear optical properties of various systems [1], the Z-scan method has recently been greatly developed. The method consists in measuring the intensity of the focused light flux transmitted through the sample at different positions of the sample relative to the focus of the beam. This makes it possible in the open aperture mode to measure the dependence of the nonlinear absorption coefficient of the sample on the power density of the incident radiation, and in the limited(closed) aperture mode to determine the nonlinear light refraction in the material [2].

Materials and methods

In our case, the Z-scan setup is based on a continuous semiconductor laser with a power of 400 mW and a wavelength of 660 nm. The optical setup is shown in Fig. 1, the radius w_0 of the pump beam waist in the focal plane of the lens was 20 μm , the Rayleigh beam waist length $z_R = 2$ mm. Nonlinear absorption of solutions was measured in the open aperture mode. For optical sensitization of the studied aqueous and aqueous-alcoholic solutions in this work, we used an organic dye – methylene blue (MB) in concentrations from 10^{-5} to 10^{-3} M. In aqueous and aqueous-alcoholic solutions, this dye is positively charged.

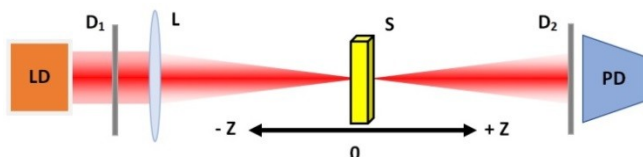


Fig. 1. The scheme of the Z-scan. z is the position of the sample relative to the focus of the lens. LD—radiation source, D_1 , D_2 —aperture; L—lens, PD—photodetector, S—sample.

The synthesis of negatively charged gold and silver NPs was carried out according to the Turkevich–Frens method [3] (Fig. 2a). In this method, sodium citrate was the metal reducing agent and NP surface stabilizer, and hydrogen tetrachloraurate was used as the sources of gold atoms (AgNO_3 was used as the source of silver synthesis in the parallel method). The concentration of NPs synthesized in this way was 120 $\mu\text{g/mL}$ (or 0.6 mM). According to [4], the NPs are negatively charged; the ζ potential measured by dynamic light scattering is -18 mV.

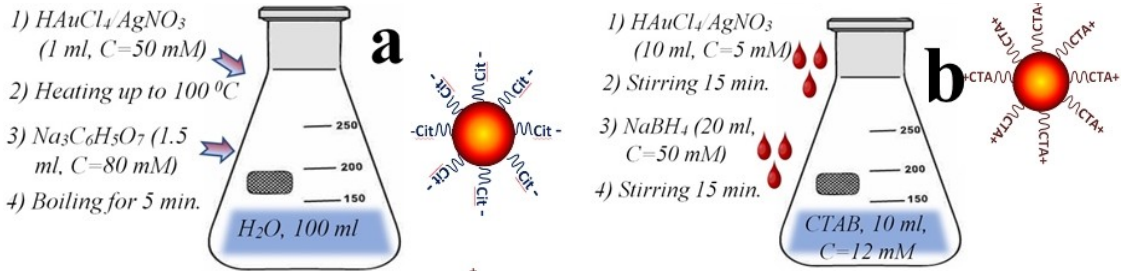


Fig. 2. Scheme for the synthesis of gold and silver NPs by citrate (a) and borohydride (b) reduction.

The synthesis of gold NPs stabilized by CTMA was carried out according to the borohydride method, similar to that described in [5] (Fig. 2b). In this method, sodium borohydride was used as a reducing agent, CTMA was used as a stabilizer, and hydrogen tetrachloroaurate was also used as a source of gold atoms (AgNO_3 was used as a source of silver synthesis in a parallel method). The concentration of gold NPs synthesized in this way is $140 \mu\text{g/mL}$ (0.7 mM for gold). According to [4], the NP data are positively charged; the ζ -potential measured by dynamic light scattering is $+40 \text{ mV}$. Note that the plasmon bands of the gold and silver NPs slightly overlap with the spectral range of the pump laser of the Z-scan setup (660 nm), i.e., the effect of NPs on the nonlinear properties of samples is indirect due to their interaction with dye molecules.

Nonlinear absorption of diluted dye solutions

It follows from Figs. 3a, 3b that in a water-ethanol solution, at a constant dye concentration, an increase in the proportion of alcohol in the range from 0 to 25% leads to an increase in the saturation of the absorption of the samples (an increase in the power of the transmitted beam in the waist by a factor of 1.1). A further increase in the proportion of alcohol in the solution (50% or more) changes the appearance of the Z-scan signals, a significant attenuation of the signal is observed in the constriction, i.e. nonlinear absorption enhancement is induced in the solution (the amplitude of this effect exceeds 50%).

Assuming that the velocity of the sample along the beam axis (the rate of change of intensity) is small compared to the characteristic times of transient processes in the medium, the mechanisms of nonlinear absorption of diluted aqueous-alcoholic solutions of MB can be considered based on the analysis of populations of various energy states of absorbing centers under constant pumping [6].

Then, the absorption coefficient, taking into account the transitions to highly excited levels S_2 and T_2 , is determined as

$$\alpha(I) = (\sigma_{01}n_{S_0}(I) - \sigma_{10}n_{S_1}(I)) + \sigma_{12}n_{S_1}(I) + \sigma_{12}^*n_{T_1}(I)$$

Here, the first two terms describe incoherent absorption saturation in the transition between the S_0 and S_1 states

$$\alpha_{\text{Sat}}(I) = \sigma_{01}n_{S_0}(I) - \sigma_{10}n_{S_1}(I) = \frac{\alpha_0}{1 + I/I_S}$$

where α_0 is the linear absorption coefficient, I_S is the intensity of the saturation of the solution. It follows from Figs. 4b and 4a, that for MB aqueous solutions this particular nonlinearity mechanism is characteristic, which indicates a small accumulation of dye molecules in the triplet state.

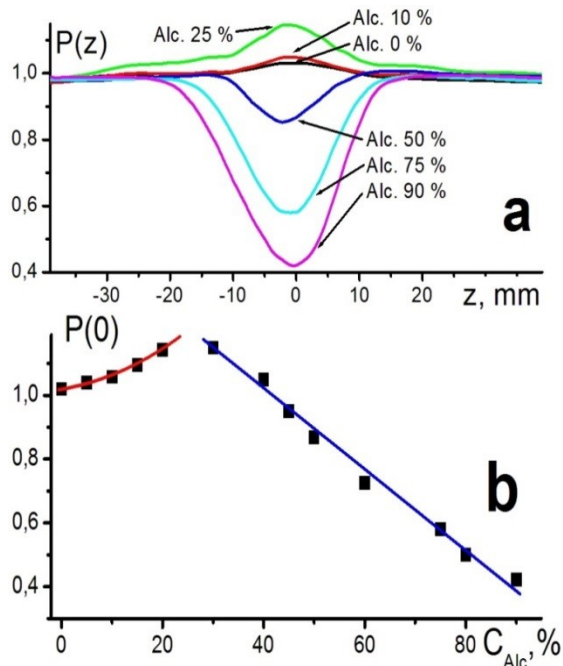


Fig. 3. Z-scan signals with an open aperture of aqueous alcoholic solutions of MB with a concentration of 5×10^{-5} M at various ethanol-water ratios.

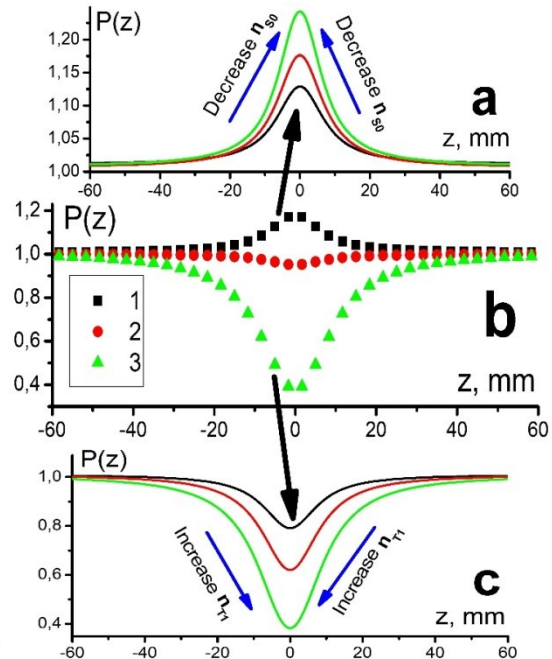


Fig. 4. Nonlinear absorption of a solution of dye molecules (b) at levels 1— S_0 , 2— S_1 , 3— T_1 ; (a) optical enlightenment of the S_0 state; (c) induced absorption of the T_1 state.

In water-ethanol solutions, with an increase in the alcohol fraction, a nonlinear increase in absorption is observed, which is associated with an increase in the lifetime of the excited states of MB molecules in alcohol solutions and, consequently, with an increase in their population in solutions (Figs. 4b and 4c). Since the lifetime of the triplet excited state T_1 is much longer than the singlet state S_1 , the fourth term will give the main part of the induced additional absorption

$$\alpha_{Add}(I) = \sigma_{12}^* n_{T_1}(I) = \frac{\beta I}{1 + I/I_S}$$

The effect of plasmon NPs on nonlinear dye absorption

To determine the effect of gold and silver NPs on the nonlinear absorption of MB, we prepared series of solutions in water and ethanol with a constant concentration of dye molecules ($C = 5 \times 10^{-5}$ M) and various contents of plasmon NPs (0, 20, 40, 60, 80%), where 100% NP content in solutions corresponds to a concentration of 0.7 mM.

It follows from Fig. 5a, that the addition of NPs stabilized by a citrate ion and having a negative surface charge in aqueous MB solutions leads to a decrease in the nonlinear saturation of the dye absorption. Moreover, while for gold NPs, the maximum signal decrease is about 20%, then for silver NPs it is already 60%. Positively charged NPs prepared by borohydride reduction almost double the amplitude of nonlinear optical enlightenment of the solution.

In alcoholic solutions (Fig. 5b), the introduction of negatively charged NPs also leads to a decrease in the induced nonlinear absorption of the dye by almost 3 times, however, no significant differences between silver and gold NPs are observed. For positively charged NPs (borohydride technique), this dependence is practically absent.

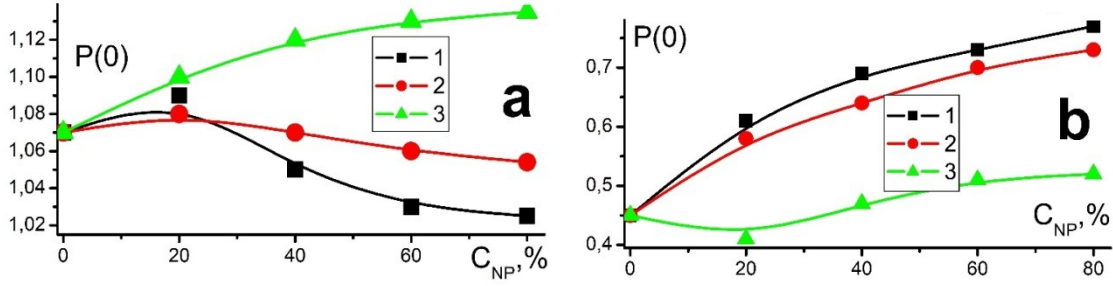


Fig. 5. Z-scan signals of aqueous ethanol solutions of MB with a concentration of 5×10^{-5} M at various concentrations of NPs. Gold (1) and silver (2) NPs were prepared by the citrate method; gold NPs (3) were prepared by the borohydride method.

Within the framework of the quasistatic approximation [7], it can be shown that near the plasmon NP, the probability of transitions between the energy states of the dye molecule is determined by the total dipole moment of the “NP-molecule” system.

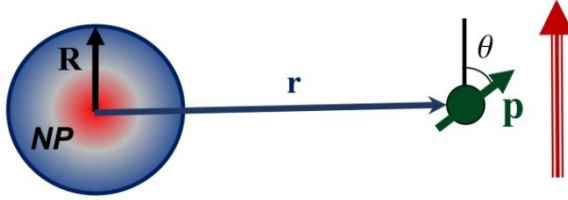


Fig. 6. The geometry of the “NP-molecule-field” system.

For the geometry of the “NP-molecule-field” system shown in Fig. 6, the probability of induced transitions can be written as

$$w_{ind}(\omega) = \left(\frac{\mathbf{p} \cdot \mathbf{E}_0}{\hbar} \right)^2 \left(1 + \frac{\text{Re} \alpha(\omega)}{r^3} (1 + 3 \cos 2\theta) + \frac{|\alpha(\omega)|^2}{4r^6} (1 + 3 \cos 2\theta)^2 \right)$$

Here, the first term in brackets is responsible for transitions in a solitary molecule, and the second and third terms describe the change in the probability of transitions in the presence of NPs. In this case, the second term—the interference term is more “long-range” compared to the third and, in contrast to it, can lead to both amplification and decrease, depending on the sign of this term. Thus, the effect of NPs on induced processes in the dye molecule in the first approximation, one can reduce the change in the absorption cross section for the transition between i and j states:

$$\sigma_{ij}^{eff} = \sigma_{ij} + \sigma_{ij}^{NP}$$

In addition to the processes considered above, it is also necessary to take into account the nonradiative transfer of energy of electronic excitation of molecules to plasmon modes of NPs with their subsequent attenuation. As shown in [8], the rate of such transitions is defined as

$$U_{rl}(\omega) = \frac{1}{2\hbar} \frac{p^2}{\epsilon_m^2 r^6} (1 + 3 \cos^2 \theta) \text{Im} \alpha(\omega)$$

and manifests itself mainly at sufficiently small distances for close pairs of “NP-molecule.” Qualitatively, this process leads to accelerated deactivation of excited states and can be taken into account through a decrease in the lifetime of i level in the dye molecule: This approach allows us to explain the different effects of plasmon NPs with the opposite sign of the surface charge on the optical nonlinearity of MB.

$$\tau_i^{eff-1} = \tau_i^{-1} + \tau_i^{NP-1}$$

Thus, in aqueous solutions, optical absorption saturation is observed, associated with a decrease in the population of the basic state S_0 . Negatively charged NPs (interact with positively charged MB molecules, which leads to their convergence and the formation of “close” “dye-

NP” complexes. At these distances, nonradiative quenching of excited NP dye molecules is more pronounced, the basic level population increases, and the optical enlightenment of solutions. Relatively positively charged NPs, MB molecules are located farther, therefore, nonradiative deactivation efficiency decreases. However, due to the lower locality, amplification of the induced absorption in the band of the $S_0 \rightarrow S_1$ transition appears at these distances, which leads to an increase in the saturation of the solution absorption and Z-scan signal in the beam constriction (Fig. 5a) This is confirmed by photometric measurements, which show that, at a constant dye concentration, the introduction of plasmon NPs into the solution, regardless of their charge sign, increases the optical density of the solutions.

In ethanol solutions of the dye, a nonlinear absorption enhancement is observed associated with the accumulation of molecules in the triplet excited state. Therefore, negatively charged NPs attracting the dye to the distance of effective nonradiative quenching exert the greatest influence on the nonlinear absorption of MB, which leads to accelerated deactivation and a decrease in the populations of the excited states of the dye. For positively charged NPs, this effect is much less pronounced.

Conclusions

It was shown that the optical nonlinearity of diluted dye solutions exhibits a strong dependence on the type of solvent. In aqueous solution, there is incoherent absorption saturation in the transition between the S_0 and S_1 states, and in alcoholic nonlinear absorption enhancement in the transition band $T_1 \rightarrow T_2$, associated with an increase in the lifetime of triplet excited states of molecules.

The dependence of the amplitude of the nonlinear response of dye solutions on the concentration of plasmon NPs and the sign of their surface charge is revealed. In aqueous MG solutions, the addition of NPs having a negative surface charge leads to a decrease in the nonlinear saturation of the dye absorption.

Positively charged NPs increase the amplitude of nonlinear optical enlightenment of the solution by almost a factor of two. In alcoholic solutions, the introduction of negatively charged NPs leads to a decrease in the nonlinear absorption of the dye by about 3 times.

The research was carried out with the financial support of the Ministry of Science and Higher Education of the Russian Federation within the framework of scientific project No. FSGU-2020-0003.

References

- [1] Kang I., Krauss T., Wise F. // Opt. Lett. 1997. V.22. P.1077.
- [2] Stryland E.W., Sheik-Bahae M. Z // Charact. Tech. Tabul. Org. Nonlinear Mater.1998. № 3. P. 655.
- [3] Frens G. // Nat. Phys. Sci. 1973. V. 241. P.20.
- [4] Li Z.P., Duan X.R., Liu C.H., Du B.N. // Anal. Biochem. 2006. V.351. P.18.
- [5] Andreu-Navarro A., Fernandez-Romero J.M., Gomez-Hens A. // Anal. Chim.Acta. 2012. V.713. P.1.
- [6] Kucherenko M.G. Rusinov A.P. // Quantum Electron. V.34. №8. 2004. P.779.
- [7] V. V. Klimov, Nanoplasmonics. Fizmatlit: Moscow, 2009.480 p.
- [8] M. G. Kucherenko, Vestn. OGU V.137 №1, P.141.

1B3b

Delayed fluorescence of molecules on the surface of ferroplasmonic nanoparticles

Alimbekov Ildar, Kucherenko Michael, Neyasov Petr

Orenburg University, Center of Laser and Information Biophysics, Orenburg, Russia

E-mail: clibph@yandex.ru

Based on an original mathematical model, the rate of annihilation delayed fluorescence (DF) of organic molecules on the surface of a layered spherical nanoparticle is calculated under the assumption that one of the molecules remains stationary, while the other diffusively moves along the outer surface of the particle. A composite particle consists of a ferromagnetic cobalt core and a plasmon shell - gold or silver. The calculations took into account the inhomogeneous and anisotropic nature of the magnetic field created by the ferromagnetic core of the composite. The predominant influence of the dimensional parameters of the system on the rate of delayed fluorescence by means of a plasmon increase in the probability of transitions in the molecule (more than 30%) is shown. The manifestation of the magnetic factor in the rate of the triplet-triplet annihilation reaction was not as noticeable (about 9%). The DF spectra demonstrate a clear dependence of the signal amplitude on the ratio of the core radius and the shell thickness of the layered nanocomposite.

Key words: ferroplasmonic nanocluster, “core-shell” nanoparticle, delayed fluorescence.

The synthesized organometallic nanostructures, which combine the properties of individual constituent components, are very relevant for the creation of functional systems of magnetically controlled molecular photonics [1-3]. It is assumed that such systems will be able to perform, for example, magnetic modulation of the rate of nonradiative triplet-singlet energy transfer between molecules in a nanocomposite. This becomes possible due to a change in the conditions of the triplet-triplet annihilation (TTA) reaction of excitons or excited electronic states of molecules in an external magnetic field or the field of a ferromagnetic nanoparticle. Because of this, it seems important to create hybrid nanostructures from metallic nanoparticles (plasmonic and ferromagnetic) associated with organic molecules or quantum dots, as well as

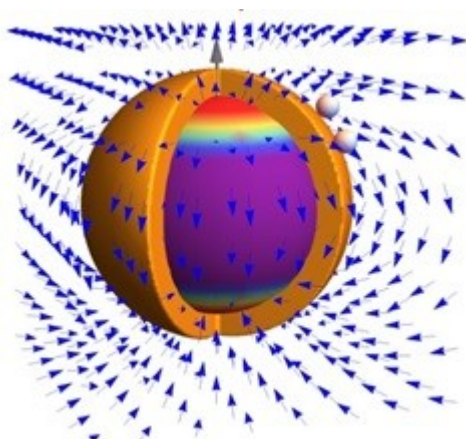


Fig. 1 – Layered spherical nanocomposite with a magnetic cobalt core and a plasmon shell made of gold or silver

macromolecular linkers (excitonogenic or passive with respect to electronic activation). One of the problems arising in this case is the optimization of the parameters of such nanostructures for their effective functioning. Along with its solution, it is necessary to study in detail the effect of plasmonic nanoparticles on the yield of delayed fluorescence accompanying the spin-selective magnetically dependent reaction TTA.

In this paper, we consider a system consisting of a spherical nanocomplex with a ferromagnetic cobalt core and a shell of a plasmon-active metal: gold or silver (Fig. 1). The magnetic moment of the nucleus is induced by an external source with a magnetic field induction B_0 .

It is assumed that dye molecules are planted on the surface of the nanoparticle, one of which is fixed at the place of the greatest amplitude value of the magnetic field induction - the magnetic “pole”, and the other can freely move diffusively over the surface. The cases of composites with varying core radii and plasmon shell thicknesses are considered.

Calculation of frequency dependent dielectric constants of core and shell materials $\varepsilon(\omega)$ was carried out on the basis of the Drude-Lorenz model [4]

$$\varepsilon(\omega) = \varepsilon_{\infty} - \frac{\omega_{pl}^2}{\omega + i\omega\gamma} \quad (1)$$

Dipole polarizability $\alpha_e(\omega)$ of a nanoparticle were calculated by the formula [4]

$$\alpha(\omega) = R_2^3 \frac{(\varepsilon_2(\omega) - 1)(\varepsilon_1(\omega) + 2\varepsilon_2(\omega)) + \xi^3(1 + 2\varepsilon_2(\omega))(\varepsilon_1(\omega) - \varepsilon_2(\omega))}{(\varepsilon_2(\omega) + 2)(\varepsilon_1(\omega) + 2\varepsilon_2(\omega)) + 2\xi^3(\varepsilon_2(\omega) - 1)(\varepsilon_1(\omega) - \varepsilon_2(\omega))} \quad (2)$$

where $\varepsilon_1(\omega)$, $\varepsilon_2(\omega)$ - frequency-dependent dielectric constants of the core and shell, respectively; R_1 и R_2 - core radius and outer radius of the nanocomposite, the ratio of these radii $\xi = R_1 / R_2$.

Spectral density of the number of photons emitted by a molecule at a frequency ω defined by the expression [5]

$$N(\omega) = \frac{1}{2\pi} \frac{w_{sp}(\omega)\Gamma^2(\omega)}{(\omega - \omega_{if})^2 + \Gamma^2(\omega)} \eta(\omega) \quad (3)$$

where $\eta(\omega) = w_{sp}(\omega) / \Gamma(\omega)$ - luminescence quantum yield; $\Gamma(\omega)$ - half-width of the spectral

band of molecular luminescence: $\Gamma(\omega) = w_{sp}(\omega) + U(\omega) + K$, $K = \text{const}$. The rate of quenching of the excited singlet state of a dye molecule by a composite nanoparticle is determined by the expression

$$U(\omega) = \frac{\mathbf{P}_M^2}{2\hbar\varepsilon_m r^6} (1 + 3\cos^2\theta) \text{Im}(\alpha(\omega)) \quad (4)$$

Here \mathbf{P}_M - vector of the electron dipole moment of the transition in the molecule; ε_m - dielectric constant of the medium. Expression for speed $w_{sp}(\omega|r)$ spontaneous emission of an annihilation partner molecule located near a nanoparticle at a distance r from its center can be written in the following form [5,6]:

$$w_{sp}(\omega|\mathbf{r}) = \frac{4}{3} \frac{\omega^3}{\hbar c^3} \left| \left[\mathbf{I} + \alpha_e(\omega) \mathbf{G}(\mathbf{r}) \right] \mathbf{P}_M \right|^2 \quad (5)$$

where $\mathbf{G}(\mathbf{r}) = r^{-3} \left[3(\mathbf{r} \otimes \mathbf{r}) / r^2 - \mathbf{I} \right]$ - tensor Green's function of a quasistatic field of a point dipole source; \mathbf{I} - unit tensor.

The observed rate of delayed fluorescence can be written as

$$w_{DF}(\omega) = K_{ann}(H) n_T^2 N(\omega) / \Gamma(\omega) = K_{ann}(H) n_T^2 \frac{1}{2\pi} \frac{w_{sp}(\omega) \Gamma(\omega)}{(\omega - \omega_{if})^2 + \Gamma^2(\omega)} \eta(\omega) \quad (6)$$

Thus, as seen from (6), ferromagnetic part of the nanocomposite affects the rate constant TTA by magnetic field [7], created by the core of a nanoparticle, which is calculated by the formula (7), and its plasmonic part – on the rate of radiative decay of a singlet-excited molecule near a nanoparticle. Second order rate constant $K_{ann}(H)$ – triplet-triplet annihilation – calculated according to a general model that takes into account the contribution of three competing mechanisms: spin-spin interaction, Δg and field gradient ∇H [8].

$$\mathbf{H} = \mathbf{H}_0 + \frac{3\mathbf{R}(\mathbf{m} \cdot \mathbf{R})}{R^5} - \frac{\mathbf{m}}{R^3}$$

$$\mathbf{m} = \frac{4\pi R_2^3}{2\mu_2 + \mu_1} \mathbf{M}_0 + \frac{\mu_1 - \mu_2}{2\mu_2 + \mu_1} R_2^3 \mathbf{H}_0 \quad (7)$$

where \mathbf{m} - magnetic moment of core, \mathbf{M}_0 - ferromagnetic core magnetization vector, \mathbf{H}_0 - external magnetic field strength, \mathbf{R} - is a vector drawn from the center of the nanoparticle to the observation point, μ_1, μ_2 - magnetic permeability of a ferromagnetic core and medium. The first term on the right-hand side of the expression for the magnetic moment \mathbf{m} in (7) takes into account the contribution of residual magnetization to the formed total magnetic moment \mathbf{m} ferromagnetic core.

Figure 2 shows the delayed fluorescence spectra of organic dye molecules located on the surface of a composite system of the type core-shell, centered at the resonant frequency of the molecular transition $\omega_{if} = 3.6 \cdot 10^{15}$ when changing the radius of the cobalt core and, accordingly, the thickness of the gold shell of the composite. Due to the presence of dissimilar materials, both the magnetic core and the plasmon shell contribute to the overall delayed fluorescence rate. The induction of the magnetic field of the cobalt core due to the inhomogeneity of the field affects the rate of the triplet-triplet annihilation reaction. According to the estimates made in the course of calculations, the greatest contribution is made by the inhomogeneity of the magnetic field, which is taken into account by means of the gradient mechanism of the field strength H . However, the contribution of the rate constant T-T-annihilation into delayed fluorescence rate as shown in the figure 3, is about 9 %. The main contribution to the change in intensity DF when composite nanoparticles are introduced, the plasmon shell of the composite exerts an increase in the probability of radiative transitions in the "molecule-particle" system.

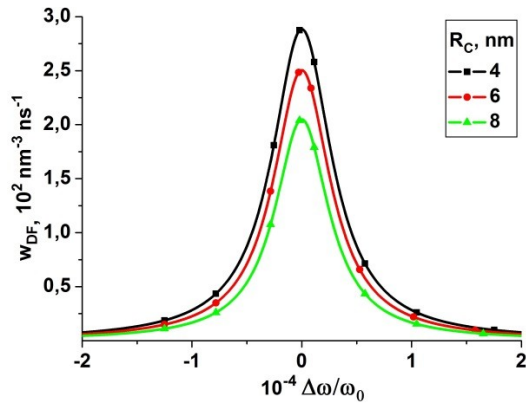


Fig. 2 – Delayed fluorescence spectra of dye molecules on the surface of a ferroplasmonic nanocomposite with a gold shell for different core radii R_C .

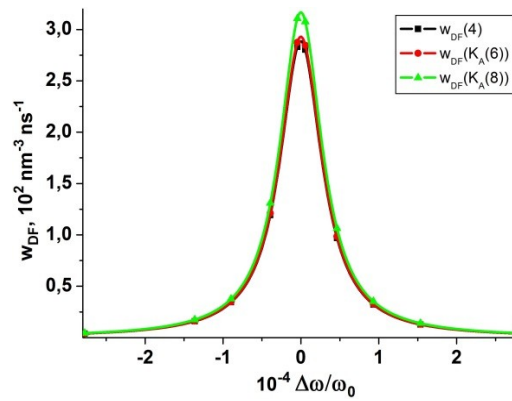


Fig. 3 – Dependence of the amplitude of the delayed fluorescence rate on the constant $K_A(R_C)$ rate of a TTA in a nanocomposite with a gold shell.

$$\omega_{plCo} = 14.79 \cdot 10^{15} c^{-1} \quad \omega_{plAg} = 13.82 \cdot 10^{15} c^{-1} \quad \omega_{plAu} = 13.67 \cdot 10^{15} c^{-1} \quad \omega_{if} = 3.6 \cdot 10^{15} c^{-1}$$

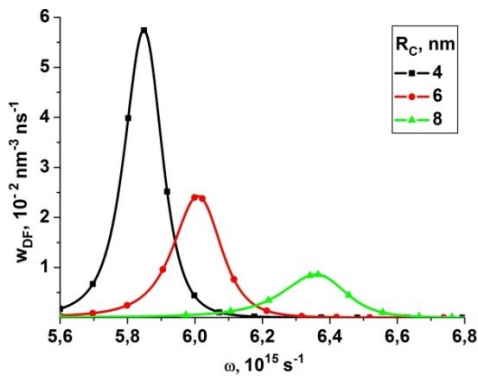


Fig. 4 - Spectra W_{DF} delayed fluorescence of dye molecules on the surfaces of ferroplasmonic nanocomposites with a silver shell for different radii of the cobalt core.

Figure 4 shows the velocity spectra $W_{DF}(\omega)$ delayed fluorescence of organic dye molecules on the surfaces of ferroplasmonic nanocomposites with a silver shell for different values of the radius of the cobalt core in the frequency range from 5.6 to $6.8 \cdot 10^{15} s^{-1}$. In this frequency range, a characteristic plasmon resonance is observed for a silver shell. With decreasing shell thickness, the signal amplitude decreases DF with a noticeable broadening of the Lorentzian spectral profile and a shift of its maximum toward the high-frequency region. From this we can conclude that the signal DF at a high frequency, arising at the smallest thickness of the silver shell, reflects the plasmon-resonance properties of the cobalt core,

which are not as pronounced as in a shell made of a noble metal. Under such conditions, the probability of emission of the complex "phosphor molecule-nanocomposite" decreases, and the width of the spectral line of the DF increases.

Thus, ferroplasmonic nanocomposites of complex structure can be used to control magnetically sensitive light signals in some organic nanophotonics devices.

This study was supported by the Ministry of Science and Higher Education of the Russian Federation, project no. FSGU-2020-0003.

References

1. *Ward Brullot et al. Magnetic-plasmonic nanoparticles for the life sciences: calculated optical properties of hybrid structures // Nanomedicine: Nanotechnology, Biology and Medicine. 2012. V. 8 Issue 5. P. 559-568*

2. **Eugenio Redolfi Riva et al. Plasmonic/magnetic nanocomposites: Gold nanorods-functionalized silica coated magnetic nanoparticles // Journal of Colloid and Interface Science 2017. V. 502. P. 201-209**
3. **Marcin Runowski et al. Luminescent-plasmonic, lanthanide-doped core/shell nanomaterials modified with Au nanorods – Up-conversion luminescence tuning and morphology transformation after NIR laser irradiation // Journal of Alloys and Compounds 2018. V. 762.P. 621-630**
4. **Klimov, V.V. Nanoplasmonics / V.V. Klimov. - FIZMATLIT, 2009. –480 c.**
5. **Kucherenko M.G., Nalbandyan V.M. Absorption and spontaneous emission of light by molecules near metal nanoparticles in external magnetic field // Physics Procedia. 2015. V. 73. P. 136–142.**
6. **Plasmon-activated processes in a hybrid molecular cluster with a spherical nanoparticle / V. M. Nalbandyan, E. V. Seliverstova, D. A. Temirbaeva, M. G. Kucherenko, N. Kh. Ibraev \ 11th Intern. Confer. «Chaos and structures in nonlinear systems» 2019, Kazakhstan, Karaganda. P. 128-133.**
7. **Meledin G.V., Cherkassky V.S. Electrodynamics in problems. Part 1 electrodynamics of particles and fields. Chapter 5 Magnetostatics.**
8. **Kucherenko M.G., Alimbekov I.R., Neyasov P.P. Peculiarities of annihilation delayed fluorescence of organic molecules near a spherical ferroplasmonic nanocomposite // All-Russian. Scientific Confer. Univer. Complex as a Region. Center of Educ., Science and Culture. Orenburg: OSU. 2020. P. 2222-2229.**

1B4b

Surface-enhanced infrared absorption spectroscopy of lanthanide complexes with N-donor or O-donor ligands on Au surface

Shogo Meiji,¹ Sakiko Hirata,² Seita Tamekuni,³ Satoru Muramatsu,^{1,2}
Takehiro Hirao,^{1,2} Takeharu Haino,^{1,2} Tosiki Sakata,²
Ken-ichi Saitow,^{1,2,4} Yoshiya Inokuchi^{1,2}

¹ Department of Chemistry, Graduate School of Advanced Science and Engineering, Hiroshima University

² Department of Chemistry, Graduate School of Science, Hiroshima University

³ Department of Chemistry, Faculty of Science, Hiroshima University

⁴ Department of Materials Science, Natural Science Center for Basic Research and Development, Hiroshima University

Separation of minor actinide (MA) and lanthanide (Ln) is a key process in the disposal of the radioactive high-level liquid waste from nuclear power plants. To achieve high selective separation is practically challenging because MA ions such as Am and Cm have similar chemical characteristics to Ln ions. One of the separation methods is solvent extraction with organic ligands; this has been extensively performed in the disposal processes. The selectivity of Eu(III)/Am(III) depends highly on donor atoms of ligands; O-donor ligands prefer to Eu(III) than Am(III), and S- and N-donor ligands show opposite trends.^[1] However, the origin of these preferences has not been understood so far from microscopic viewpoints. In this study, we observe IR absorption spectra of Ln complexes by surface-enhanced infrared absorption (SEIRA) spectroscopy to examine the interaction between Ln ions and organic ligands, and finally to understand the relation between the bonding nature and selectivity.

Firstly, we synthesize thiol derivatives of diglycolamide (DGA) and bis(4-mercaptobutyl)phosphinic acid (BMPA), which act as an O-donor ligand. In addition, we also synthesize thiol derivatives of *N,N,N',N'*-Tetrakis(2-pyridinylmethyl)-1,2-ethanediamine (TPEN), which act as a N-donor ligand (Fig. 1). The gold surface is formed by vacuum deposition on a Si prism for ATR-IR measurements. The thiol derivative of the ligand is dissolved in DMSO and dropped onto the gold surface to form an Au-S covalent bond, which is chemically adsorbed on the Au surface (Fig. 2). After removing the solution of the ligand, an aqueous solution of $\text{EuCl}_3 \cdot 6\text{H}_2\text{O}$ is placed on the surface to form the Eu^{3+} complex, and the IR spectra of the complex are obtained using an FT-IR spectrometer.

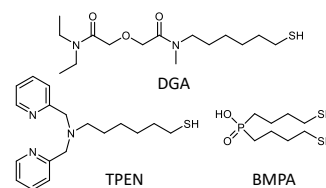


Fig. 1. Thiol derivatives of ligands.

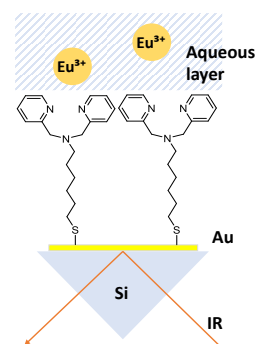


Fig. 2. A schematic drawing of ligands chemisorbed on a gold surface.

Figs. 3a–c display the IR difference spectra of the Eu^{3+} complexes with TPEN, DGA, and BMPA, respectively. The IR spectrum of the Eu^{3+} -TPEN complex shows a signal at $\sim 1600\text{ cm}^{-1}$ (Fig. 3a). This band can be assigned to deformation vibrations of the pyridine ring. The IR spectrum of the Eu^{3+} -DGA complex shows a signal at $\sim 1600\text{ cm}^{-1}$ (Fig. 3b). This band is attributed to the C=O stretching vibrations. For the Eu^{3+} -BMPA complex, the IR spectrum (Fig. 3c) show a strong signal at $\sim 1050\text{ cm}^{-1}$, which can be assigned to the stretching vibration of the $(\text{POO})^-$ group. These results indicate that the formation of the Eu^{3+} complexes can be detected by SEIRA spectroscopy with their vibrational signatures.

Here it should be noted that the concentration of the Eu^{3+} ion is different from each other for the IR spectra in Fig. 3. The IR spectra of the DGA and BMPA complexes are observed at the Eu^{3+} concentration lower than 1 mM (Figs. 3b

and c). In the case of the Eu^{3+} -TPEN complex (Fig. 3a), we have to use the Eu^{3+} solution at the concentration of 1 M, three orders of magnitude higher than that for the DGA and BMPA complexes, to obtain comparable signal intensity. One possibility of this result is that the IR transition probability of TPEN may be substantially smaller than that of DGA and BMPA. Table 1 shows the IR intensity of a representative vibration calculated by quantum chemistry calculations. The IR intensity of TPEN is certainly smaller than that of DGA and BMPA, but it is not so small to explain reasonably the large difference in the Eu^{3+} concentration for the IR measurement in Fig. 3. As mentioned above, the O-donor ligands show high affinity to Ln more than to MA. Hence, the difference in the Eu^{3+} concentration for the IR spectra can be attributed to the capability of the complex formation for Eu^{3+} ion; the coordination ability of the TPEN ligand with Eu^{3+} is smaller than that of the DGA and BMPA, resulting in smaller detection efficiency for TPEN by IR spectroscopy.

[1] Kaneko et al, *Inorg. Chem.*, **54**, 7130 (2015).

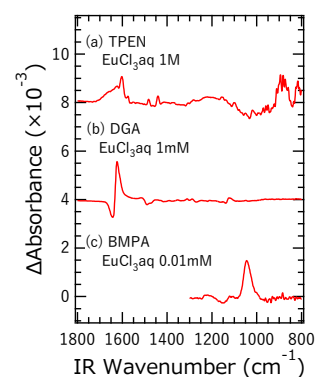


Fig. 3. The IR difference spectra of the (a) Eu^{3+} -TPEN (b) Eu^{3+} -DGA (c) Eu^{3+} -BMPA complexes.

Table 1. IR intensities of ligand peak

	TPEN	DGA	BMPA
IR Intensity (km/mol)	67	417	182
Frequency (cm^{-1})	1673	1776	1254

Gaussian09 M06-2X/6-311++G(d,p) Gaussian09 wb97xd / 6-31+G(d) Gaussian09 wb97xd / 6-31+G(d)

Masayuki Morie,¹ Ryo Sekiya¹, Takeharu Haino¹¹Department of Chemistry, Graduate School of Science, Hiroshima University

Biological functions such as information transfers, biological transformations, are driven by specific intermolecular interactions in water. Therefore, water-soluble artificial host-guest complexes have received great attentions so far to understand the specific intermolecular interactions in nature. Many synthetic receptors have been studied in organic solvents because of their low solubility in water. We reported the calix[4]arene-based triple stranded metallohelicates.^{[1],[2]} Replacing the alkyl chains with hydrophilic chains should improve the hydrophilicity of the metallohelicates, which results in the host-guest

complexes in water. Here, we report the water-soluble calix[4]arene-based hosts **1_{Ga}**, **1_{Fe}** (Figure 1).^[3] The preparation of **1_{Ga}** was determined by NMR spectroscopy. The aromatic proton signals of **G1** showed gradual upfield shifts upon the addition of **1_{Ga}** in water, indicative of the entrapment of the pyridinium moiety within **1_{Ga}**. The association constant of **G1** and **1_{Fe}** was evaluated by UV-vis titration experiments in water. Nonlinear regression analysis of the titration data led to an association constant of $4.83(8) \times 10^3 \text{ M}^{-1}$. On the other hand, the encapsulation of **G2**, **G3** within **1_{Fe}** generated 1:2 host-guest complexes with the association constants (**G2**: $K_{a1} = 3.7(1) \times 10^3 \text{ M}^{-1}$, $K_{a2} = 2.5(1) \times 10^3 \text{ M}^{-1}$; **G3**: $K_{a1} = 5.9(2) \times 10^3 \text{ M}^{-1}$, $K_{a2} = 3.3(1) \times 10^3 \text{ M}^{-1}$). An interaction parameter ($\alpha_{12} = 4K_{a2} / K_{a1}$) was given to be 2.5 and 2.2 for **G2** and **G3**, respectively. The positive cooperative effects were found in the 1:2 host-guest complexation in water.

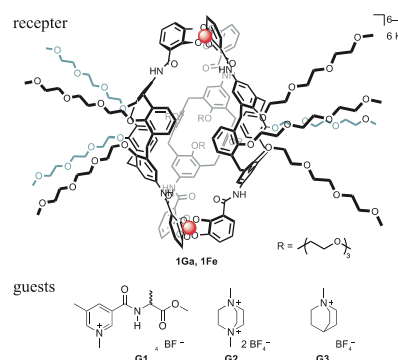


Figure 1. Molecular structures of water-soluble calix[4]arene-based triple stranded metallohelicates **1_{Ga}** and **1_{Fe}** and cationic and neutral guests **G1-G3**.

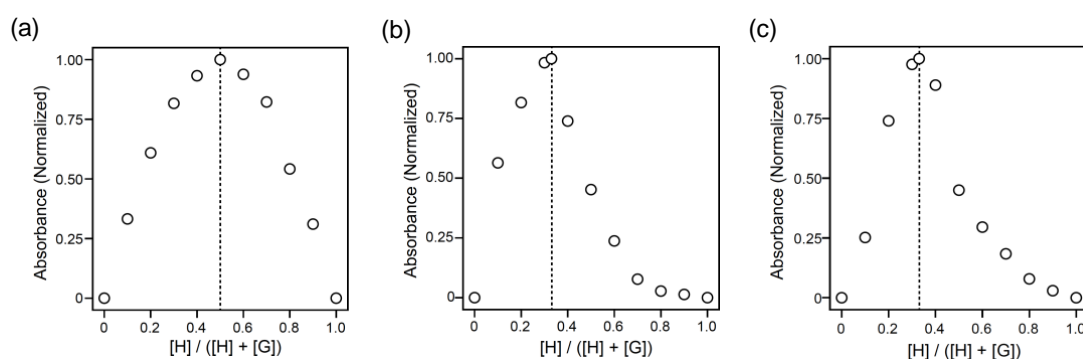


Figure 2. Job plots (H_2O , 298 K) of $K_6[1\text{Fe}]$ with (a) (R)-**G1**, (b) **G2**, and (c) **G3**. The total concentrations of $K_6[1\text{Fe}]$ and the guests are $1.0 \times 10^{-4} \text{ mol L}^{-1}$.

References

- [1] T. Haino, H. Shio, T. Takano, Y. Fukazawa. *Chem. Commun.*, **45**, 2481-2483 (2009).
- [2] Y. Yamasaki, H. Shio, T. Amimoto, R. Sekiya, T. Haino, *Chem. Eur. J.*, **24**, 8558-8568 (2018).
- [3] M. Masayuki, R. Sekiya, T. Haino, *Chem. Asian. J.*, DOI:10.1002/asia.202001154.

1C2b Inactivation of bacteria with shock acoustic waves generated by thermal sensitizers

Ishemgulov Azamat, Letuta Sergey, Pashkevich Sergey

Orenburg University, Orenburg, Russia

The mechanism of bacterial inactivation in solutions caused by the shock waves action is discussed. Shock waves are generated as a result of short-term heating after the relaxation of excited molecular thermosensitizer. Other possible mechanisms and their effect on bacterial survival are also assessed.

Photodynamic inactivation as a combined effect of light and sensitizers on living cells is a promising method of non-drug action on microorganisms; they cannot develop a stable immunity to this effect at all [1, 2]. There are several photoinduced mechanisms of bacterial inactivation, which can be divided into chemical, thermal and mechanical. Chemical mechanisms are mainly the action of active radicals and reactive oxygen species. The thermal mechanism is the conversion of light energy into heat with further destruction of the cell. The release of a large amount of heat in a small volume can cause local heating of the medium, as a result of which small bubbles form and collapse to form shock waves. The shock wave, moving in the environment, may mechanically damage the microorganisms.

If the thermal sensitizers (TC) are polyatomic molecules, then you can use their high-energy electronic states (HEES), that is, the energy states following S_1 . HEES S_n ($n > 1$) have a very short lifetime of about 1-10 ps and turn back to the S_1 states with heat release. When molecules are excited by light pulses with duration more than 1 ns, the absorption acts of light quanta by molecules and the conversion of light energy into heat can occur repeatedly. If a lot of TC molecules accumulate in small volume, a large of heat can be obtained in a very short time [3, 4].

Using of molecular TS is convenient in terms of the action of all three mechanisms. If the TS are located directly in the cells, their death can be caused due to hyperthermia. If the TS are outside of the cell, heat energy is transferred to the media, followed by the formation and collapse of small vapor bubbles, which leads to generation of acoustic shock waves that can also damage microorganisms. It should be noted that in the case of populating the lower triplet states of TS due to the HEES cascade relaxation, they are still capable of generating a reactive oxygen species. Shock acoustic waves can damage bacteria even at some distance from the area of light irradiation. In this work, we present the study results of damage to planktonic bacteria by acoustic shock waves.

Cell cultures of *Escherichia Coli* and *Bacillus Subtilis* were studied. Before irradiation, the cells were transferred to saline. Bacterial survival after exposure to visible light in the presence of a sensitizer was assessed by counting colony forming units (CFU).

The anionic xanthene dyes erythrosine and eosin, and the cationic dye rhodamine 6G were used as sensitizers. The dye concentration in solutions was 0.01–0.5 mM. These dyes have different photodynamic activity and variously interaction with the cell walls of gram-positive and gram-negative bacteria. Fig 1 shows the experimental setup that was used for photoinactivation of microorganisms and the study of shock waves in dye solutions. The solutions were placed in a rectangular quartz cuvette 1. Pulsed Nd:YAG laser 2 (second harmonic 532 nm, duration of each pulse 15 ns) was used as excitation source. For an efficient excitation of the medium in the cuvette near the “glass-solution” interface, an excitation zone 3 with a cross section of 3.2 x 0.5

mm² was created using a converging cylindrical lens 4. The maximum possible specific power at the beam waist of 50 MW/cm². The depth of penetration of the exciting beam into the solution decreases with increasing concentration of the dye and increases with increasing power density. The fluorescence of the excitation region was registered through the monochromator 5 by PMT 6 to obtain information on the relaxation of excited states of sensitizers. Shock waves were registered by change in the scattering of a probe beam of a low-power He-Ne laser 7 (parallel to the waist at a distance L). Actually, L is the distance from irradiation area to the point of observation. Synchronous work of the laser and the recording system, as well as the collection, accumulation and processing of signals were performed automatically.

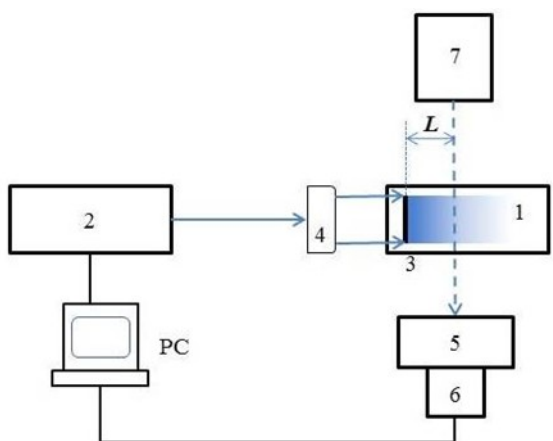


Fig 1 – Experimental setup

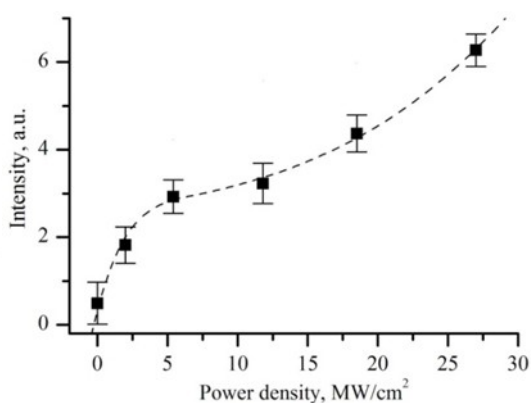


Fig 2 – Phosphorescence intensity of eosine saline solution related to excitation power density

Fig. 2 shows the dependence of the intensity of eosin phosphorescence in saline on the pump power density. At the beginning of the curve, the phosphorescence intensity increases rapidly, reaching saturation under power density about 5 MW/cm². This is due to saturation of the population of the S1 states, which provide the population of the T1 triplet states as a result of intersystem crossing. With a further increase in the power of the exciting laser, the phosphorescence intensity of eosin begins to increase smoothly. The dye molecules in the S1 states absorb the second quantum and moving to HEES. The quantum yield to triplet state of dye molecules from S_n more than from S1, therefore the intensity of phosphorescence increases. This experiment confirms the presence of the HEES population.

When probing beam of a He-Ne laser pass through a cuvette, several phenomena can be observed depending on the probing zone (Fig 3).

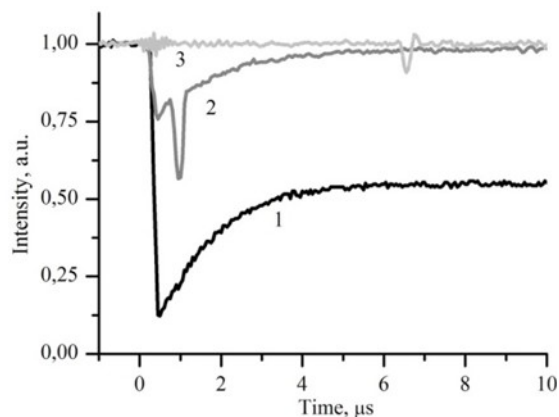


Fig 3 – Kinetics of probe He-Ne laser transition after excitation of TS: (1) $L = 0$; (2) $L = 3$ mm; (3) $L = 10$ mm

Directly in the irradiation zone (curve 1), there is an abrupt decrease in the intensity of the probing beam lasting up to several milliseconds, due to scattering on the arising vapor bubbles. In the time range 1-5 microseconds, induced triplet-triplet light absorption is also observed. Note that the existence of triplet states of the dye molecules in the presence of oxygen can lead to the formation of reactive oxygen species, which can cause additional bacterial damage. Sharp dips in curves 2 and 3, in our opinion, correspond to the moments when the probing beam intersects with the front of the acoustic shock wave formed in the irradiation zone. This is proved by the linear dependence of the time of occurrence of the dip on the distance L to the irradiation zone. The reverse slope of this straight line corresponds to the speed of sound in the medium (~ 1500 m/s).

Bubble scattering is observed only in the direct irradiation zone. Triplet-triplet absorption is observed at a distance of up to $L = 5$ mm, and shock waves are observed even at $L = 10$ mm. Thus, there are three areas where different effects on microorganisms are possible.

In the area of irradiation, bacteria can be damaged as a result of hyperthermia, action of shock waves or reactive oxygen species, as well as energy transfer from dye molecules to bacterial membranes or intracellular substrate. In the intermediate region, triplet sensitizer molecules are still present, but hyperthermia and energy transfer are unlikely. Here bacteria can be damaged by reactive oxygen species and shock waves. Finally, in a remote area, shock waves are the only cause to damage bacteria. Shock waves appear under local heating of the solvent. Local heating of the solvent arises as a result of nonradiative relaxation of HEES of sensitizer molecules.

The damage of bacteria was assessed by determining CFU for samples taken in the irradiation region directly, and at a distance of 5 and 10 mm from this region. Fig 4 shows the survival rate of *E. Coli* (EC) and *B. subtilis* (BS) in saline solutions with xanthene dyes (0.25 mM) before and after exposure to pulsed irradiation at different power densities and at different distances from the excitation region.

Anionic dyes do not interact with the negatively charged wall of *E. Coli* bacteria. Direct in the area of irradiation, damage to bacteria is observed even at low radiation power densities. This is a consequence of the combined action of various mechanisms of photo-induced damage. At distances of 5 and 10 mm from the excitation region, damage to *E. Coli* cells becomes evident only at an excitation power above 10 MW/cm^2 , when the efficiency of shock wave generation increases due to two-quantum absorption.

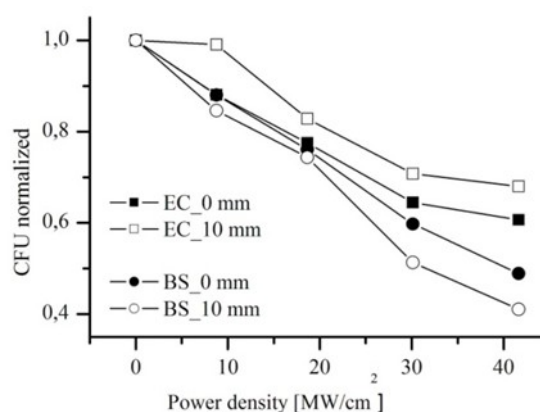


Fig 4 – CFU of bacteria related to excitation power density and the distance from irradiation

Gram-positive *B. Subtilis* bacteria have been more sensitive to shock waves action. Probably, their susceptibility to small doses of radiation is a result the dye binding with the bacterial wall. This facilitates the heat transfer to the microorganisms and increases the chance of their damage.

Shock waves generated due to fast local heating from TS damage bacteria effectively at distances many times exceeding the range of the conventional photodynamic effect. Damage to microorganisms becomes more effective with increasing concentration of the TS in solutions and depends on the power density of the exciting light. This can provide to develop a practical method for photodynamic inactivation of pathogenic microorganisms in the deep layers.

Study was supported by the Ministry of Education and Science of the Russian Federation, project number FSGU-2020-0003.

- 1. Wozniak A., Grinholc M. Combined Antimicrobial Activity of Photodynamic Inactivation and Antimicrobials–State of the Art. // *Front Microbiol.*, 2018, 9, 930.**
- 2. Kashef N. et al. Advances in antimicrobial photodynamic inactivation at the nanoscale. // *Nanophotonics*, 2017, 6, 853-879.**
- 3. Letuta S.N., et al. Photothermal Inactivation of Microorganisms under Relaxation of Highly Excited States of Sensitizers. // *Biophysics*, 2020, 65, 599-605.**
- 4. Kohmura Y. et al. Transient photothermal inactivation of *E. coli* stained with visible dyes using a nanosecond pulsed laser. // *Scientific Reports*, 2020, 10:17805.**

1C3b Laser-induced crystallization of amino acids at the chiral ionic liquid/water interface

Q.Dat Luong¹, Shoji Ishizaka¹

¹ Department of Chemistry, Graduate School of Science, Hiroshima University

[Introduction] Crystallization of various compounds in solution is a commonly employed method for separation and purification. Crystallization process can be carried out using conventional methods, such as heating-cooling solution, solvent evaporation, crystal seeding. However, crystallization of proteins with above methods was found to be difficult, due to the complex nature of proteins. In recent years, with the aid of laser, scientists have found that the crystallization of amino acids, such as Glycine and Phenylalanine, is possible without the need of supersaturated solution^[1,2]. Namely, when the air/solution is irradiated with NIR laser, the crystallization of amino acids can occur under the effect of photon pressure. Nonetheless, chiral selectivity at the chiral ionic liquid/water interface (chiral ionic liquid (CIL) is ionic liquid with chiral cation or anion)) has not been investigated using laser irradiation method. Therefore, our scheme is to achieve the chiral selectivity at the chiral ionic liquid/water interface by employing laser to induce the crystallization of amino acids. In this study, to test the chiral properties of ionic liquid, L-Phenylalanine derived ionic liquid was synthesized, and then utilized to the crystallization of L- and D-Leucine.

[Experiment] Ionic liquid in our research was [N,N,N-trimethyl-L-phenylalanine methyl ester]⁺[bis(trifluoromethane)sulfonimide]⁻ (herein, abbreviated as [(CH₃)₃N-PheOMe]⁺[NTf₂]⁻). To obtain this ionic liquid, we first started with the quaternization of L-Phenylalanine methyl ester hydro chloride using iodomethane and potassium carbonate, in acetonitrile at elevated temperature (90 °C). Then ionic liquid was synthesized using water as reaction medium. The result ionic liquid was extracted from water with dichloromethane, followed by solvent removal. The rate of crystallization of L- and D-Leu was compared in cases of with and without the presence of CIL. The L-Leu and D-Leu supersaturated solutions were prepared by stirring the corresponding 1.4 g of amino acids in 55 mL of water at 70 °C. In addition, a substantial amount of distilled water is also kept at 70 °C. In total, there were 5 samples; L-Leu with and without CIL (sample 1, 2), D-Leu with and without CIL (sample 3, 4), and water with CIL (sample 5). Temporally, each solution was diluted 50 times, and the corresponding UV-Vis absorption spectrum was recorded. The crystallization progress was then monitored using remaining concentration data obtained from UV absorption spectra.

[Results and discussion]

The synthesized ionic liquid was found to be immiscible with water, and thus formed an observable phase separation interface. The difference in kinetic of crystallization process for L- and D-Leu was yet to be recorded. However, it was shown by visual images and data that at equilibrium state, there was a remarkable difference between samples with and without ionic liquid. The time-wise concentrations of Leu solutions were recorded, featuring fluctuated data, in lieu of a gradually decreased one. The causes of the phenomenon were discussed.

[1] Cryst. Growth Des. 2010, 10, 11, 4686–4688

[2] Cryst. Growth Des. 2018, 18, 5417–5425

[3] CrystEngComm, 2016, 18, 8769

2A1b

Pulse spin manipulations with high spin ions for quantum computing

Arifullin Marsel, Berdinskiy Vitaly

Department of Physics, Orenburg University, Russia

Spin-orbital interactions in high spin ($S \geq 1$) paramagnetic ions embedded in crystal lattice induce zero fields splitting (ZFS) of ground state [1]. If there are no magnetic field, then spin states of ions (Ni²⁺, for example) are ground state $|0\rangle = 2^{-1/2}|\alpha_i\beta_j + \beta_i\alpha_j\rangle$ and excited states $|A\rangle = 2^{-1/2}|\alpha_i\alpha_j - \beta_i\beta_j\rangle$ and $|B\rangle = 2^{-1/2}|\alpha_i\alpha_j + \beta_i\beta_j\rangle$. All these states are well known naturally entangled Bell states [2].

RF or microwave pulses allow manipulation of populated states and coherent relationships between them, and hence magnetic properties. To describe pulse phase manipulations a new approach was suggested: the spin Hamiltonian of ions was presented as an Ising Hamiltonian; all spin rotation operator were presented as simple polynomials of one-spin Pauli operators. Thus, all three combinations of spin states $|0\rangle$, $|A\rangle$ and $|B\rangle$ can be used as qubits. However, pair of degenerate states $|A\rangle$ and $|B\rangle$ is more preferable due to absence of magnetic decoherence mechanisms [3]. Practical usage of paramagnetic crystals with embedded high spin ions needs neither strong magnetic fields, nor vacuum or laser equipment.

Resonant radiofrequency or microwave pulses having different polarizations and phases are able to produce spin manipulations similar to CNOT, Phase Shift, Quantum Fourier Transformations and others gates. For example, operation NOT described by the product of the operators $U_X(-\pi/2, \delta)U_X(\theta)$, leads to the transformation the matrix representation of which in the basis $|0\rangle, |B\rangle$ has the form

$$U_X(\text{NOT}) = \begin{pmatrix} 0 & 1 \\ 1 & 0 \end{pmatrix}.$$

The phase shift operator S can be realized using two pulses and described by the product of the operators $U_X(\pi/2, \delta)$ and $U_X(-\pi/2, 0)$. In the matrix form in the basis $|A\rangle$ and $|0\rangle$, it has the form

$$S = \begin{pmatrix} 1 & 0 \\ 0 & e^{i\delta} \end{pmatrix}.$$

The given logic operation is the key element in performing the quantum Fourier transform.

For spin paramagnetic sublevels, the first transition of alignment to polarization, controlled by radio frequency pulses, should be accompanied by the appearance of macroscopic magnetization even in zero magnetic fields [4-5].

The reported study was funded by RFBR according to the research project № 18-37-00374.

[1] **A. Abragam, B. Bleaney *Electron Paramagnetic Resonance of Transition Ions, Clarendon press, Oxford, (1970)***

[2] **M. Nielsen, I. Chuang. *Quantum Computation and Quantum Information Cambridge: Cambridge University Press (2010)*.**

- [3] **G. Pileio**, *Relaxation theory of nuclear singlet states in two spin-1/2 systems*, *Progress in Nuclear Magnetic Resonance Spectroscopy*, 56 (2010) 217-231
- [4]. **M.R. Arifullin, V.L. Berdinskiy**, *Physics of the Solid State* 62, p. 440–444 (2020).
- [5]. **M.R. Arifullin, V.L. Berdinskiy**, *High-Spin Paramagnetic Ions as Qubits and Qutrits for Quantum Computations*. *Russ. Phys. J.* (2020).

2A2b

Aggregation and disaggregation behavior of Nanographene

Ikuya Matsumoto, Ryo Sekiya, Takeharu Haino

Department of Chemistry, Graduate School of Advanced Science and Engineering, Hiroshima University

Nanographenes have received a great deal of attention because of showing photoluminescence (PL). We reported that the nanographenes, given by oxidative cleavage of graphite, have the vast π -conjugating plane. In this presentation, we will report the self-assembling behavior of nanographene NG-3 through the π - π -stacking interaction in organic solvents.

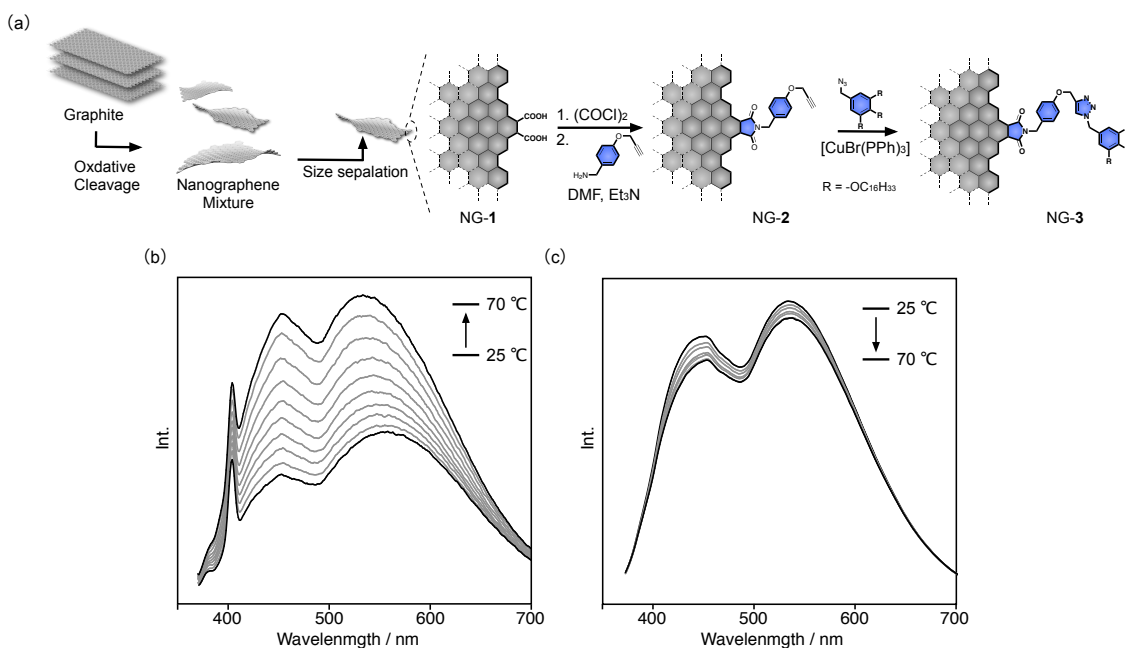


Figure 1. (a) The installation of long alkyl chain to nanographene of NG-1. PL spectra of NG-3 in (b) cyclohexane and (c) 1,2-dichloroethane.

The nanographenes with large size distributions were obtained by the oxidative cleavage of graphite in the mixed acids with sulfonic acid and nitric acid (Figure 1a). The nanographenes were separated by dialysis using two membranes (2 kD and 15 kD) to give rise to nanographene NG-1, which were functionalized to yield NG-2. The click reaction of NG-2 resulted in NG-3, which was soluble in various organic solvents such as cyclohexane and 1,2-dichloroethane. The PL intensities of NG-3 in cyclohexane increased upon increasing the temperatures from 25 °C to 70 °C (Figure 1b). On the other hand, the PL intensities of NG-3 in 1,2-dichloroethane slightly decreased with increasing the solution temperature (Figure 1c). Accordingly, NG-3 showed the self-assembling behavior in cyclohexane, whereas 1,2-dichloroethane interfered with the self-assembly.

2A3b Determination of the phase composition of bentonite powders used for the sorption of nickel ions

Yudin Alexander, Kanygina Olga, Salnikova Elena, Osipova Elena

Chemistry Department, Orenburg University, Russia

The article is devoted to the study of the phase composition of bentonite clays of the Republic of Khakassia. It was found that the main mineral of the studied clay is montmorillonite. When studying the sorption of nickel ions on bentonite powder, it was found that the sorption process predominantly proceeds according to the physical mechanism.

Key words: bentonite, X-ray diffraction pattern, phase composition, sorption.

Modern technologies for the extraction of non-ferrous metals from various objects are based on the processes of sorption and extraction. Sorption consists in the absorption by a solid or liquid phases substances from environment.

Bentonite clays are highly colloidal, plastic, water-swelling clays which formed as a result of the decomposition of volcanic ash and a number of rock-forming processes occurring in hydrothermal conditions. Basically, bentonites clays are composed of minerals of the montmorillonite group: directly montmorillonite, beidellite, nontronite, hectorite, saponite. Montmorillonite clays have a high efficiency of extraction of nickel ions from aqueous solutions, which opens up wide possibilities of using natural and modified montmorillonites for the creation of sorbents [1].

A number of researchers have proofed that the mechanism of sorption of bentonites clays includes molecular adsorption and ion exchange [2]. The maximum sorption capacity of modified bentonite can reach 80 mg/g (in terms of hydrogen ions), modified (acid treatment) - up to 321 mg/g.

For a full studies of the processes, which penetrate at sorption of nickel on bentopowders, it is important to carry out a complex study of the structure of substances, including by methods of X-ray structural analysis. The identification of the phases that included in clays is an indispensable process for assessing the sorption capacity of a natural object.

The purpose of this work was to establish the phase composition of natural bentonite clays, bentonite powders which was calcined at 1000 °C and clays that adsorbed nickel ions, by X-ray phase analysis using a RADIANT DR-1 diffractometer. The object of the study was bentonite clay, which contains Na-montmorillonite. Researching clay was from the 10th Khutor deposit in the Ust-Abakan region of the Republic of Khakassia.

Parameters for recording diffraction patterns: copper radiation from an X-ray tube ($\text{CuK}\alpha$, $\lambda = 1.540598 \text{ \AA}$). Anode tube voltage: 30 kV, anode current: 5mA. Scanning range: 12 to 80 2θ , step: 0.02 2θ , scanning speed - 0.1 deg/min. The diffraction spectra were measured in the Bragg-Brentano geometry.

Diffraction patterns of clay that was adsorbed nickel ions were recorded on an MD-10 mini-diffractometer. Copper radiation, anode current 4 mA, voltage 24 kV, two-beam X-ray optical scheme.

The diffractogram of air-dry clay (figure 1) shows sets of lines belonging to several phases. The search for a correspondence in the databases of powder diffraction patterns (Crystallography Open Database, American Mineralogist Crystal Structure Database, PDF-2 Release 2004) made

it possible to identify them as the following phases: montmorillonite ($\text{Na}_x(\text{Al,Mg})_2\text{Si}_4\text{O}_{10}(\text{OH})_2 \cdot z\text{H}_2\text{O}$), anorthite ($(\text{Ca,Na})(\text{Si,Al})_4\text{O}_8$), silicon oxide (SiO_2).

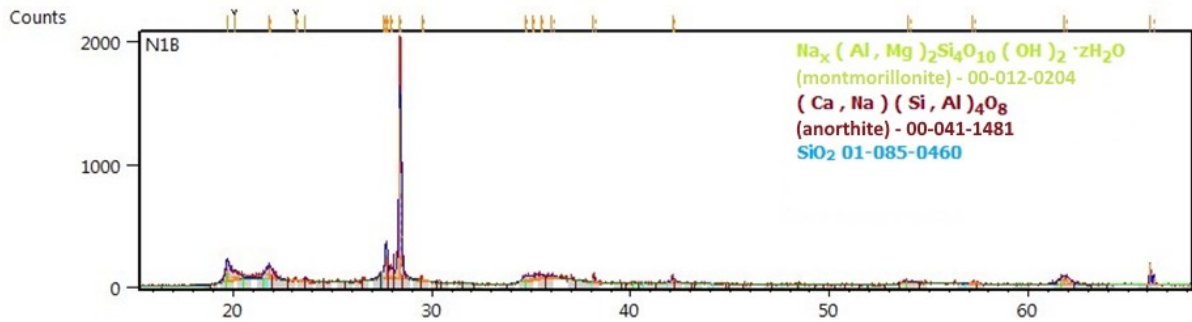


Figure 1 - X-ray powder diffractogram of Na-bentonite clay

The powder diffraction pattern of bentonite treated at 1000 °C (figure 2) shows two phases: aluminosilicate with a composition corresponding to the formula $\text{Na}_{0,4}\text{Ca}_{0,6}\text{Al}_{1,6}\text{Si}_{2,4}\text{O}_8$, referring to a row of plagioclase – probable product of thermal destruction of anorthite; second phase - silicon oxide (SiO_2). It is necessary to note an increase in the intensity of reflections of silicon oxide and the absence of reflections of montmorillonite – when processing above 800 °C various primary phases begin to form in montmorillonite: spinel, quartz. Since the spinel phase has no definite composition, its lines in the diffractogram are blurred.

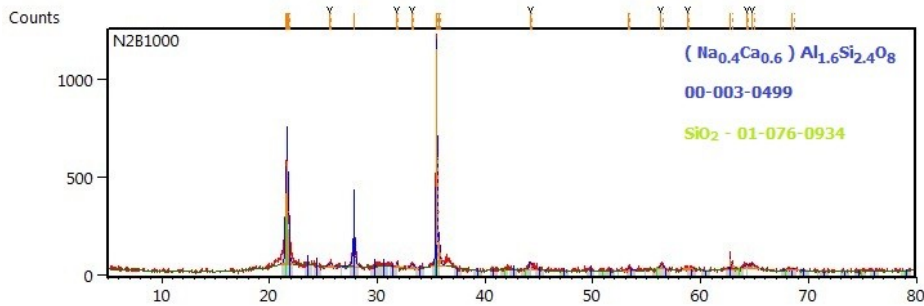


Figure 2 - X-ray powder diffractogram of Na-bentonite clay calcined at 1000 °C

When comparing diffraction patterns of air-dry bentonite, and bentonite sorbed nickel (figure 3) it is seen that the latter has a number of reflexes corresponding to the following compounds: $\text{Ni}(\text{OH})_2$, NiCl_2 , $\text{NiCl}_2 \cdot 6\text{H}_2\text{O}$ (таблица 2).

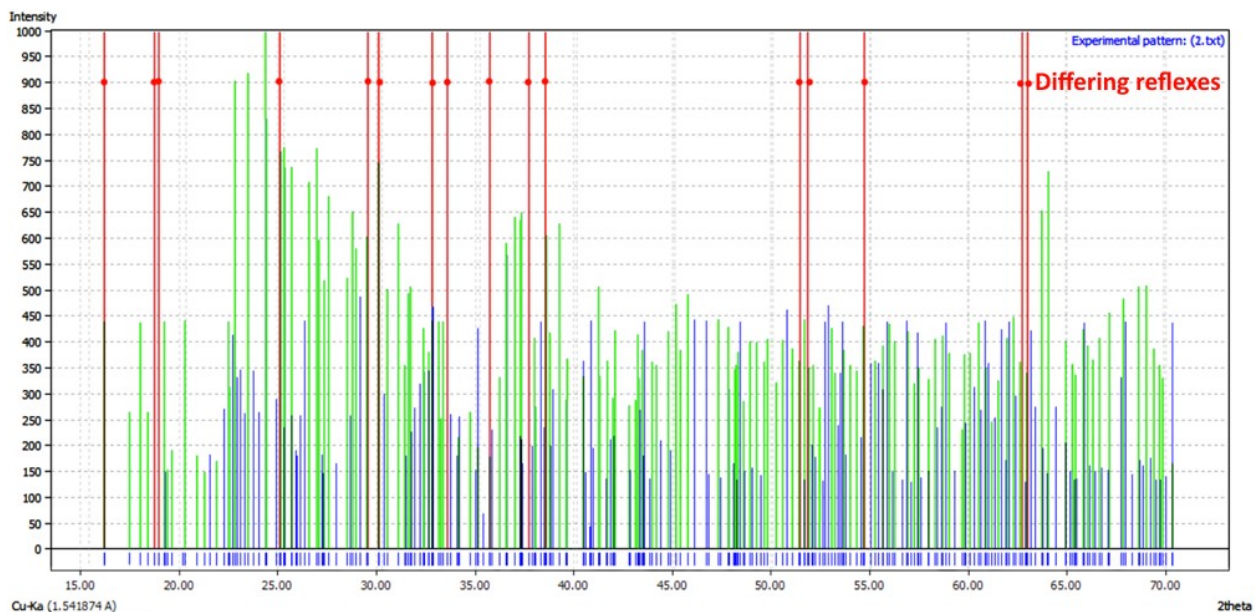


Figure 3 - Comparison of diffraction patterns of air-dry bentonite (blue lines) and bentonite that has absorbed nickel (red lines - different reflections)

Table 2 - Interpretation of the difference in diffraction patterns bentonite - bentonite-nickel

$2\Theta, ^\circ$	$2\Theta_{ref}, ^\circ$	Cards	Phase
16,19	16,17	99-101-2381	$\text{NiCl}_2 \cdot 6\text{H}_2\text{O}$
18,73	18,64	99-101-2381	$\text{NiCl}_2 \cdot 6\text{H}_2\text{O}$
18,97	19,25	99-100-9039	$\text{Ni}(\text{OH})_2$
25,12	25,27	99-101-2381	$\text{NiCl}_2 \cdot 6\text{H}_2\text{O}$
29,56	29,57	99-101-0725	NiCl_2
30,14	30,15	99-101-2381	$\text{NiCl}_2 \cdot 6\text{H}_2\text{O}$
32,83	32,86	99-101-2381	$\text{NiCl}_2 \cdot 6\text{H}_2\text{O}$
33,61	33,75	99-101-2381	$\text{NiCl}_2 \cdot 6\text{H}_2\text{O}$
35,76	35,73	99-101-2381	$\text{NiCl}_2 \cdot 6\text{H}_2\text{O}$
	35,86	99-101-0725	NiCl_2
37,75	37,79	99-101-0725	$\text{NiCl}_2 \cdot 6\text{H}_2\text{O}$
38,53	38,62	99-100-9039	$\text{Ni}(\text{OH})_2$
40,83	40,87	99-101-2381	$\text{NiCl}_2 \cdot 6\text{H}_2\text{O}$
44,24	44,27	99-101-2381	$\text{NiCl}_2 \cdot 6\text{H}_2\text{O}$
51,47	51,59	99-101-0725	NiCl_2
51,85	51,88	99-101-2381	$\text{NiCl}_2 \cdot 6\text{H}_2\text{O}$
54,74	54,71	99-101-2381	$\text{NiCl}_2 \cdot 6\text{H}_2\text{O}$
62,69	62,76	99-101-2381	$\text{NiCl}_2 \cdot 6\text{H}_2\text{O}$
63,01	62,90	99-100-9039	$\text{Ni}(\text{OH})_2$

Thus, according to the results of phase analysis, the main mineral of the studied bentonite clay from the "10th Khutor" deposit of R. Khakassia is montmorillonite (semi-quantitative assessment by the method of reference intensity ratio – 90,9%) [3].

Since the diffraction pattern of the clay that adsorbed nickel from the model solution is dominated by reflexes NiCl_2 , it can be concluded that physical sorption predominates in the mixed sorption process (chemical sorption is due to the formation of nickel hydroxide – $\text{Ni}(\text{OH})_2$).

Bibliography:

- 1 Sviridov A. V. Sorption of copper and nickel cations on layered materials / A. V. Sviridov [et al.] // Sorption and chromatographic processes. – 2016. – T. 16. – №1. – P. 78 – 86.
- 2 Kostin A.V. Peculiarities of sorption of nickel and copper ions on bentonite clay of the Zyryansk deposit, Kurgan region / A. V. Kostin [et al.] // Vestnik SUSU. Series: Chemistry. – 2009. – №12(145). – P. 37 – 41.
- 3 Liu, Z. R. Adsorption of copper and nickel on Na-bentonite / Z. R. Liu., S. Q. Zhou // Process safety and environmental protection. – 2010. - Vol. 88. – №1. – P. 62 – 66.
- 4 Aljlil, S. A. Adsorption of Cu & Ni on bentonite clay from waste water / S. A. Aljlil, F. D. Alsewailem // Athens Journal of Natural & Formal Sciences. – 2014. – №1(1). – P. 21 – 30.

2A4b

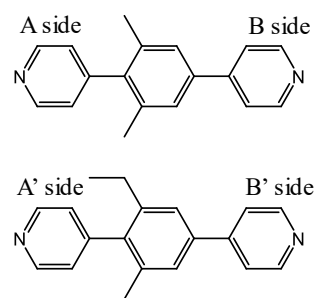
Steric effect by substituents on spin state of iron(II) assembled complexes using low symmetry bis(4-pyridyl)benzene derivatives

Akane Kato,¹ Satoru Nakashima^{1,2,3}¹ Department of Chemistry, Graduate School of Science, Hiroshima University² Department of Chemistry, Graduate School of Advanced Science and Engineering, Hiroshima University,³ Natural Science Center for Basic Research and Development, Hiroshima University

Self-assembled iron(II) complexes in which the central metals are bridged by ligands may show spin crossover (SCO) phenomenon between high-spin (HS) state and low spin-state (LS) state depending on temperature change. Fe(II)-N distance decreases by 0.2 Å from HS to LS state. Therefore, local structure around iron becomes important to show SCO. SCO coordination polymers using 1,4-bis(4-pyridyl)benzene (bpb) and the anionic ligand NCX⁻ (X = S, Se, BH₃), [Fe(NCX)₂(bpb)₂]_n·solvent were investigated by Wu et al., and [Fe(NCBH₃)₂(bpb)₂]_n·2CH₂Cl₂·2C₂H₅OH showed an abrupt spin transition at 250 K.^[1] Our research group has studied the effect of a methyl substituent of

1,4-bis(4-pyridyl)benzene (bpb) derivatives, i.e., 1,4-dimethyl-bis(4-pyridyl)benzene (= dmbpb) and 1,2,4,6-tetramethyl-bis(4-pyridyl)benzene (= tmbpb) to control SCO behaviors. [Fe(NCBH₃)₂(dmbpb)₂]_n showed spin transition at 125K, while [Fe(NCBH₃)₂(tmbpb)₂]_n kept the HS state. The cause of decrease in $T_{1/2}$ and SCO-off on these complexes was concluded to be due to the steric repulsion.^[2] In this study, we introduced the low symmetry bridging ligands, 2,6-dimethyl-bis(4-pyridyl)benzene = 2,6-dmbpb (A-B) and, 2,6-diethyl-bis(4-pyridyl)benzene = 2,6-debpb (A'-B') which were expected to introduce un-uniformity into local structure around iron atom. We synthesized [Fe(NCX)₂(L)₂]_n (X = S, Se, BH₃; L = 2,6-dmbpb, 2,6-debpb) and discussed the SCO behavior.

X-ray structural analysis of [Fe(NCBH₃)₂(2,6-dmbpb)₂]_n revealed that local structure around iron is FeAB₃(15%), FeA₂B₂(70%), and FeAB₃(15%). Magnetic susceptibility of [Fe(NCBH₃)₂(2,6-dmbpb)₂]_n revealed that 85% of iron showed SCO at $T_{1/2}$ = 95K. We tried to explain the incomplete SCO (85%) using DFT calculation that the irons having local structure FeAB₃(15%) and FeA₂B₂(70%) show SCO. X-ray structural analysis of [Fe(NCBH₃)₂(2,6-debpb)₂]_n did not have any disorder and revealed that local structure around iron is A'₂B'₂. We suppose that the bulky ethyl group forced the local structure A'₂B'₂. Powder sample was suggested to have two types of crystals from the PXRD patterns. And ⁵⁷Fe Mössbauer spectra revealed that 21% of iron showed SCO. We are now considering the other structure.



Scheme 1. 2,6-dmbpb(top) and 2,6-debpb(bottom)

Reference

[1] Xue-Ru Wu, et al., *Inorg. Chem.*, **54**, 2015, 3773-3780.

[2] Keisuke Yoshinami, et al., *Radioisotopes.*, 2017, **66**, 625-632.

2B1b Synthesis and Characterization of a Digallane Gold Complex with a 12-Electron Auride Center

- Shozo Matsumae¹, Rong Shang¹, Kohei Susukida¹, Leonardo I. Lugo-Fuentes², Kazuki Nakanishi¹, Masaaki Nakamoto¹, Yohsuke Yamamoto¹, Joaquín Barroso-Flores³, J. Oscar C. Jimenez-Halla²

¹ Department of Chemistry, Graduate School of Advanced Engineering and Science, Hiroshima University

² Department of Chemistry, Division of Natural and Exact Sciences, University of Guanajuato

³ Centro Conjunto de Investigación en Química Sustentable UAEM-UNAM, Unidad San Cayetano

Gold complexes with coordination number between 2 and 4 are usually stable 14- and 16-electron species. Singly coordinated gold (L = neutral 2-electron ligand) complex [AuL]⁺ with a 12-electron Au(I) center is highly electron deficient and thus highly reactive. Therefore, *in situ* generation of 12-electron [AuL]⁺ has been used to increase the efficiency of homogeneous gold catalysts for substrate coordination. Although isolation and characterization of one-coordinate gold complexes have been attempted with sterically hindered substituents, no example has been reported.

Meanwhile, 12-e⁻ gold has also been studied as auride (Au⁻). Exemplifying such gold complexes has long been a synthetic challenge. A series of experimental studies have authenticated the stability of monoatomic auride center. Although its chemical behavior toward organic substrate has been investigated by using computational and physical techniques, their preference to form clusters prevents the formation and isolation of molecular, mononuclear, low-valent gold complexes.

Previously, our group has demonstrated the controlled selectivity for σ -bond metathesis between the B–B bond and Au–L/Cl bond by the complexation of tri(*tert*-butyl)azadiboriridines with gold (I) complexes¹. In the resulting structures (Figure 1), the two borane moieties accept one-/two-electron donors, while the electron

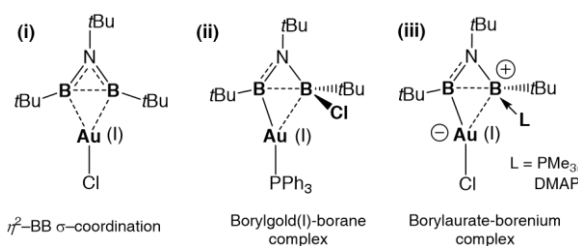
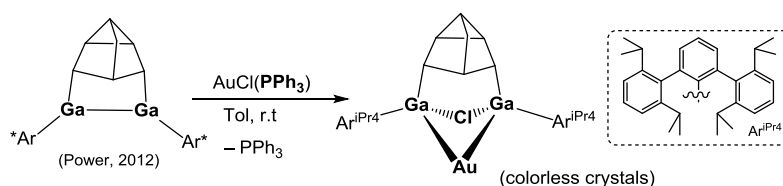


Figure 1. Diboron gold complex (Our previous work, 2018)

density on the B–B bond is donated to the more electron negative gold center to form B–Au bond.

We applied the same strategy to gallium and investigated the reaction of cyclodigallane with Au precursor. Power's digalladeltacyclane² with a rigid and saturated backbone was employed as digallium ligand precursor to eliminate any possible side reactions. Recently, we obtained a digallium gold complex through a reaction of digalladeltacyclane with AuCl(PPh₃)³ (Scheme 1).

Its structure was characterized by X-ray



Scheme 1. The formation of digallium gold complex

crystallography (Figure 2), which features a chlorine, gold-bridged digallium complex with complete cleavage of Au–Cl bond.

To obtain more detailed insight into the bonding situation in digallium gold complex, computational studies were carried out. Figure 3 shows the Natural Hybrid Orbitals (NHOs) in the Ga–Au–Ga fragment. NHOs **A** and **B** are mostly constructed from 4p orbitals of Ga atoms. The NHO **C** constitutes mostly all the Au 6s orbital. Moreover, no Natural Bond Orbital (NBO) was found between both Ga atoms. These results indicated this Ga–Au–Ga 3-centered bond was different from an usual 3-center 2-electron bonding. Analysis of the Laplacian of electron density of digallium gold complex was performed in terms of Electron Localized Function (ELF) to look further into the nature of the 3-centered bond (Figure 4). The large cyan region between Au and Ga atoms reveals the existence of the weak bonding interaction, whereas the dark blue region indicates no interaction between Ga atoms. Therefore, we could conclude this bonding situation was a 3-center 2-electron banana bond.

Furthermore, Natural Atomic Orbital Occupancies for Au showed filled 6s and 5d orbitals, while all 6p orbitals were vacant. This result implies that the Au center has 12 electrons as auride. Thus, it was concluded that the complexation of digalladeltacyclane with AuCl(PPh₃) resulted in digallium gold complex with the reduction of Au (I) to 12-e⁻ auride by the σ Ga–Ga bond. The investigation for the reactivity of this novel digallium gold complex is underway.

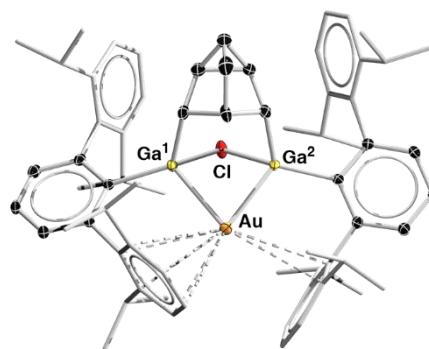


Figure 2. X-ray structure of digallium gold complex

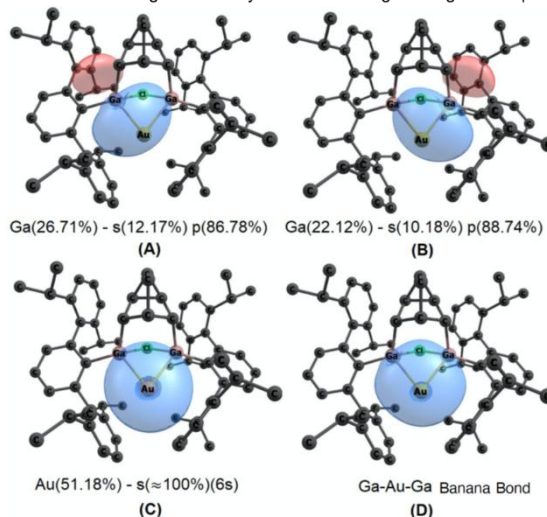


Figure 3. Natural hybrid orbital composition (A-C) of the bent bond for the Ga-Au-Ga (D) moiety

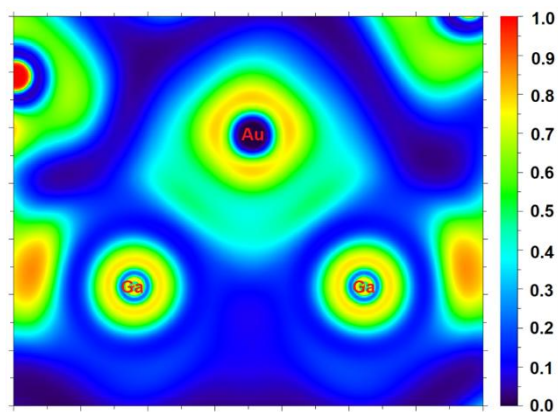


Figure 4. Electron localized function (ELF) plot on the Ga–Au–Ga plane

- [1] Shang, R.; Saito, S.; Jimenez-Halla, J. O. C.; Yamamoto, Y. *Dalton Trans.* **2018**, *47*, 5181– 5188.
- [2] Caputo, C. A.; Guo, J.-D.; Nagase, S.; Fettinger, J. C.; Power, P. P. *J. Am. Chem. Soc.* **2012**, *134* (16), 7155– 7164
- [3] Susukida, K.; Lugo-Fuentes, L. I.; Matsumae, S.; Nakanishi, K.; Nakamoto, M.; Yamamoto, Y.; Shang, R.; Barroso-Flores, J.; Jimenez-Halla, J. O. C. *Organometallics.* **2020**

2B2b

Generation and propagation of acoustic waves in condensed matter

Tsyurko Dmitry, Letuta Sergey, Pashkevich Sergey.

Faculty of Physics, Orenburg University, Russia

The main processes occurring in a matter upon excitation of sensitizers by powerful (saturating) laser radiation of a state have been established: stepwise absorption of two quanta by molecules through real lower excited electronic states, population of triplet states, local growth of the matter and formation of vapor bubbles, generation and propagation of acoustic waves.

Key words: *high electronically excited states, local heating, shock waves.*

Generation and propagation of shock acoustic waves in various solutions is experimentally investigated. Shock waves in liquids arise as a result of a rapid increase in temperature during nonradiative relaxation of electronically excited states of thermosensitizers (TS). At ambient temperature the boiling point, then evaporation of the liquid takes place and shock waves generate vapor bubbles. Shock waves are generated simultaneously in the process of local thermal expansion of the medium and the formation of vapor bubbles.

Organic dyes were used as TS for generating shock waves. The processes of generation and propagation of waves in different viscosities - water, ethyl alcohol, saline solution, ethylene glycol, propylene glycol, glycerin - have been studied.

Thermal sensitizer dye molecules were excited by nanosecond laser pulses. The radiation of a YAG: Nd laser (second harmonic, 532 nm) was focused using a cylindrical lens onto an area of 3.0 x 0.3 mm² near the end wall of a rectangular quartz cell in which the solutions were placed. The excitation density is maximum at the focus of the lens and was controlled within the range of 0.1 - 50 MW / cm². When excited, local heating occurs and vapor bubbles are generated. It is this region that is the extended shock waves of axial symmetry.

The shock wave arising during local heating, propagating in the matter, changes the refractive index of the solution. The change in the refractive index in this region of the solution was recorded by the refraction of the probe beam of the He - Ne laser. The probe beam (632 nm, cross section less than 1 mm, power less than 1 mW), having passed through the solution, fell on the entrance slit of the monochromator, behind which was a photodetector (photomultiplier tube). When the wave crosses the probe beam, refraction occurs, and the light falling on the photodetector (FMT-84) is reduced. After the passage of the wave, the intensity of the probing light was restored to its original value.

If the TS has a large quantum yield to the triplet state, then on the kinetic transmission curve one can observe not only the shock wave profile, but also the induced triplet-triplet absorption. In fig. 1, characteristic kinetic curves of the probing beam transmission under pulsed excitation of erythrosine with a concentration of 0.25 mM in saline at different distances from the excitation zone: curve 1 - 0.1 mm; curve 2 - 0.2 mm, curves 3 and 4 - excitation zones.

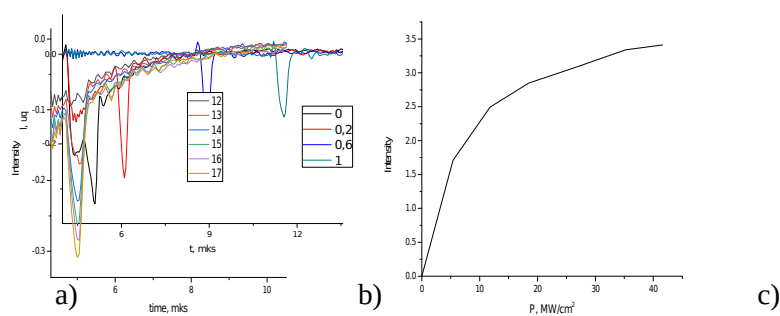


Figure: 1 a) kinetic curves of the probing beam transmission under pulsed excitation of erythrosine (0.25 mM) in saline at different distances from the excitation zone; Kinetic curves (b) and a graph of the dependence (c) of the shock wave intensity on the power density of pumping eosin (0.5 mM) in water.

The short-lived (about 5 μs) induced triplet-triplet absorption of light by excited dye molecules is clearly seen in curves 1 and 2. At distances greater than 5 mm, triplet-triplet absorption is no longer manifested, which can be seen from curves 3 and 4.

All curves show sharp dips, which correspond to the moments of crossing the probe beam by the shock front. The speed of propagation of the detected waves coincides with the speed of sound in water (1505 m / s, at 26 $^{\circ}\text{C}$) and depends on the temperature of the solution - with an increase in temperature to 80 $^{\circ}\text{C}$, the speed increased to 1555 m / s, and when the solution was cooled to 0 $^{\circ}\text{C}$, it decreased to 1410 m / s.

The dependence of the efficiency of generation of shock waves on the type of dyes, their concentration, air pressure above the surface of solutions, and the power density of the exciting radiation is studied. The optimal TS concentration under the conditions of our experiments was (0.25 - 0.50) mM.

At a power density of the exciting radiation $P < 0.5 \text{ MW} / \text{cm}^2$, shock waves in solutions with dyes have a very low intensity and their experimental registration is difficult (Fig. 1b, c). If P exceeded $5 \text{ MW} / \text{cm}^2$, acoustic waves were reliably recorded both in solutions with dyes with high values of the quantum yield to the triplet state (halogen-substituted fluoresceins) and with dyes with a low yield of triplet states (rhodamines). This is due to the high heat release in solutions. At $P > 10 \text{ MW} / \text{cm}^2$, each TS molecule during the action of the exciting pulse ($\tau = 15 \text{ ns}$) can repeatedly absorb exciting quanta, making the $S_1 \leftrightarrow S_n$ transitions (as well as $S_1 \rightarrow S_n \rightarrow T_m \rightarrow S_1$, or $T_1 \leftrightarrow T_m$, or $T_1 \rightarrow T_m \rightarrow S_1 \rightarrow T_1$), each of which is accompanied by heat release. Since the absorption bands $S_0 \rightarrow S_1$, $S_1 \rightarrow S_n$, and $T_1 \rightarrow T_m$ overlap strongly in the dyes studied by us, then when a substance is exposed to intense radiation, all of the above transitions are simultaneously excited.

The practical significance of the work lies in the ability to control the process of generation and propagation of acoustic waves in condensed media, which can be used in optics, biophysics and other related industries.

2B3b

Self-assembling behaviors of platinum(II) complexes possessing hydrophilic triethylene glycol chains

Masaya Yoshida, Takehiro Hirao, Takeharu Haino

Graduate School of Advanced Science and Engineering Hiroshima University

The self-assembly of small molecules is a powerful tool for the development of discrete supramolecular organizations, which display attractive optical, magnetic, mesogenic, and macroscopic properties. We reported a luminescent micelle formed through the self-assembly of a TEG-equipped platinum(II) complex **1**.¹ The micelle formation was driven by hydrophobic forces as well as intermolecular Pt–Pt interactions.

In this presentation, we will describe the self-assembling behaviors of (*R*)- and (*S*)-**2** possessing the stereogenic centers on the TEG side chains (Figure 1). The self-assembling behavior of (*S*)-**2** was studied in chloroform and in toluene. The ¹H NMR signals of (*S*)-**2** were concentration-dependent in chloroform-*d*₁. The aromatic protons of (*S*)-**2** shifted upfield upon increasing the solution concentration, which indicates that (*S*)-**2** formed the stacked assemblies. Emission band at 800 nm was assigned to the MMLCT band of (*S*)-**2**, indicating the formation of the stacked assemblies with the Pt–Pt interaction. The CD spectra of (*S*)- and (*R*)-**2** displayed a mirror image relationship, suggesting that (*S*)- and (*R*)-**2** formed helically twisted assemblies, and the helical sense was directed by the chiral side chains. Transmission electron microscopy (TEM) and atomic force microscopy (AFM) revealed the morphological insight into the assemblies of (*S*)-**2**. The stacked assemblies formed the 2D sheet-like nano structures, which were most likely directed by the Pt–Pt interactions.

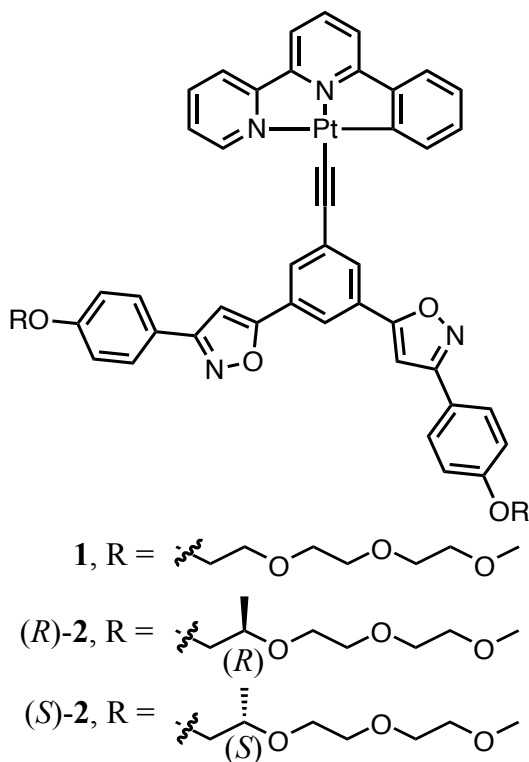


Figure 1. Molecular structures of platinum complexes.

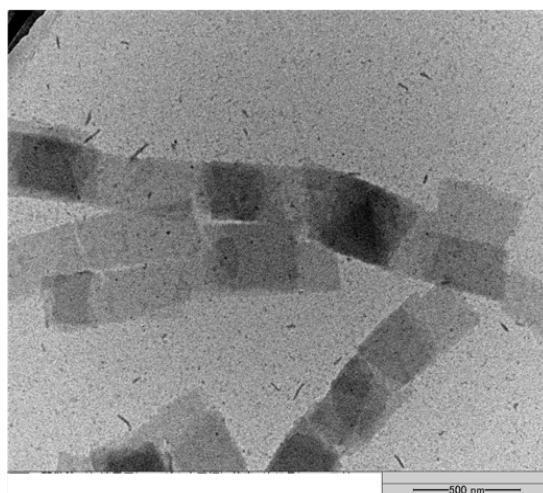


Figure 2. TEM image of (*S*)-**2**.

[1] T. Hirao, H. Tsukamoto, T. Ikeda and T. Haino, *Chem. Commun.*, **2020**, 56, 1137-1140.

2B4b Molecular dynamic simulation of the conformational structure rearrangement of polyampholyte polypeptides on the surface of a metal nanoparticle in an ultrahigh-frequency electric field

Kruchinin Nikita, Kucherenko Michael

Center of Laser and Information Biophysics,
Orenburg State University, Orenburg, Russia

Molecular dynamics has been employed to study conformational rearrangements of polyampholytic polypeptides adsorbed on the surface of a metal nanoparticle, with the rearrangements being caused by changes in the direction of particle polarization at a frequency corresponding to ultrahigh-frequency electric field. With a periodic change in the direction of polarization of the nanoparticle, in one case, fluctuations in the conformational structure of the adsorbed polyampholyte polypeptide were observed. In another case, the formation of a macromolecular ring was observed in the equatorial region of the nanoparticle.

Keywords: molecular dynamics, polyampholytes, metal nanoparticle, ultrahigh-frequency electric field

Metal nanoparticles with macromolecules adsorbed on their surface are widely used in many fields of science and technology, in particular, when creating chemical sensors, as well as in biochemical and biomedical studies. Of particular interest is the development of methods for the control over conformational rearrangements of macromolecular chains adsorbed on a nanoparticle surface under the action of electromagnetic radiation. In an electric field, electric charges are induced on the surface of a metal nanoparticle, with the density of the charges being distributed over the surface in proportion to the cosine of the angle between the directions of the electric field vector and the normal vector at a point on the nanoparticle surface. Therefore, an electric field, which is uniform at a distance from a nanoparticle, is strongly distorted near it [1-3].

Upon the action of electromagnetic radiation on a nanosystem in which the polyampholyte is adsorbed on a metal nanoparticle, the conformational structure of macrochains will vary in accordance with fluctuations in the density of the charges induced by the field on the nanoparticle surface. When plasmon oscillations are excited in a nanoparticle, a local electric field is enhanced near it. In this case, the effect of the enhancement–weakening of the attraction between monomer units and the nanoparticle surface becomes noticeable upon the activation of high-frequency plasmon modes, i.e., in the plasmon resonance frequency range, while the initiation of conformational transitions in macrochains near the nanoparticle becomes possible only upon excitation of ultrahigh-frequency vibrations in it. In the latter case, the matter concerns not the plasmon resonance, but rather the plasmonic activation of the conformational mobility of polypeptide fragments. At certain frequencies of electromagnetic radiation, a resonance of variations in the conformational structure of a polyampholytic macromolecule on the surface of a metal nanoparticle becomes possible [3].

Molecular dynamics simulation (NAMD 2.13 [4], CHARMM22 [5]) was performed for a molecular system in which a polyampholyte polypeptide was located on the surface of a spherical gold nanoparticle (radius 1.5 nm). Four polyampholytic polypeptides with different arrangements of charged amino acid residues were examined:

- 1) A200R50D50 consisting of 300 amino acid residues, namely, 200 Ala (A) units, 50 Asp units (D), and 50 of Arg units (R), with the two latter being uniformly distributed over the chain - (ADAARA)₅₀;

- 2) A240R30D30 polypeptide – (AADAAAARAA)₃₀;
- 3) A320R40D40 polypeptide – (A₄RRA₈DDA₄)₂₀;
- 4) A272R16D16 polypeptide – A₈(A₈DDA₁₆RRA₈)₈A₈.

The entire nanosystem was placed in a 20 nm cube filled with water molecules. The simulation was carried out at constant temperatures of 300 and 900 K (Berendsen thermostat) for each considered polypeptide.

Local electric fields were specified by varying atomic charge values on the surface of the spherical nanoparticle according to the cosine law for the orientation angle of the normal. During the MD simulation, the densities of these charges were periodically varied with time according to the sine law with oscillation period $T = 2.4$ ns (oscillation frequency of 416.7 MHz) for 3–5 oscillation periods. The peak value of the induced dipole moment of the polarized nanoparticle was $P_{\max}^{np} = 10.92kD$. Each oscillation period was divided into 8 equal time periods of 0.3 ns, during which the field remained unchanged, and the dipole moment of the nanoparticle in a selected period was set by averaging it over the entire period duration.

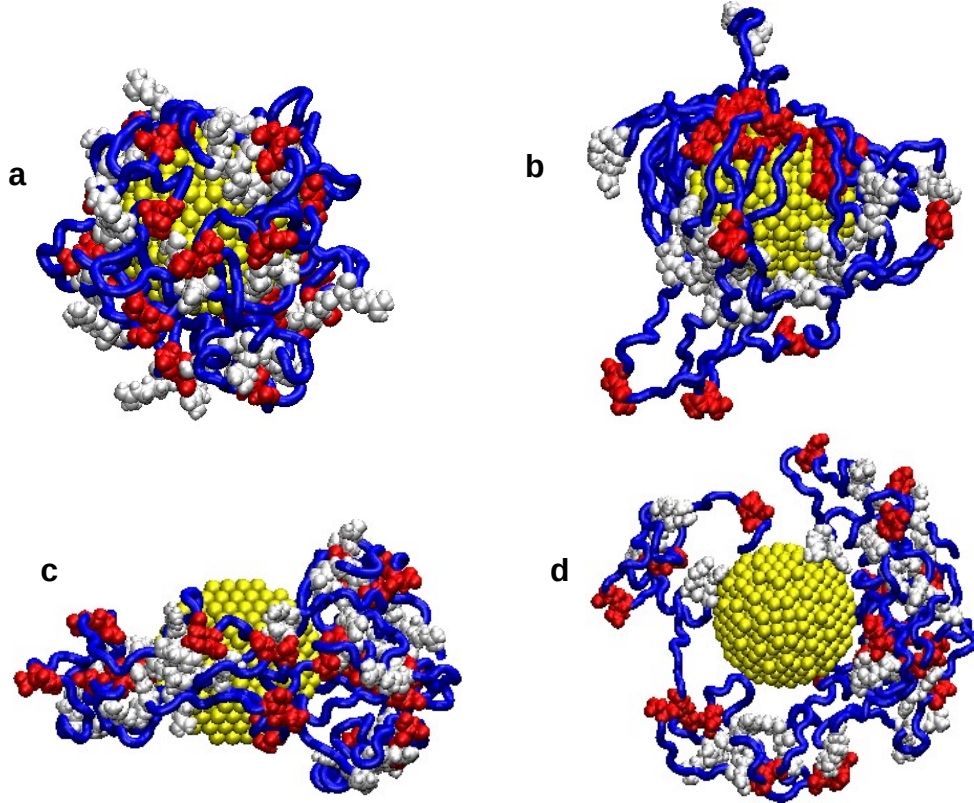


Fig. 1. Conformations of A200R50D50 polypeptide in the course of MD simulation with periodic changes in the polarization of the nanoparticle: a) starting conformation; b) conformation in 10.2 ns at 900 K, when nanoparticle dipole moment is directed upward; c) and d) at the end of the MD simulation at 300 K (c - side view, d - top view). On the figure: blue tube and white and red symbols denote Ala, Arg, and Asp residues, respectively.

The MD simulation performed at 900 K with periodic changes in the polarity of a gold nanoparticle under the action of an electric field has revealed fluctuations in the conformational structure of polyampholytic polypeptides adsorbed on the particle surface. Figure 1A shows the starting conformation of the A320R40D40 polypeptide, and figure 1B shows its conformation at the time of 10.2 ns (the dipole moment of the nanoparticle is directed upwards) during the last, fifth oscillation period. It can be seen that the conformational rearrangements were accompanied

by the adsorption of negatively charged Asp units of the polypeptides on the surface of the nanoparticle pole that was positively charged at the given time moment. In Figs. 1b, this pole is located in the upper part of the nanoparticle. Arg residues were adsorbed on the surface of the nanoparticle pole that was negatively charged at this time moment; this pole is located in the lower part of the nanoparticle.

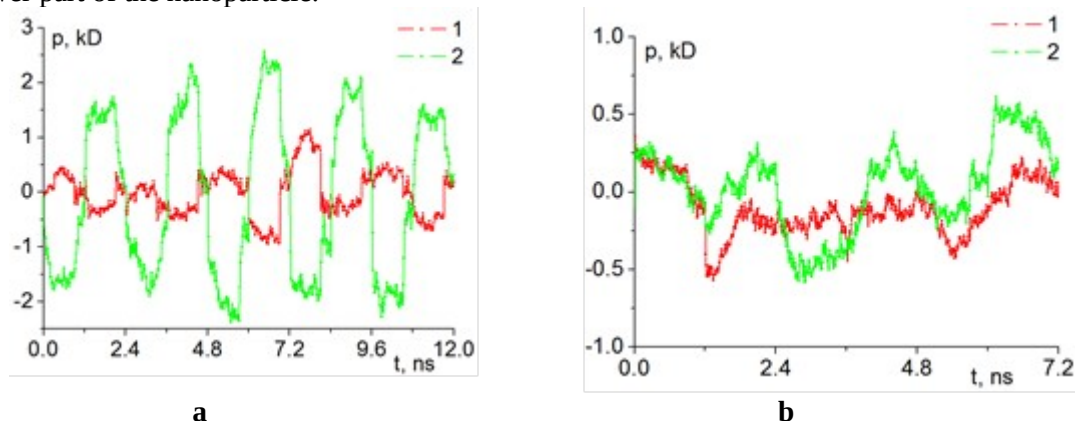


Fig. 2. Projections of the dipole moments of (1) A200R50D50 and (2) A320R40D40 polypeptides in the direction of the gold nanoparticle polarization vector as functions of the time of MD simulation at (a) 900 and (b) 300 K.

Figure 2a shows that periodic oscillations of the projection of the dipole moment of polyampholyte polypeptides in the direction of the polarization vector of the nanoparticle are observed. This suggests that a change in the local electric field near the surface of the metal nanoparticle is followed by a change in the conformational structure of the macromolecule. It can be seen that A200R50D50 polypeptide exhibits an increase in the projection of the macromolecule dipole moment with an increase in the dipole moment of the nanoparticle. On the contrary, the projection of the total macrochain dipole moment decreases for A320R40D40 polypeptide. This difference is due to the fact that the fringe of A200R50D50 polypeptide is elongated in the polar regions, and most of the dipole moments of polypeptide fragments bounded by oppositely charged units are oriented in the direction of the electric field. In this case, in A320R40D40 polypeptides, the majority of the charged units are shifted to the oppositely charged poles of the nanoparticle. This leads to the fact that the projection of the dipole moment of the entire macrochain is oriented in the opposite direction.

Figure 3 exhibits the radial dependences of the atom density for A320R40D40 polypeptide on the surface of the gold nanoparticle at the ends of the MD simulation at different time intervals in the cases of the nonpolarized nanoparticle (Fig. 3a) and that polarized with an upward dipole moments of (Fig. 3b). It is seen that the radial atom density distributions in one phase of variations in the surface charge density of the nanoparticle almost coincide with each other. The periodic changes in the local electric field of the nanoparticle with time lead to fluctuations in the conformational structure of the adsorbed polyampholytic polypeptide, with very different radial density distributions of polypeptide atoms corresponding to the polarized and nonpolarized states of the particle.

Moreover, different angular distributions of adsorbed polypeptide atoms correspond to the cases of the nonpolarized nanoparticle and that polarized in different directions (Fig. 4a and 4b). In the plots, abscissa axes represent the average angles corresponding to the selected spherical segments bounded by circles of different latitudes from the lower pole (-90°) to the upper one (90°).

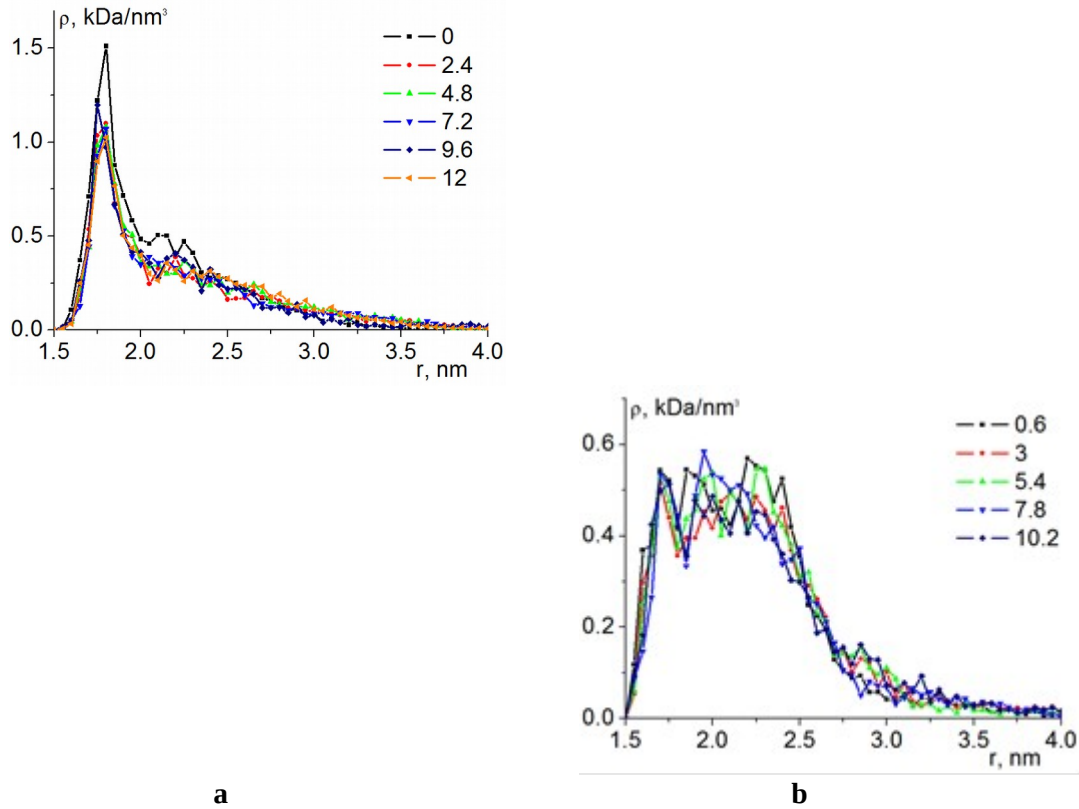


Fig. 3. Radial density distributions of A320R40D40 polypeptide atoms on gold nanoparticle surface at the ends of different time intervals of MD simulation at 900 K (nanoseconds, indicated in the figure field) for (a) nonpolarized nanoparticle and (b) polarized nanoparticle with upward dipole moment.

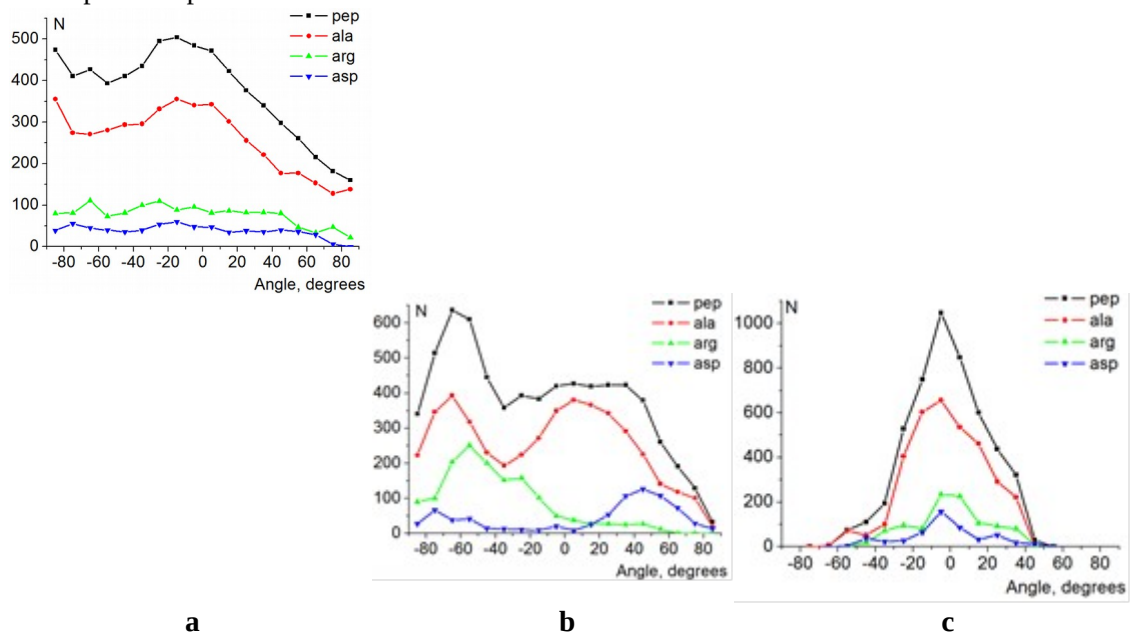


Fig. 4 Average angular distributions of A320R40D40 atoms over all conformations at the ends of different time intervals of MD simulation at 900 K for (a) nonpolarized nanoparticle, and (b) polarized nanoparticle with upward dipole moment. (c) Angular distribution of A320R40D40 polypeptide atoms at the end of the MD simulation at 300 K. Pep denotes angular

distributions for all polypeptide atoms; Ala, Arg, and Asp denote the angular distributions differentiated over the types of amino acid residues.

The MD simulation with periodic changes in the gold nanoparticle polarity with time at 300 K has revealed a shift of adsorbed polyampholytic polypeptide units to the equatorial region of the nanoparticle with the formation of a ring-shaped polypeptide fringe enveloping the nanoparticle. Figures 1c and 1d show the conformation of A320R40D40 polypeptides after 7.2 ns MD simulation at 300 K. Figure 2b presents the dependences of the dipole moment projections of polypeptides in the direction of the nanoparticle polarization vector on the time of MD simulation at 300 K. It can be seen that the amplitude of variations in the macrochain dipole moment projections is much smaller than that at 900 K (Fig. 2a). This is due to the fact that, at 900 K, the changes in the polarity of the nanoparticle were accompanied by shifts of the charged units from one pole to the other and the protrusion of macrochain loops in the polar regions. At 300 K, the changes in the dipole moment of a macrochain are associated with a reorientation of polypeptide fragments in the weakly charged equatorial region.

Figure 4c shows the angular distributions of A320R40D40 polypeptide atoms with differentiation over the types of units. These distributions correspond to the conformational structures shown in Figs. 1c and 1d. In this case, the peak of the maximum value of the angular distribution of the polypeptide atoms is in the equatorial region, and the angular distributions themselves hardly change upon repolarization of the nanoparticle. The differences observed in the rearrangement of the conformational structure of polyampholytic polypeptides when performing the MD simulation with periodic changes in nanoparticle polarity with time at 300 and 900 K are due to the fact that, when the polarity of the nanoparticle changes, charged units shift to the nanoparticle poles charged oppositely to these units. Upon the MD simulation at the high temperature, potential barriers between the macrochain units are overcome under the action of the local electric field of the polarized nanoparticle more easily than they are at the low temperature; therefore, the charged units are shifted from one pole to the other. At the low temperature, the polypeptide units bearing charges of different signs shifting to oppositely charged poles meet each other in the equatorial region where the local electric field of the polarized nanoparticle is weakest. Therefore, oppositely charged polypeptide units attract each other to form neutralized macrochain fragments, which cannot be separated into individual charged fragments under the influence of the weak local electric field of the equatorial region of the nanoparticle at 300 K.

Thus, the rearrangements occurring in the conformational structure of a polyampholytic polypeptide adsorbed on the nanoparticle upon periodic changes in the particle polarization direction are accompanied by two effects: fluctuations in the conformational structure of the polypeptide and the formation of a ring of macromolecules in the equatorial region of the nanoparticle.

Funding: This work was supported by the Russian Foundation for Basic Research and Orenburg oblast within the framework of project no. 19-43-560003; and the Ministry of Science and Higher Education of the Russian Federation within the framework of project no. FSGU-2020-0003

References

- [1]. Kruchinin N.Yu., Kucherenko M.G. // *Biophysics*. 2020. V. 65 (2). P. 186-194.
- [2]. Kruchinin N.Yu., Kucherenko M.G. // *Colloid Journal*. 2020. V. 82 (2). P. 136-143.
- [3]. Kruchinin N.Yu., Kucherenko M.G. // *Colloid Journal*. 2020. V. 82 (4). P. 392-402.
- [4]. Phillips J.C. et al. // *J. Comput. Chem.* 2005. V. 26. P. 1781-1802.
- [5]. MacKerell A.D. Jr. et al. // *J. Phys. Chem. B* 1998. V. 102. P. 3586-3616.

2C1b

Attempts to synthesize antiaromatic σ -dimer:

Silyl group conversion of cobalt complex

Airi Oguri¹, Masaaki Nakamoto¹, Rong Shang¹, Yohsuke Yamamoto¹¹ Graduate School of Advanced Science and Engineering, Hiroshima UniversityBackground

The expansion of a conjugated π -system is an important strategy for generation and stabilization of radical species, and therefore, has been widely applied in design of functional molecules in material chemistry involving electron-transfer processes. In considerations of design strategies for conjugated π -systems, two complementary concepts are of crucial importance, namely, aromaticity and antiaromaticity. Hückel in 1931, found that planar structures with sp^2 hybridized orbitals and $[4n+2]\pi$ electrons, such as benzene, are stabilized through the conjugated π -orbitals. Such stabilization effect was termed aromaticity. On the other hand, structures with $[4n]$ are found to avoid conjugated planar structures and were defined as antiaromatic compounds. Due to the stabilization effect of aromaticity and destabilization of antiaromaticity, design strategies for controlling conjugated π -system has been mostly limited to aromatic species. The effect of antiaromaticity remains less understood due to its high reactivity.

The highly reactive nature of antiaromatic compounds and their proneness to avoid conjugation through structural changes can be explained by consider their frontier orbitals. For example, the smallest $4n\pi$ annulene cyclobutadiene (CBD) with 4π electrons can adopt either a square geometry (Figure 1, **A**) with conjugation similar to that of benzene, or a rectangular geometry with single-double bond alternation (Figure 1, **B**). The HOMO of **A** is a set of doubly degenerate orbitals. Consequently, an open-shell, diradical species is expected, which explains its high reactivity. Through the structural change to the rectangular geometry with bond alternation (Jahn-Teller distortion), the HOMO loses degeneracy with a pair of electrons occupying the stabilized orbital. Also because of this, the HOMO-LUMO energy gap is very small in **B**. Numerous theoretical and experimental studies of the parent CBD in the ground state demonstrated that the rectangular structure is more favorable than the square diradical structure.

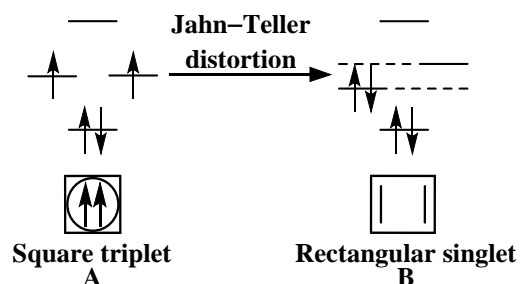
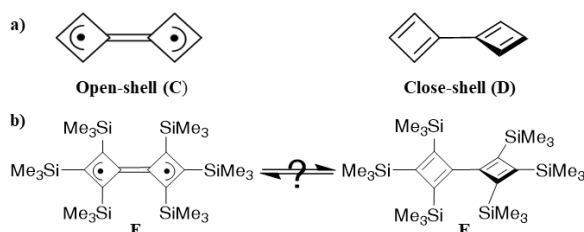


Figure 1. Electron configuration of CBD

Our group aims to understand structure-property relationship of antiaromatic systems through systematically investigating the structure, electronic properties and antiaromaticity of CBD derivatives. This project targets a σ -bond linked silyl-substituted bicyclobutadienyl (CBD σ -dimer), which can interact through σ -bond

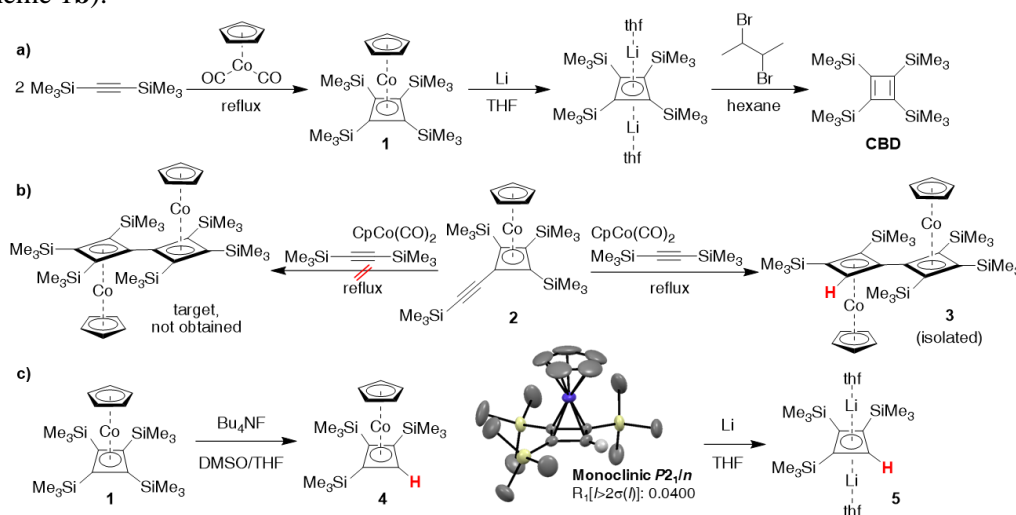
an open-shell diradical species (Figure 2, **E**) and a close-shell species with a non-planar structure (Figure 2, **F**). Although theoretical calculation¹⁾ on the parent CBD σ -dimer (Figure 2a) predicted the open-shell species (**C**) being more stable, it has not been verified experimentally. Here, we

Figure 2. CBD σ -dimer

describe the attempts to synthesize and characterize a silyl-substituted CBD derivative which represents the first example of a CBD σ -dimer. The large steric repulsion among trimethylsilyl substituents is expected to prevent the formation of the coplanar open-shell species **C**. The finding of this study will contribute to the rational design of new organic electronic devices based on extended π -conjugation of antiaromatic molecules.

Results

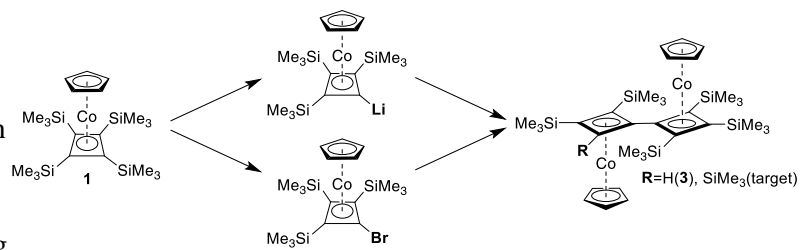
The synthesis of tetra-silyl substituted CBD has been established by our group, which involves formation of a CBD cobalt complex (**1**) for introduction of trimethylsilyl groups, followed by reductive demetallation using lithium metal and two-electron oxidation (Scheme 1a). For synthesis of the target CBD σ -dimer, this procedure has been modified to use the acetylene-substituted CBD cobalt complex (**2**). Instead of the target hexa-silyl-substituted CBD dicobalt complex, the penta-silyl-substituted CBD dicobalt complex (**3**) was obtained in small yield (11%). The observed desilylation is likely due to steric repulsion between the bulky trimethylsilyl groups (Scheme 1b).



Scheme 1. Synthetic routes

Further reductive demetallation of **3** was not successful. Initially, this was attributed to the less electron-accepting property of hydrogen compared to that of a trimethylsilyl group. To verify, the mononuclear tri-silyl-substituted CBD cobalt complex (**4**) was synthesized by desilylation from tetrabutylammonium fluoride (Scheme 1c). Contrary to our initial hypothesis, **4** can be reduced to form the dianionic species (**5**). A singlet at 5.66 ppm in the ^1H NMR spectrum, attributed to the skeleton hydrogen, and a singlet at -5.65 ppm in the ^7Li NMR spectrum clearly show a significant shift due to the aromatic ring current.

At present, we obtain following result; desilylation of **1** is possible, and hydrogenated CBD dianion **5** is accessible. We are going to investigate the halogenation and lithiation methods of **1** towards σ -dimer of CBD (Scheme 2).



Scheme 2. Future plan

Radiation and radiationless molecular processes in a near field of 2D-gratings with plasmonic nanoelements

Kucherenko Michael, Rusinov Alexander

Orenburg University, Center of Laser and Information Biophysics, Orenburg, Russia

E-mail: clibph@yandex.ru

Radiation and nonradiative processes in molecular systems over a quasi-two-dimensional lattice of plasmonic nanorods and spherical nanoparticles have been investigated. The simulation of the electromagnetic field of optical frequency in periodic structures composed of parallel conducting nanorods - in the quasi-static approximation and the FDTD method, as well as conducting and composite spherical nanoparticles with an excitonogenic shell in hexagonal 2d-lattices. Qualitative agreement of these approaches is shown when calculating the field characteristics in arrays of cylindrical elements. Calculations are made of the characteristics of the near field of electronically excited molecules located above the surface of a regular quasi-two-dimensional lattice of spherical plasmonic nanoparticles.

Keywords: *luminescence of molecules, two-dimensional lattice, plasmon nanoparticle, plasmon resonance, nonradiative energy transfer*

Nanolattices or metallic photonic crystals are being investigated in detail at the present time due to the presence of a number of unusual properties in them, which make it possible to create new devices of modern optoelectronics [1-2]. These properties include: strong spatial and frequency dispersion, negative refraction, anisotropy, which manifest themselves in a wide spectral zone: from the microwave range to optical frequencies. Nanolattices are various periodically located metal elements or nanoobjects embedded in a dielectric matrix with a constant dielectric constant. It was shown that optical plasmons in nanowires can be used to transfer energy to quantum dots with subsequent emission of light quanta by the latter. Regular spatial structures composed of plasmonic nanoparticles of various geometries have unique optical characteristics, which suggests their use in promising nanophotonics, biosensorics, and other applications. In [3], the results of experimental and theoretical studies of samples of planar two-dimensional (2D) plasmon structures are presented. The samples under study were a 2D lattice of gold nanoparticles placed in a thin dielectric layer. The properties of such samples were studied using atomic force microscopy, as well as by optical methods. The absorption bands associated with the excitation of various surface plasmon resonances were interpreted. It was shown in [4] that the relationship between grating diffraction and localized surface plasmons in two-dimensional arrays of gold nanoparticles in water leads to narrow resonance peaks in the near infrared range, observed in far-field extinction spectra. It was shown in [5] that the emission of light by fluorescent molecules near periodic gratings-nanoantennas or plasmonic crystals can be strongly modified when the gratings are covered with a dielectric film. The connection between localized surface plasmon resonances and photonic states leads to the appearance of surface modes that increase the density of optical states and improve light output.

1. Regular gratings of long conducting nanorods (quasi-static approximation and rigorous approach)

The resulting field $E(\mathbf{r})$ in the lattice is the sum of the external field E_0 and the field of polarized rods [6], and the distribution of the strength $E(\mathbf{r})$ is reduced to the pattern in the plane (x, y) (Fig. 1). The vector P_2' of the dipole moment of a unit length of an individual nanowire of radius R has the form, where $P_2'(\omega) = \alpha_0(\omega)E_0$, $\alpha_0(\omega)$ is the polarizability of a unit length of

a nanowire at a frequency ω . In the case of a regular spatial arrangement of parallel nanorods in the form of a one-dimensional chain or two-dimensional lattice, the effective dipole moment per unit length of each rod can be represented as $\mathbf{P}_2(\omega) = \alpha_{eff}^{\perp} \mathbf{E}_0$, where α_{eff}^{\perp} is the effective polarizability

$$\alpha_{eff}^{\perp} = \left[\mathbf{I} - \alpha_0 \sum_i \sum_j \mathbf{G}(\mathbf{r}_{ij}) \right]^{-1} \alpha_0, \quad \mathbf{G}(\mathbf{r}) = \frac{1}{r^2} \left[2 \frac{\mathbf{r} \otimes \mathbf{r}}{r^2} - \mathbf{I} \right], \quad (1)$$

$\mathbf{r}_{ij} = \mathbf{r} + i\mathbf{e}_1 + j\mathbf{e}_2$ is radius vector of the rod with indices i and j , \mathbf{e}_1 and \mathbf{e}_2 - elementary vectors of a two-dimensional periodic lattice of nanorods. The field potential in such a lattice is determined by the expression

$$\varphi(\mathbf{r}) = -\mathbf{E}_0 \cdot \mathbf{r} + 2 \sum_i \sum_j \mathbf{P}_2(\omega) \mathbf{r}_{ij} / r_{ij}^2. \quad (2)$$

In quasi-two-dimensional geometry, calculations were performed for lattices with square $|\mathbf{e}_1| = |\mathbf{e}_2|$, $\angle(\mathbf{e}_1 \wedge \mathbf{e}_2) = \pi/2$ and hexagonal $|\mathbf{e}_1| = |\mathbf{e}_2|$, $\angle(\mathbf{e}_1 \wedge \mathbf{e}_2) = \pi/3$ packing of rods (Fig. 1), taking into account the influence of only a few nearest neighbors.

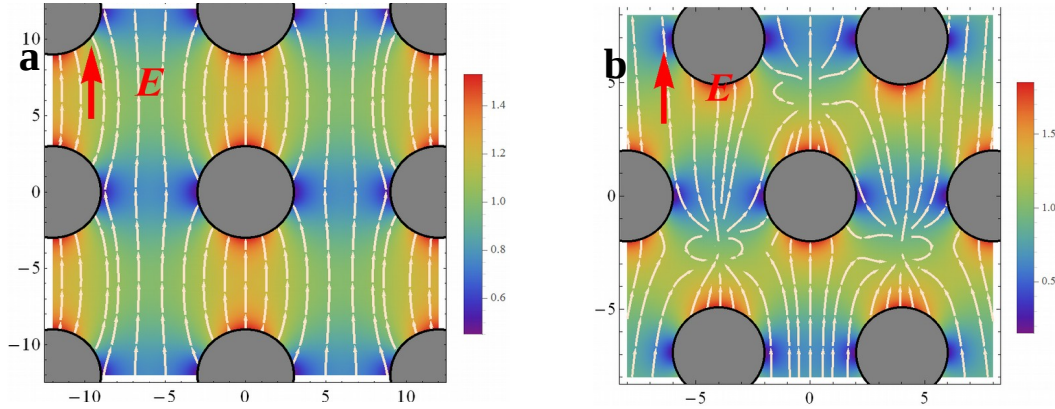


Fig. 1. Field structure $\mathbf{E}(\mathbf{r})$ and its relative amplitude $|\mathbf{E}(\mathbf{r})|/E_0$ in a quasi-two-dimensional matrix of infinite nanorods with their square (a) and hexagonal (b) packing

The maximum local field distortions occur when the vector \mathbf{E}_0 is oriented along the basis vectors \mathbf{e}_1 and \mathbf{e}_2 of the structure. Along the direction of the vector \mathbf{E}_0 parallel to the vector \mathbf{e}_1 of the lattice, the field energy density is concentrated near the nanorods, and in the transverse direction, the field maximum is located between them in the middle.

When calculating the probability \mathbf{P}_D of induced transitions for a molecule in a lattice of nanorods, it is necessary to take into account the orientation of its transition dipole moment, both with respect to the external field \mathbf{E}_0 and with respect to the principal axes of the quasi-two-dimensional structure. The case of coinciding orientation of vectors $\mathbf{P}_D \uparrow \uparrow \mathbf{E}_0$ is indicative, since with their angular mismatch the transition probability decreases. Alternatively, the spatial distribution of the electromagnetic field in periodic nanostructures composed of metal nanorods with activated plasmon modes was calculated by the FDTD method [6].

2. A grating of spherical conducting nanoparticles (quasi-static approximation)

In recent experiments [7], plasmon-accelerated Förster resonant energy transfer (FRET) in layered structures of organic dye molecules on the surface of silver island films was investigated. The effect of the plasmon subsystem on the fluorescence intensity of the dyes was observed, depending on the thickness of the insulating layer between the fluorophore and metal films. Here are the results of calculations of the characteristics of near-field fields formed in such nanostructures and determining the efficiency of nonradiative processes in them, as well as the spectra of the resulting fluorescence of a multilayer composite for its various geometries. The calculations were carried out on the basis of a special model, the prototype of which was the previously developed theory [8-9]. A plane nanolattice of hexagonal symmetry made of conducting nanoparticles was considered as a model of an island metal film. Taking into account the nearest dipoles in the lattice gives the following expression for the vector of the dipole moment $\mathbf{P}_2(\omega) = \alpha_{eff}^{\perp} \mathbf{E}_0$ of the nanoparticle selected in the center of the fragment, where

$$\alpha_{eff}^{\perp}(\omega) = \left[\mathbf{I} - \alpha_0(\omega) \sum_{j=1}^N \mathbf{G}(\mathbf{r}_j) \right]^{-1} \alpha_0(\omega), \quad \alpha_0(\omega) = R^3 \frac{\varepsilon_1(\omega) - \varepsilon_2}{\varepsilon_1(\omega) + 2\varepsilon_2}, \quad (3)$$

$\alpha_0(\omega)$ is the dipole polarizability of an individual nanoparticle of radius R ; Green's tensor $\mathbf{G}_j(\mathbf{r}) = r^{-3} (3\mathbf{n}\mathbf{n} - \mathbf{I})$ of the field of a dipole source; $\varepsilon_1(\omega)$, ε_2 - dielectric constants of the metal of the nanoparticle and the environment.

The potential of a quasi-static field from a dipole source with moment \mathbf{p} in space above such a grating is determined by the expression

$$\varphi(\mathbf{r}) = \frac{\mathbf{p}\mathbf{r}}{r^3} + \sum_j \alpha_{eff}^{\perp}(\omega) \frac{3(\mathbf{p}\mathbf{r}_j)\mathbf{r}_j - \mathbf{p}r_j^2}{r_j^5} \frac{(\mathbf{r} - \mathbf{r}_j)}{|\mathbf{r} - \mathbf{r}_j|^3}, \quad (4)$$

and the field strength at this point

$$\mathbf{E}(\mathbf{r}) = \frac{3(\mathbf{p}\mathbf{r})\mathbf{r} - \mathbf{p}r^2}{r^5} + \sum_j \frac{[3(\mathbf{p}_{eff}^{(j)}(\omega)(\mathbf{r} - \mathbf{r}_j))(\mathbf{r} - \mathbf{r}_j) - \mathbf{p}_{eff}^{(j)}(\omega)(\mathbf{r} - \mathbf{r}_j)^2]}{|\mathbf{r} - \mathbf{r}_j|^5}, \quad (5)$$

where $\mathbf{p}_{eff}^{(j)}(\omega) = \alpha_{eff}^{\perp}(\omega)[3(\mathbf{p}\mathbf{r}_j)\mathbf{r}_j - \mathbf{p}r_j^2]/r_j^5$ is the induced dipole moment at the j -th lattice element.

Plasmonic initiation of luminescence is carried out by increasing the rate of the radiative spontaneous transition $w_{sp}(z_D | \omega)$ in the nanostructure

$$w_{sp}(z_D | \omega) = \frac{4}{3} \frac{\omega^3}{\hbar c^3} \left| \mathbf{p} + \sum_j \mathbf{p}_{eff}^{(j)}(\omega) \right|^2. \quad (6)$$

The picture of the distribution of the near-field strength at different near-resonance frequencies in space outside the grating is shown in Figures 2 and 3. The structure of the resulting field in the plane at a frequency of 0.9, 1.02 and 1.15 of the plasmon resonance frequency ω_{res} of a spherical particle is shown. In all cases, localization of the field induced in the lattice is observed on the plasmon nanoparticle closest to the initiating dipole [10].

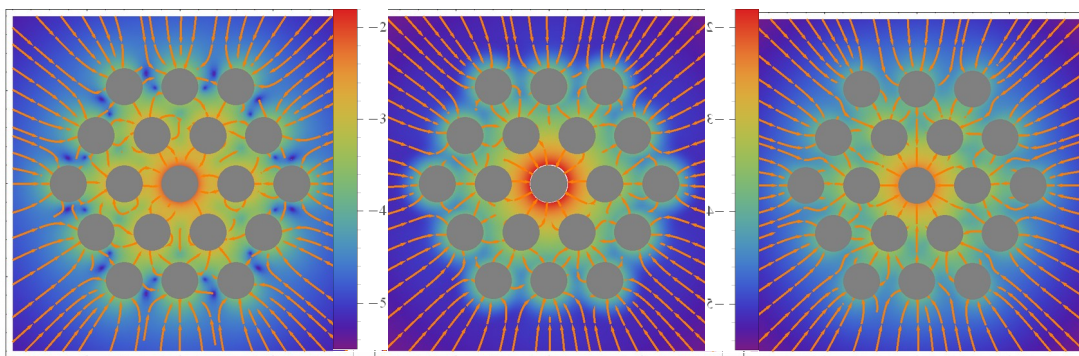


Fig. 2. The structure of the total field of the dipole and the plasmon grating in the X0Z plane at $Z = 0$ at frequencies 0.9, 1.02, and 1.15 of the plasmon resonance frequency. Orientation of the dipole along the OZ axis.

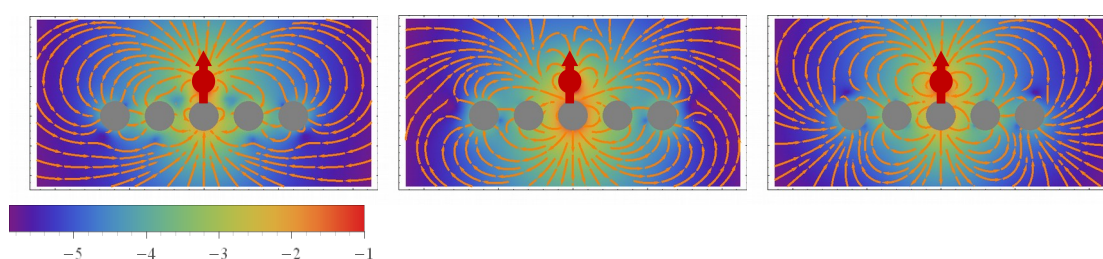


Fig. 3. The structure of the total field of the dipole and the plasmon grating in the X0Z plane at $Y = 0$ at frequencies 0.9, 1.02, and 1.15 of the plasmon resonance frequency. Orientation of the dipole along the OZ axis.

In contrast to the case of the X-orientation of the dipole, from Fig. 2 that in the plane of the grating near the plasmon resonance frequency, the field intensity near the central nanoparticle increases, and the structure of the field lines of the field practically does not change. In this case, in the X0Z plane (Fig. 3), at frequencies lower than the plasmon resonance frequency, the layer of metal nanoparticles "reflects" the field from itself, and at frequencies higher than the plasmon one, the field amplitude above the nanoparticle layer increases. Near plasmon resonance, the field is concentrated between the dipole and the lattice of nanoparticles, and above the layer of dipole molecules (in the region where acceptor molecules are located) the field is weakened. In fig. 4 shows the frequency dependence of the relative rate of spontaneous transitions over the lattice at a distance: 1 - $2.5R$, 2 - $3R$, where $R=10$ nm is the radius of nanoparticles.

Calculations based on model (3) - (6) showed that the structure of the field formed by the system has a pronounced dependence on the orientation of the dipole moment of the donor molecule relative to the layer plane (Fig. 5). In the "molecule-lattice" system, the maximum of the curve - plasmon resonance - shifts towards lower frequencies in the case of the longitudinal orientation of the dipole, and towards higher frequencies - in the transverse orientation, as compared with the case of the near-field intensity spectrum of the two-particle system "dipole-nanosphere". Fig. 5 that the frequency dependence of the rate of spontaneous transitions of the "donor molecule-plasmonicnanolattice" system shifts depending on the orientation of the dipole moment \mathbf{p}_D of the donor molecule. Thus, when the vector \mathbf{p}_D is oriented in the lattice plane (XOY), the maximum of the dependence shifts below the plasmon resonance frequency for a solitary nanosphere, and when the vector \mathbf{p}_D is oriented along the Z axis, a shift in the opposite direction occurs.

The research was carried out with the financial support of the Ministry of Science and Higher Education of the Russian Federation within the framework of scientific project No. FSGU-2020-0003.

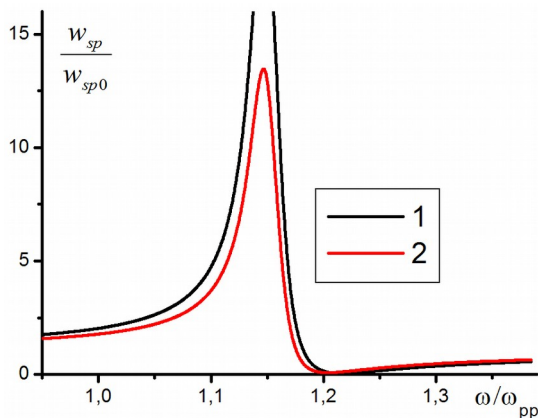


Fig.4. Frequency dependence of the rate

$$w_{sp}(z_D | \omega) / w_{sp0}(\omega) = |\mathbf{p}_{eff}|^2 / |\mathbf{p}_D|^2$$

of spontaneous transitions in a donor molecule near the plasmon lattice at a distance of 1 - 2.5R, 2 - 3R, referred to the rate of spontaneous transitions in a solitary molecule. $R = 10$ nm is the radius of nanoparticles. Orientation of the dipole along the OZ axis. ω_{pp} is the plasmon frequency for one lattice element.

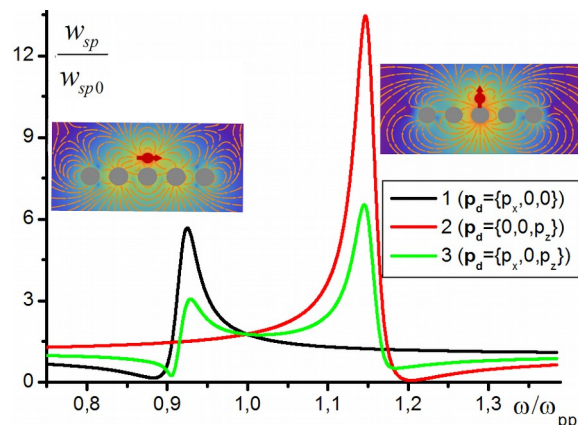


Fig. 5. Frequency dependence of the rate

$$w_{sp}(z_D | \omega) / w_{sp0}(\omega) = |\mathbf{p}_{eff}|^2 / |\mathbf{p}_D|^2$$

of spontaneous transitions in a donor molecule in the presence of a plasmon lattice at a distance of 2.5R, referred to the rate of spontaneous transitions in a solitary molecule. $R = 10$ nm is the radius of nanoparticles. ω_{pp} is the plasmon frequency for one lattice element. 1- Orientation of the dipole along the OX axis; 2-along the OZ axis; 3 - Orientation of the dipole in the XOZ plane.

List of references

1. Silveirinha M.G., Fernandes C.A., Costa J.R. // *Phys. Rev. B.* 2008. Vol. 78. P. 195 121(1–7)
2. Davidovich M.V., Shilovskii P.A. *Technical Physics. The Russian Journal of Applied Physics.* 2012. T. 57. № 12. C. 1687-1691.
3. Shaymanov A., Khabarov K., Merzlikin A.M., Bykov I. V., Baryshev A.V. // *J. Experim. and Theor. Physics* 124(4):584-591. DOI: [10.1134/S1063776117030165](https://doi.org/10.1134/S1063776117030165)
4. Chu Yizhuo, Schonbrun Ethan, Yang Tian, Croziera K.B. // *Applied Physics Letters* 2008. V. 93, P. 181108
5. Vecchi G., Giannini V., Gómez Rivas J. // *Phys. Rev. Lett.* 2009. V. 102. P. 146807
6. Kucherenko M.G., Rusinov A.P., Kislov D.A. *VII Internat. Confer. on Photonics and Information Optics, (2018)* 173-189.
7. Ibrayev N., Seliverstova E., Zhumabay N., Temirbayeva D. // *J. Lumin.,* V. 214 (2019). P. 116594.
8. Kucherenko M.G., Rusinov A.P. // *Univer. complex as a region. center science and cult. Mater. All-Russian scient. confer. Orenburg, 2015.* P. 1091-1096.
9. Kucherenko M.G., Rusinov A.P., Nalbandyan V.M. // *Int. scient. conf. "Science and educ.", 60 years of OSU. 2015 Part 4.* - P. 167-173.
10. Kucherenko M.G., Rusinov A.P., Ibraev N.Kh., Seliverstova E.V. *11th Intern. Confer. «Chaos and structures in nonlinear systems» 2019, Kazakhstan, Karaganda.* P. 128-133.

3A1b Microwave activation of phyllosilicate adsorption on kaolin clays

Alpysbaeva G., Kanygina Olga, Chetverikova Anna, Chetverikova Dariya
Orenburg State University, Orenburg, Russian Federation

Ability to activate adsorption capacity of dispersed systems of naturally-occurring aluminosilicates via microwave activation was studied. Dispersed particles of kaolin clay with low adsorption characteristics were studied. Methylene blue was used as the adsorbent as its amount is well controlled over a white background of particles. Powders were subjected to a 10-minute long microwave treatment at a power of 800 W with a frequency of 2.45 GHz. It was found that microwave activation of dye extraction occurs without any change in adsorption mechanisms, so it is due to structural transformations taking place within the particles.

Keywords: adsorption, microwave activation, kaolin clay

Introduction. Analysis of the current state of research of physical chemistry of aluminosilicates shows that with a vast amount of information some aspects of structural transformations caused by external factors are clearly insufficiently studied. With the current state of affairs a modern approach is required to natural clays together with new methods of their research and development of new technologies.

Currently, mineral adsorbents are of great interest, since the production of synthetic adsorbents is expensive. From this point of view, natural complex aluminosilicates are an interesting research object. Phyllosilicates occupy a special place in fundamental studies of adsorption. The search for sorbents that are most effective for green production in terms of protecting the environment from pollution involves the usage of such natural raw material [1].

The easiest way to estimate the adsorbency of a clay is to use dyes as an adsorbate. The efficiency of adsorption is determined by three factors: by the surface tension at the phase boundary, by the interaction forces between the dye and the adsorbent, and by the porosity of the adsorbent [2]. The strength of a bond between the dye and the adsorbent is defined by the type of forces manifested during adsorption.

According to present view, the sorption features of kaolin clays are low and the sorption properties of clays from the Orenburg deposits have not yet been studied. The activation of clays via microwave treatment makes it possible to create additional adsorption centers. This should result in an increase of the exchange capacity of clays [3]. Microwave activation is an environment friendly, fast-acting, and energy-efficient process that allows one to perform a local influence on the surface of clay mineral particles [4].

The goal of the work was to perform the following tasks. 1) To study an opportunity to increase the adsorption capacity of phyllosilicate particles in samples of natural kaolin clay via microwave field treatment. 2) To estimate changes in the sorption capacity using Langmuir isotherms and the mechanism of interaction of functional groups of the dye with a surface of clay mineral particles.

Material and methodology. The object of the study was raw kaolin mineral materials from the Svetlinsky district of the Orenburg region. We selected kaolin clay powders consisting of fragmented particles with an effective diameter less than 40 μm . The whiteness factor of powder samples, determined according to [5], is above 90%.

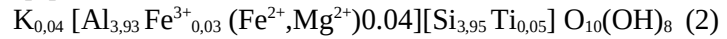
Among all structure-forming minerals kaolinite has the lowest sorption capacity, which varies from 3 to 15 milligram-equivalent per 100 g. This is due to the rigid crystal structure of the mineral and the almost complete absence of isomorphic substitutions. Exchange processes in kaolinite take place on the side cleavages of particles and they are caused by the presence of uncompensated valence bonds. The structure of this phyllosilicate can be imagined as two layers: an oxygen tetrahedral layer with a silicon cation in the center and an oxygen-hydroxyl

octahedral layer with an aluminum cation in the center [6]. The connection between the layers is carried out by molecular and hydrogen forces the energy of which exceeds the energy of hydration of the interlayer space. Minerals of this group do not exhibit intracrystallineswelling. The layer alternation period is about 0.7 nm; the thickness of the silicon-oxygen layer is 0.49 nm. On the basal surface formed by “inverted” tetrahedra with a vertex distance of 0.25 nm oxygen atoms form a hexagonal network [1].

The structural formula of pure kaolinite reads:



For the majority of kaolinite isomorphous substitutions was found: it was established that iron and magnesium atoms are found among octahedral cations, while an insignificant number of titanium atoms may be included in the tetrahedra. Therefore, the averaged structural formula of kaolinite takes the following form [6]:



By the way of the octahedral layer filling kaolinite belongs to dioctahedral minerals, to phyllosilicates of the 1:1 type. Both layers form a package in which the hydroxyl groups are located on one side. Unlike iron, which directly enters the crystal lattice of clays (hard frame), copper is placed in the interlayer hydration space. With one-layer hydration Cu^{2+} cation forms a hydration complex of 4 water molecules. A two-layer hydration layer forms $[\text{Cu}(\text{H}_2\text{O})_6]^{2+}$. A three-layer interlay is formed due to the same complex, but with a different orientation of water molecules. The presence of iron and copper oxides increases the water wetting heat of clays. The affinity of the surface of clay particles for water is greater in the presence of copper oxide than in the presence of iron oxide [7].

Two methods were chosen to determine the quantitative content of iron and copper oxides in the clays. Those methods are the photocolometric method of silicate materials absorption spectroscopy and the method of ion-exchange chromatography for separation of iron (III) and copper (II) ions in their mixture. To study the microwave adsorption activation we used the spectrophotometric method. The method is based on a control the solution's optical density before and after dyes interact with the surface of crystals of clay minerals. Optical density was measured with KFK-3 photocolimeter.

The sorption of dyes on different types of minerals defined by the structure of material particles and by the dye itself. Methylene blue is a universal dye. It has the richest spectrum of test characteristics and it is widely used as a test-sorbate in various studies of minerals sorption capacity [8, 9]. The methylene blue molecule has a large size about 1.5 nm.

The sorption capacity was evaluated by the change in the optical density before and after the sorption. The degree of sorbate extraction W was calculated by the following formula:

$$W = \frac{(C_{init} - C_{fin})}{C_{init}} \times 100 \%, \quad (3)$$

where C_{init} , C_{fin} are molar concentration of the dye in the solution before and after sorption respectively. After the experiment the maximum ion-exchange capacity for methylene blue and the sorption mechanism were determined from the sorption isotherms.

Natural clay powders (A0) were treated with 800 W microwave field with frequency of 2.45 GHz for 10 minutes (sample A1). Infrared spectroscopy was used to control structural transformations [10]. Changes in chemical bonds of the clays were found by the IR spectra of the samples obtained before and after the exposure. The samples were formed into KBr tablets and their spectra were recorded with Bruker Alpha FT-IR spectrometer. This spectrometer is designed to measure optical transmission and reflection spectra in the mid-IR range of 4000–400 cm^{-1} .

The phase composition was found by X-ray phase analysis on an MD10 mini-diffractometer in monochromatic copper radiation in the angle range from 20 ° to 120 ° on the 2θ scale. Results were recorded in a digital format. X-ray reflection were qualitatively interpreted by the standards contained in the PDF02 database (ICDD, 2006) of the LookPDF software.

Results. Results of the chemical silicate analysis show that kaolin clay had the chemical composition given in Table 1.

Table 1. Chemical composition of kaolin clay (wt pct)

SiO ₂	CaO	MgO	Fe ₂ O ₃	Al ₂ O ₃	TiO ₂	CuO	MnO	ZnO	Σ(Na ₂ O+K ₂ O)	LOI	Σ
53,50	2,14	0,97	1,63	21,89	1,97	0,27	0,02	0,06	4,45	10,10	100

Microwave irradiation of dispersed systems consisting of kaolin clay particles resulted in structural transformations at several structural levels:

- the effective particle diameters were decreased by an average of 1.2 times, which led to a corresponding increase in the specific surface area;
- the whiteness factor of the powder increased from 90 to 93% due to the growth of the kaolinite particles surface;

X-ray diffraction shown that the volume fraction of crystalline kaolinite decreased from 74% to 62% due to the amorphization of kaolinite particles and due to a slight increase in the tridymite content (from 13 to 16%). SiO₂ particles underwent polymorphic transformations with a general decrease of the symmetry of the newly formed crystalline phases. Microwave treatment also caused a decrease of the size of α-Al₂O₃ particles coherent scattering region of X-ray radiation [11].

The initial sample was dominated by bonds of the type $\nu_{as}(\text{Si-O-Si})_{\text{bridge}}$ or $\nu(\text{Si-O-Al})$ and by bonds $\delta(\text{Si-O})$ in the SiO₄ tetrahedron. The infrared spectra of K-clay, as in [12], contained characteristic absorption bands given in cm⁻¹: 3620, 3424, 1032, 1008, and 912. Microwave treatment resulted in a rapid destruction of the most fragile Si-O-Si bridging bonds: their share amount decreased about the factor 1.8–2. A significant part of the dominant bonds in the SiO₄ tetrahedron, similarly to the $\delta(\text{Al-O-H})$ bond, was destroyed. Spectra of all samples contain the C – C band (at 467 cm⁻¹). The vibration mode was not altered by the microwave treatment, but its intensity decreased. This could be a response either to the limitation of the angular deformations of the C – C bond which is due to a retaining of the carbon between the plates of clay minerals, or to its extraction (burning out) from the clay bulk. Consequently, the particles of kaolin clay turned out to be sensitive to the conditions of microwave treatment [10]. These structural transformations resulted in an increase of the adsorption capacity of kaolin clay. Figure 1 shows the time dependencies of the degree of extraction of methylene blue powder in the initial state (A0) and after the exposure (A1).

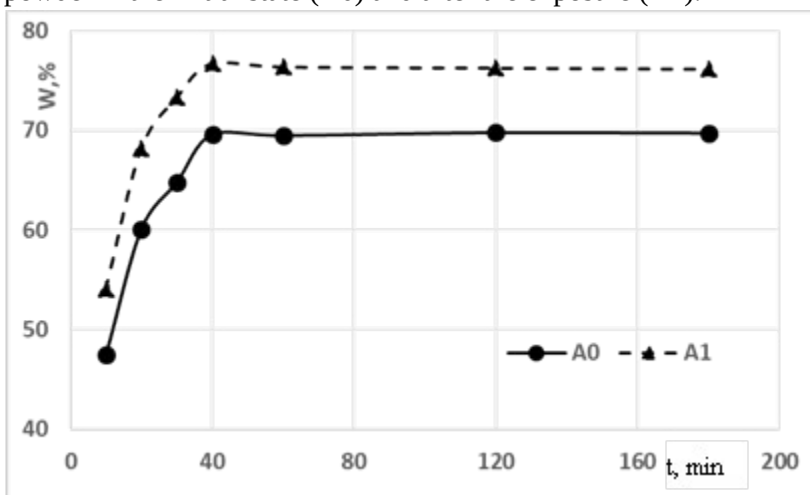


Figure 1. Dependencies of the degree of extraction of methylene blue by samples A0 and A1 on the time of adsorption

The maximum of methylene blue extraction after the microwave treatment increased slightly, by the factor 1.1. The active sorption mode was observed in both cases in the first 40 minutes. The extraction rates of methylene blue by samples A0 and A1 were (in % per min): 1.74 and 1.92, respectively. These values were proportional to the specific surface area.

The value of the sorption capacity for the methylene blue dye was determined via Langmuir isotherms and it increased by 37% from 1.77 mg / g to 2.84 mg / g, which is also due both to an increase of the particles specific surface area and to the amorphization.

Based on the results obtained, it was concluded that the increase of the kaolin clay particles adsorption features is due to the structural transformations at the level of chemical bonds and at the level of morphology. The sorption of the dye by clay particles was predominantly monomolecular; the interaction between the functional groups of the dye and the surface of the clay mineral particles proceeded by the donor-acceptor mechanism.

REFERENCES

1. Ivanova Ye. S. Vzaimosvyaz' strukturnykh isorbtsionnykh svoystv prirodnikh al'yumosilikatov: dis. kand. khim. nauk. 02.00.01 :zashchishchena 26.02.15 : utv. 07.04.15 / Ye. S. Ivanova. - Sankt-Peterburg, 2015. – 110 s. – Bibliogr.: s 1-106. – 415040760017.
2. Parfitt G. D., Rochester C. H. Adsorption from solution at the solid/liquid interface, Academic Press, 1983, 416 p.
3. Preparation, Adsorption Properties and Microwave-Assisted Regeneration of Porous C/SiC Ceramics with a Hierarchical Structure / Cuiyan L., Zhao X., Haibo O., Liyuan C., Jianfeng H., Yijun L. // Applied Composite Materials. 2020. V. 27. No. 3. P. 131-148.
4. Kazmierczak-Razna J., Pietrzak R. The Use of Microwave Radiation for Obtaining Carbonaceous Adsorbents from Biomass and Their Use in Elimination of Inorganic Pollutions // Adsorption. 2016. V. 22. No. 4-6. P. 473-480.
5. ISO 26066–83. Processed kaolin. Method of brightness measurement, 1984. 5p.
6. Osipov V.I., Sokolov V.N. Clays and their properties. Composition, structure and formation of properties - Moscow: GEOS. 2013. 576 p.
7. Kanygina O.N., Chetverikova A.G., Strelkovskaya A.D. Molecular Interaction at Water Purification by Clay Containing Montmorillonite // Russian-Japanese Conference "Chemical Physics of Molecules and Polyfunctional Materials": Proceedings. 29-31 October 2014. P. 66-68.
8. Vedeneeva, N. Ye. Method of research of clay minerals using dyes / NE Vedeneeva, MF Vikulova. - Lviv: Publishing house of the Lviv state. University, 1956. 95 p.
9. Andreeva K.D. The Technique for the Operational Determination of the Cation Volume of Clays // Proceedings of higher educational institutions. Geology and exploration. 2014. No. 6. P. 74-76.
10. Chetverikova, A. G., Kanygina, O. N., Alpysbaeva, G. Z., Yudin, A. A., & Sokabayeva, S. S. Infrared Spectroscopy as the Method for Determining Structural Responses of Natural Clays to Microwave Exposure. *Kondensirovannyye Sredy I Mezhfaznye Granitsy = Condensed Matter and Interphases*, 2019, V. 21, No. 3, P. 446-454. DOI: <https://doi.org/10.17308/kcmf.2019.21/1155>
11. Chetverikova A. G., Kanygina O. N., Filyak M.M. Structural Responses in Oxides of Aluminum and Silicon in Microwaves Fields // *Materialvedenie*, 2020, No 5. P. 37-42. DOI: [10.31044/1684-579X-2020-0-5-37-42](https://doi.org/10.31044/1684-579X-2020-0-5-37-42)
12. Characterization of bentonite clays from Cubati, Paraíba (Northeast of Brazil) / De Oliveira C. I. R., Rocha M. C. G., Da Silva A. L. N., Bertolino L. C. // *Ceramica*, 2016, v. 62(363), pp. 272–277. DOI: 10.1590/0366-69132016623631970

3A2b Morphology and biological activity of Co and Zn oxide nanoparticles and ferrates

Nikiyan Hike, Davydova Olga, Senatorova D.
 Orenburg University, Russia,
nikiyan@yahoo.com

Nanoparticles of Co and Zn oxides, as well as their ferrates were studied under various synthesis conditions (weakly acidic and alkaline) for morphology and biological activity against Escherichia coli and Staphilicoccus aureus cells. The estimated size (30 to 400 nm) and shape (spherical or round) can cause different bactericidal effects. The dose-dependent (on time and concentration) antibacterial effect is different for gram-positive and gram-negative microorganisms, it is associated with the conditions of nanoparticles synthesis, the type of compound and metal.

Nanoparticles, atomic force microscopy, bactericidal effect, antibacterial effect, biological activity.

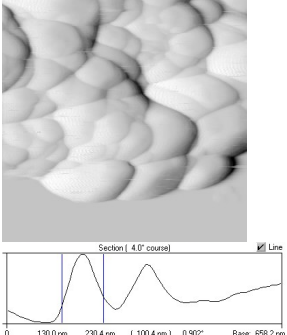
Among numerous nanomaterials, MFe_2O_4 nanopreparations (M – Mg, Zn, Ni, Co, Cd, etc.) that belong to spinel-type magnetic products are relevant in biomedical practice, used in drug delivery as biosensors for magnetic resonance imaging and magnetic hyperthermia [1]. At present, special attention is paid to the study of the morphology and biological activity of such nanoparticles (NPs).

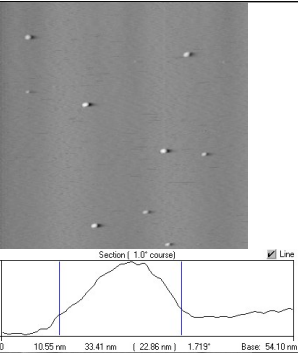
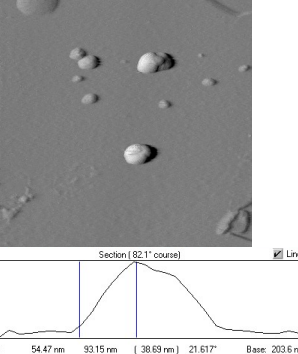
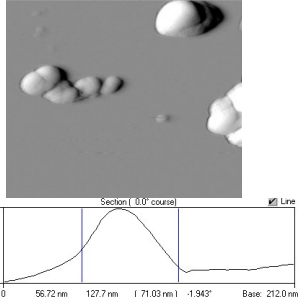
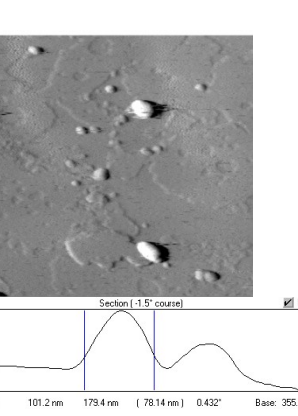
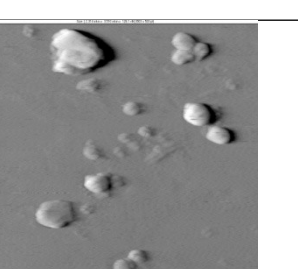
In this regard, the work evaluated the dimensional and cytotoxic properties of NPs of oxides and ferrites of Co and Zn biosynthesized at various pH levels in an aqueous extract of *Petroselinum crispum* leaves [2]. Biological (or “green”) synthesis of nanoparticles using plant extracts is an attractive alternative to traditional chemical synthesis [3].

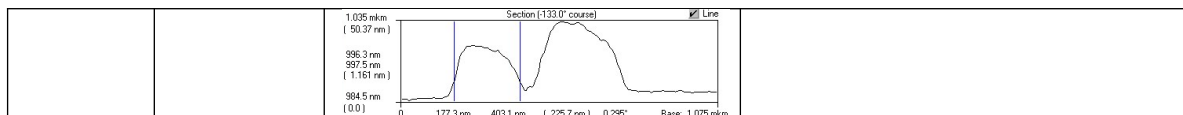
The shape and size of NPs were visualized using the contact mode of an atomic force microscope (SMM-2000; Proton-MIET, Russia). The antibacterial activity of biogenic NPs against gram-negative (*E. coli*) and gram-positive (*S. aureus*) strains was studied under conditions of acute (1 hour) and chronic (24 hours) toxicity at various concentrations (0.5 and 5 mg/ml).

Atomic force microscopy (AFM) of the studied NPs is presented in Table. 1.

Table 1 - AFM NPs

NP	Synthesis conditions	AFM image, 2x3 mkm, surface profile	Characteristics
ZnO	neutral		heterogeneous in size: small - 55-100 nm, medium - from 120 to 200 nm, large 300-400 nm, there are conglomerates on the scans

ZnFe ₂ O ₄	weakly acidic		Spherical, uniform in size - from 20 to 70 nm
	alkaline		relatively uniform in size: from 60 to 90 nm for small and from 140 to 160 nm for large. There are conglomerates ranging in size from 250 nm and above
Co ₃ O ₄	neutral		relatively uniform in size: small 30-90 nm, large 160-220 nm
CoFe ₂ O ₄	weakly acidic		the composition of the sample is heterogeneous: small spherical formations from 60 to 90 nm, large objects with a diameter of 120-150 nm and huge aggregates. Some particles are doubled.
	alkaline		The composition of the sample is inhomogeneous: small 70-90 nm, doubled at 36-55 nm, also medium 130-190 nm, and large non-spherical, from 300 nm in size.



AFM made it possible to detect predominantly round-shaped particles of Zn and Co oxides, Zn ferrates and often “doubled” particles for Co ferrates. In this case, the samples, in addition to ZnFe₂O₄ (weakly acidic), had a heterogeneous composition from 30 to 400 nm, sticking together into larger aggregates (~ 1 μm).

The antibacterial activity of the studied NPs is presented in Table 2.

Table 2 - Bactericidal effect of NPs on *E. coli* / *S. aureus* (in% relative to the initial number of cells)

NP	Synthesis conditions	Concentration, mg/ml	CFU after n hours,%	
			1	24
ZnO	-	0,5	67 / 100	100 / 100
		5	86 / 100	100 / 100
ZnFe ₂ O ₄	weakly acidic	0,5	0 / 0	0 / 0
		5	0 / 0	0 / 0
	alkaline	0,5	70 / 86	87 / 100
		5	79 / 92	100 / 100
Co ₃ O ₄	-	0,5	15 / 21	35 / 74
		5	20 / 27	47 / 91
CoFe ₂ O ₄	weakly acidic	0,5	0 / 0	0 / 26
		5	0 / 10	0 / 45
	alkaline	0,5	0 / 0	0 / 0
		5	0 / 0	9 / 0

The data obtained indicate that samples with Zn exhibit a more pronounced bactericidal effect than with Co, while NPs with Zn synthesized under alkaline conditions are more toxic than under weakly acidic conditions, and with Co, vice versa. The acute toxic effect (after 1 hour of contact) increases in a day by 1.2-4.5 times, and an increase in concentration by 10 times (from 0.5 to 5 mg / ml) leads to an increase in bactericidal activity by an average of 30%.

The antibacterial activity of NPs can probably be associated with both the shape of the particles (particles with a rough surface and sharp edges cause mechanical damage to the cell walls) and the conditions of their synthesis [4]. In addition, to assess the toxicity of NPs, it is necessary to determine the percentage size groups in each sample: a large number of small nanoparticles (<100 nm) increases their activity compared to coarse particles due to an increase in sorption capacity, which cannot be ignored in the case of future biological applications of these materials [5].

Thus, the results obtained in our study are promising and require further testing, including using other biological models.

References:

1. Mohapatra J, Xing M. and Liu J.P. Inductive Thermal Effect of Ferrite Magnetic Nanoparticles // *Materials*. 2019, 12, P. 3208-3238.
2. Korotkova A.M., Polivanova O.B., Gavrish I.A., Kosyan D.B., Bagrov D.V., Klinov D.V., Fenin A.A., Koroleva M.Y., Baranova E.N., Ksenofontov D.A., Cherednichenko M.Y., Lebedev S.V. «Green» Synthesis of Cerium Oxide Particles in Water Extracts *Petroselinum crispum* // *Current Nanomaterials*. 2019, 4(3), P. 176-190.

3. Mittal A.K., Chisti Y. and Banerjee U.C. Synthesis of metallic nanoparticles using plants // *Biotechnol.* 2013, 31, P. 346–356.
4. Korotkova A., Lebedev S. and Gavrish I. The study of mechanisms of biological activity of copper oxide nanoparticle CuO in the test for seedling roots of *Triticum vulgare* // *Environ. Sci. Pollut. Res.* 2017, 24(11), P. 10220–10233.
5. Hoet P., Bruske-Hohlfeld I., Salata O. Nanoparticles – known and unknown health risks // *Journal of Nanobiotechnology.* 2004, 2 (12).

3A3b Rate coefficients and branching ratio for quenching of $O(2p^3 3p^3 P_J)$ by collisions with He

Yuki Tanimoto,¹ Takumi Daijogon,¹ Shogo Tendo,¹ Hiroshi Kohguchi,² Katsuyoshi Yamasaki²

¹Graduate School of Science, Hiroshima University

²Graduate School of Advanced Science and Engineering, Hiroshima University

Atomic oxygen plays important roles in the chemical reactions in the atmosphere, combustion, and plasma. In this study, we have determined the branching ratio for quenching of the $2p^3 3p^3 P_J \rightarrow 2p^3 3s^3 S$ by collisions with He.

Fig. 1 shows the energy diagram of atomic oxygen. k_{q1} and k_{q2} are the rate coefficients for quenching from the $2p^3 3p^3 P_J$ state to the $2p^3 3s^3 S$ state and other states, respectively.

A gaseous mixture of O_3 (6–13 mTorr) and He (4.8–400 Torr) in a flow cell at 298 K was irradiated with laser light at 248 nm. $O(2p^4 3P_J)$ was generated in the $O(2p^4 1D) + O_3$ reaction. $O(2p^4 3P_2)$ was excited to $O(2p^3 3p^3 P_J)$ with two photons at 226 nm. The $2p^3 3p^3 P_J$ state transfers to the $2p^3 3s^3 S$ state via infrared transition ($= k_{IR}$) or collisions with ambient gases. The $2p^3 3s^3 S$ state emits vacuum ultraviolet fluorescence via the transition to the $2p^4 3P_J$ state.

The time-resolved fluorescence from the $2p^3 3s^3 S$ state were recorded at varying pressures of He (Fig. 2). The profiles of the fluorescence from the $2p^3 3p^3 P_J$ state are nearly identical to those from the $2p^3 3s^3 S$ state since the radiative lifetime of $O(2p^3 3s^3 S)$ (≈ 2 ns) is much shorter than the decay of $O(2p^3 3p^3 P_J)$ under the present experimental conditions.

On the basis of the values of the lifetime of the infrared transition ($1/k_{IR}$) and the overall quenching rate of the $2p^3 3p^3 P_J$ state ($k_{q1} + k_{q2}$) the ratio (slope)/(intercept) = k_{q1}/k_{IR} of the plot shown in Fig. 3 has given the state-specific quenching rate coefficient $k_{q1} = 3.5 \times 10^{-13} \text{ cm}^3 \text{ molecule}^{-1} \text{ s}^{-1}$ and the branching ratio $k_{q1}/(k_{q1} + k_{q2})$ to be 15 %.

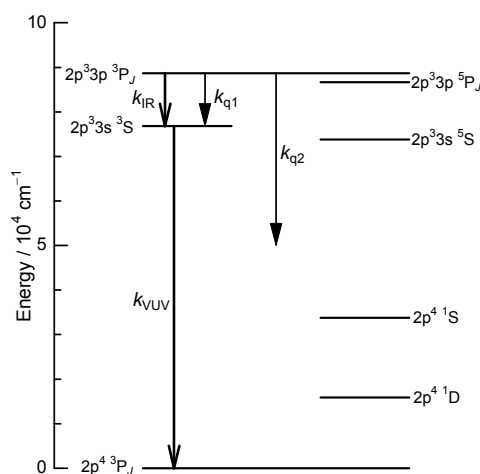


Fig. 1. Energy diagram of atomic oxygen.

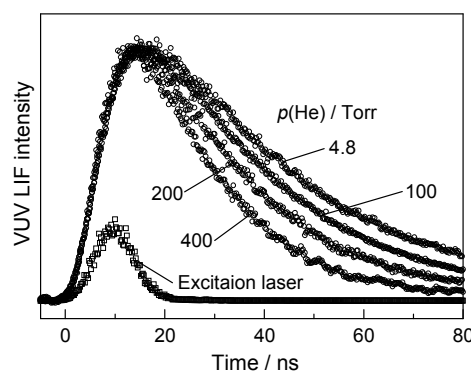


Fig. 2. Time-resolved fluorescence from $O(2p^3 3s^3 S)$ at varying pressures of He.

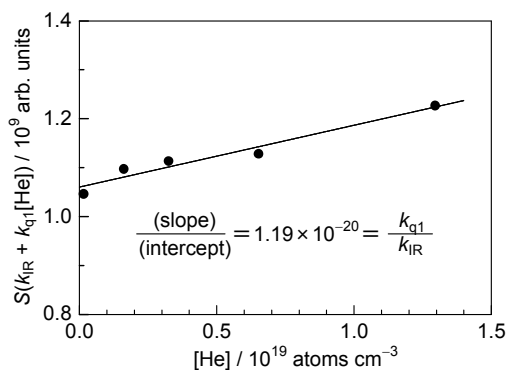


Fig. 3. Plot of $S(k_{IR} + k_{q1}[\text{He}])$ versus $[\text{He}]$. S corresponds to the area of the fluorescence shown in Fig. 2.

Letuta Ulyana G.

Orenburg University, Orenburg, Russia

E-mail: shevulyana@yandex.ru

*Experimental evidence for the theory of enzymatic magneto sensitivity is considered in this paper on the example of *E. coli* bacteria. Combined effects of an external static magnetic field and magnetic isotopes of zinc and magnesium on the metabolism of *E. coli* bacteria have been studied. The magnetic isotope of magnesium stimulates bacterial growth and affects antibiotic resistance and biofilm formation. The external magnetic field of 76-93 mT enhances the effect of the magnetic magnesium isotope ^{25}Mg , increasing the colony-forming ability. Similar effects have been found in the range of 25-30 mT for magnetic zinc isotope ^{67}Zn . The combined effect of magnetic field of 70-95 mT and the magnetic magnesium isotope ^{25}Mg on *E. coli* also leads to a significant increase in the intracellular concentration of ATP. This proves the sensitivity of enzymatic reactions to the magnetic field.*

Keywords: magnetic field, magnetic isotope, magnesium, zinc, bacterial metabolism

Magnetic sensitivity of living organisms is an intriguing scientific problem. There are many works that investigate causes of its occurrence, mechanisms, and consequences of various magnetic fields effects on living cells. Even though such work has been carried out for more than a decade, a clear answer about the mechanism of influence of magnetic fields on organisms has not been found. The discoveries of the 21st century in the magnetic isotopy have been proved that cells react not only to external magnetic fields, but also to fields created by magnetic nuclei of chemical elements isotopes inside cells [1-4]. For example, the magnetic isotopes of magnesium ^{25}Mg , calcium ^{43}Ca , and zinc ^{67}Zn , being in the active site of phosphorylating enzymes, contribute to an increase the ATP yield [1-4]. The presence of the same magnetic isotopes in the active site of DNA polymerase suppresses DNA synthesis [2-4]. The enzymatic reaction with electron transfer was considered as the primary receiver of the magnetic field in the magnetic sensitivity theory of living organisms proposed in [5]. As a result of this reaction, an ion-radical pair is formed, the spin state of which, as well as the further course of the reaction, depend on magnetic nuclei presence or external magnetic fields exposure. In this paper, we consider experimental evidence for the theory of enzymatic magneto sensitivity on the example of *E. coli* bacteria.

Bacteria *E. coli*, strain K12TG1, were cultured in a synthetic nutrient medium, in which magnesium (or zinc) sulfate was replaced with an isotopic analog. Among the used stable isotopes of magnesium $^{24,25,26}\text{Mg}$, only ^{25}Mg is magnetic. Among the isotopes of zinc $^{64,66,67}\text{Zn}$, ^{67}Zn is magnetic. A special experimental setup was created to study the external magnetic fields effects. Bacteria were exposure by static magnetic field in the range of 0.8-98 mT during growth. The magnetic field was created by an electromagnet from Takeda Riken Ltd. The magnetic isotope magnesium ^{25}Mg have been found affected the growth and physiological properties of *E. coli* bacteria (antibiotic resistance and biofilm formation. Its biological effects differ from those of non-magnetic isotopes of $^{24,26}\text{Mg}$. The colony-forming ability of *E. coli* bacteria growing on a medium with magnetic magnesium isotope is higher in the range of 0-15 and 76-93 mT. The intracellular elemental composition changes because of the combined action of external static magnetic field and the magnetic isotopes of magnesium ^{25}Mg and ^{67}Zn . The intracellular content of ATP in *Escherichia coli* bacteria is a magnetically dependent indicator of the vital microorganism activity. The magnetic field of 70-95 mT and magnetic isotope of magnesium ^{25}Mg effects on *E. coli* leads to a significant increase in the intracellular concentration of ATP. The observed effects indicate that the magnetic moments of atomic nuclei of the ^{25}Mg and ^{67}Zn isotopes affect the entire body through several intracellular

enzymatic processes, including ATP synthesis. The effects of the magnetic field in the range of 0.8-16 mT, registered for all bacteria without considering the magnesium or zinc isotope enrichment of cultured medium, indicate the sensitivity of intracellular processes to weak magnetic fields.

This work was financially supported by the Ministry of Science and Higher Education of the Russian Federation, project no. FSGU-2020-0003.

1. Buchachenko A.L (2009) *Magnetic Isotope Effect in Chemistry and Biochemistry*. Nova Science Publishers, New York.
2. Buchachenko A.L (2014) *Magneto-Biology and Medicine*. Nova Science Publishers, New York
3. Buchachenko A.L (2014) Magnetic field-dependent molecular and chemical processes in biochemistry, genetics and medicine. *Russ Chem Rev* 83:1–12
4. Buchachenko A.L, Bukhvostov A.A, Ermakov K.V, Kuznetsov D.A (2020) A specific role of magnetic isotopes in biological and ecological systems. *Physics and biophysics beyond. Prog Biophys Mol Biol* 155:1-19
5. Letuta U.G, Berdinskiy V.L, Udagawa C, Tanimoto Y (2017) Enzymatic mechanisms of biological magnetic sensitivity. *Bioelectromagnetics* 38(7):511-521.

3A5b

Transition Metal-Free Borylation Reaction Using 1,8-Diaminonaphthalene-substituted Borane [H–B(dan)] as a B(dan) Electrophile

Jialun Li,¹ Shintaro Kamio,¹ Hiroto Yoshida¹

¹ Graduate School of Advanced Science and Engineering, Hiroshima University

Lewis acidity of organoboron compounds having a 1,8-diaminonaphthalene substituent on the boron center, R–B(dan), is highly diminished, owing to the effective electron-donation from the adjacent nitrogen atoms and the nearly ideal B(sp²)-hybridized orbital arising from the planar six-membered ring structure (Figure 1). We have recently reported that the “protected” B(dan) moiety can be readily activated by *t*BuOK to generate the respective borate species, which serves as a key intermediate in the actual direct Suzuki–Miyaura coupling (SMC) with Ar–B(dan).^[1]

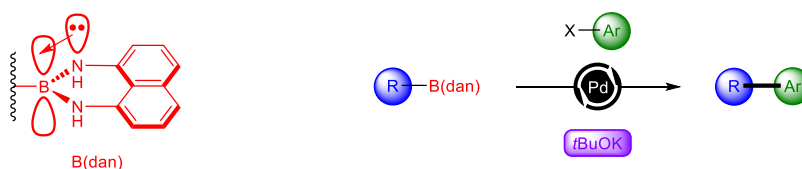


Figure 1

Herein we report that H–B(dan) serves as a convenient B(dan) electrophile in the reaction with various Grignard reagents, which provides a direct way of synthesizing diverse R–B(dan) derivatives in high yields.^[2] The Grignard reagents including aryl, alkyl, allyl, ethynyl or vinyl groups have proven to be efficient nucleophiles to catch boron center under mild and transition metal-free conditions (Figure 2). Furthermore, diverse 2-pyridyl–B(dan) were accessible as stable compounds according to a modified protocol by use of Turbo Grignard reagent (Figure 3).

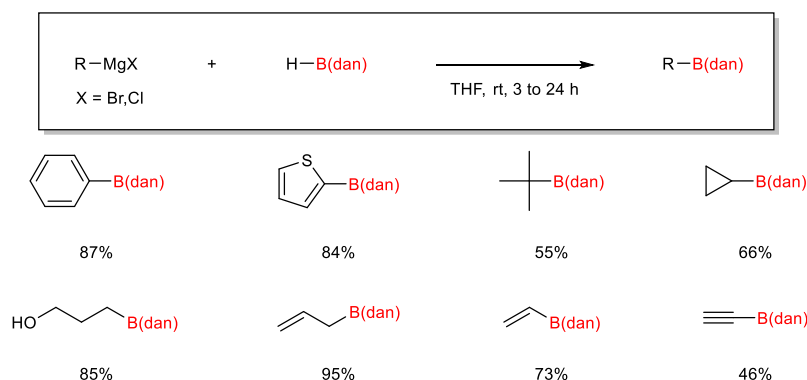


Figure 2

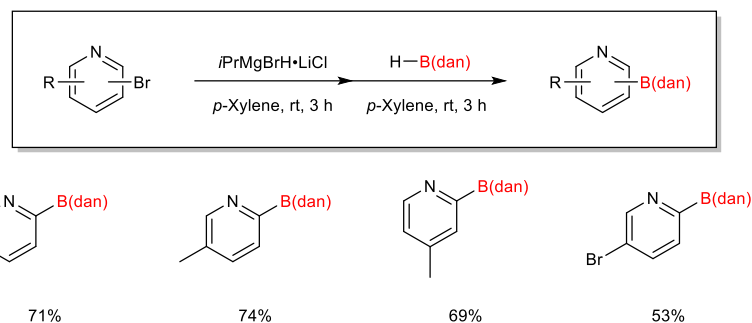


Figure 3

During the course of the reaction, we observed vigorous evolution of gas from the reaction mixture. On the assumption that the gas would be hydrogen, generated from a leaving group, a hydride (H-MgX) and a proton (H-N on the B(dan)), we carried out its trapping experiment by using *trans*-stilbene as a hydrogen acceptor in the presence of a palladium catalyst (Figure 4). A reduced product, 1,2-diphenylethane, was found to form in 88% yield, which verifies the evolved gas is indeed hydrogen. Based upon this, a plausible pathway for the B(dan) -installing reaction, where a hydride serves as a good leaving group, is depicted in Figure 5. In addition, this mechanism was further supported by Me-OTs or D_2O quenching reactions (Figures 6 and 7).

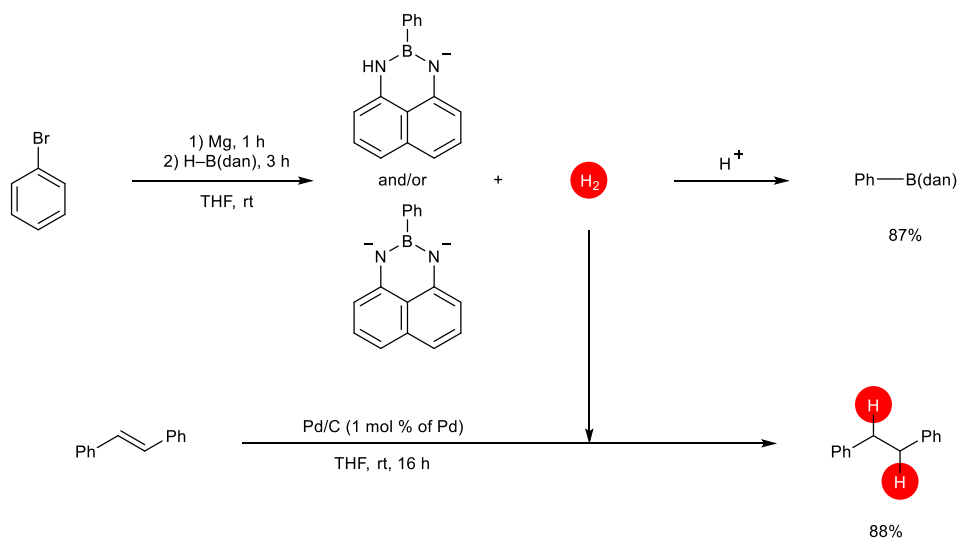


Figure 4

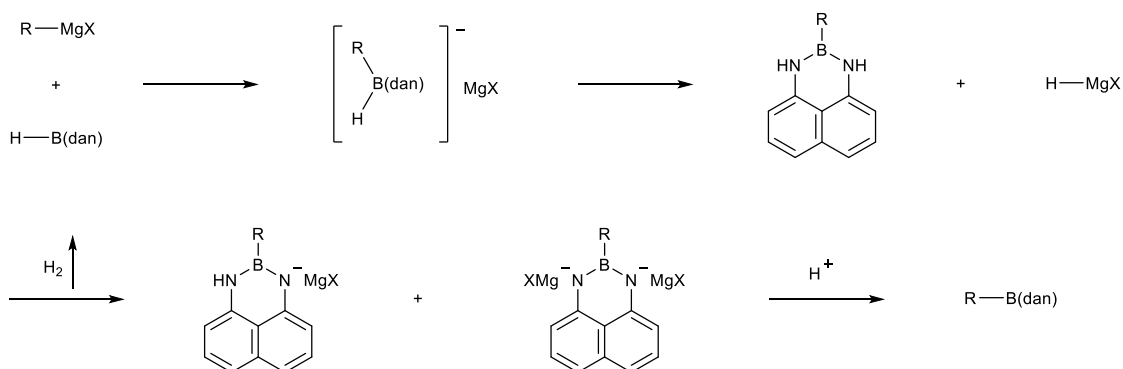


Figure 5

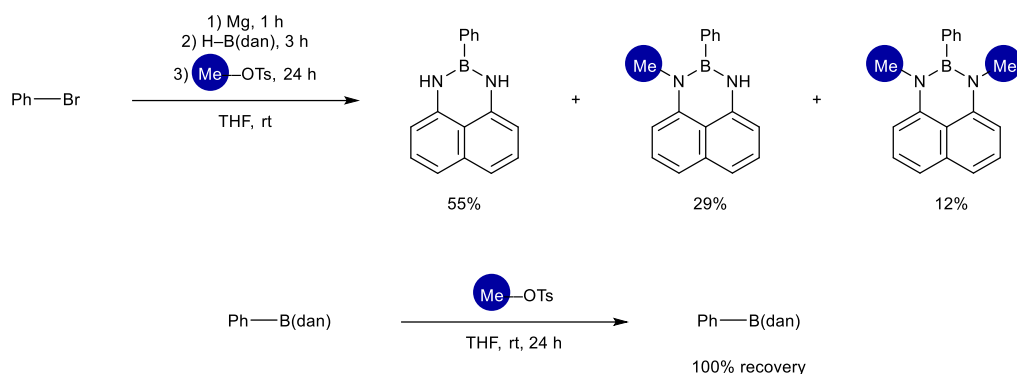


Figure 6

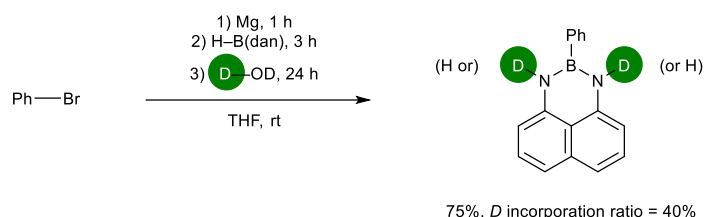


Figure 7

The synthetic utility of the present reaction was well demonstrated by the iterative SMC with 5-bromo-2-pyridyl-B(dan) obtained by our borylation reaction, which furnished oligoarene in 52% yield (Figure 8).

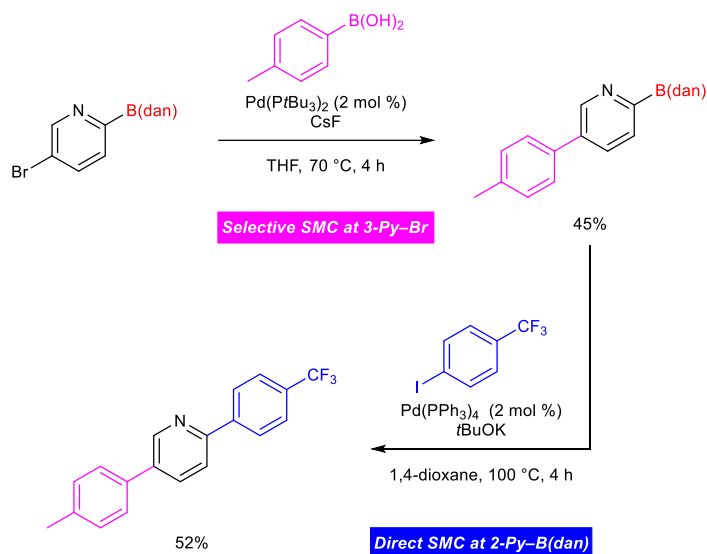


Figure 8

In conclusion, we have demonstrated that H-B(dan) can serve as a promising B(dan) electrophile for capturing such carbon nucleophiles as diverse Grignard reagents, leading to the convenient and practical method for synthesizing C(sp, sp² and sp³)-B(dan) of high synthetic utility under the transition metal-free conditions. Moreover, the reaction pathway has been found to include the evolution of H₂ via the deprotonation of the H-N on the B(dan) moiety with H-

MgX. Iterative cross coupling of 5-bromo-2-pyridyl–B(dan), synthesized by the present method, was also achieved.

References

- [1] H. Yoshida, M. Seki, S. Kamio, H. Tanaka, Y. Izumi, J. Li, I. Osaka, M. Abe, H. Andoh, T. Yajima, T. Tani, and T. Tsuchimoto, *ACS Catal.*, **2020**, *10*, 346.
- [2] J. Li, M. Seki, S. Kamio, and H. Yoshida, *Chem. Commun.*, **2020**, *56*, 6388.

3B2b

Spin-dependent quenching of triplet excitons by doublet centers in a nanoparticle

Penkov Sergey, Kucherenko Michael

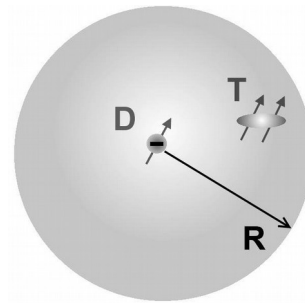
Orenburg University Center of Laser and Information Biophysics, Orenburg, Russia,

Abstract. *The process of spin-selective quenching of a triplet (T) exciton by a fixed spin doublet (D) center in an organic semiconductor nanoparticle is studied. Random walk of a T-exciton in a spherical nanoregion of a crystal or polymer globule were modeled based on the solution of the Neumann boundary-value diffusion problem. Calculations of the time dependences of the spin-nonselective rate of quenching of T-excitations have been performed for various values of the geometric and diffusion parameters. A strong influence of the nanoparticle size and the starting position of the T-exciton and doublet sink on the absolute value of the effect was found. It is shown that the obtained radial dependences of the magnetic field modulation of the quenching efficiency can be approximated by a superposition of two exponential curves.*

Key words: *organic semiconductor nanoparticles, molecular excitons, triplet-doublet quenching, Green's functions.*

The rapid development of the industry of light and photodiodes, as well as transistors based on organic semiconductors, where triplet molecular excitons interact with electrons and holes that initiate T-D quenching, has led to a new surge of interest in this type of spin-selective processes. An important fact is that it is triplet excitons in molecular crystals that can have a significant diffusion path [1, 2] due to long lifetimes, while being under confinement conditions within a nanoparticle serving as a nanoreactor for them. In this work, we consider the process of spin-selective quenching of a triplet exciton by a spin doublet in an

Fig. 1 Spherical nanoregion with a volume V_R for diffusion-reaction of T- and D-particles with a surface reflecting a T-particle - a sphere S_R .



organic semiconductor nanoparticle in the presence of a constant external magnetic field. A feature of this work is the diffusion of a triplet exciton (T) in the nanostructure of an organic semiconductor with injected current carriers, or a nanocrystal doped with radicals (D). The act of T-D quenching passes through the paired spin doublet D state ($S = 1/2$), which can be mixed with the paired quadruplet Q ($S = 3/2$) state of the T-D pair [3, 4]. The kinetics of the spin-selective quenching reaction of triplet electronic excitations by doublets can be described on the basis of the pair density operator $\hat{\rho}_{TD}(t)$ [4]. The diffusion of triplet excitons in a spherical nanoregion (Fig. 1) was described by a diffusion operator (in a spherical coordinate system r, φ, θ) [5]. Calculations of the spin-nonselective average rate $\chi(t | \mathbf{r}_1, \mathbf{r}_2')$ of the T – D quenching reaction were carried out on the basis of an expression similar to that obtained for the average rate of T – T annihilation of excitons [5, 6]. The degree of this influence and the nature of the

magnetic field dependences were determined through the ratio of the intensities of exciton phosphorescence $I_{ph}(B)/I_{ph}(0)$ in the presence of a magnetic field and in its absence on the basis of the following expression, which includes the rate constant of magnetically dependent TD quenching $K_{TD}(B)$, which was already used by us earlier in [6] with insignificant modifications. Here, in (1), the dimensionless factor C depends on the concentration of the quencher molecules and a number of kinetic parameters characterizing the system, and the radius vectors \mathbf{r}'_1 and \mathbf{r}'_2 determine the initial positions of the reagents - before the start of their wanderings and entering into a reaction. In the considered conditions of extinguishing, factor C is close to unity.

$$\gamma(B) = \frac{I_{ph}(B)}{I_{ph}(0)} = \frac{1 + C \int_0^{\infty} \langle \rho_D(t|0) \rangle \chi(t|\mathbf{r}'_1, \mathbf{r}'_2) dt}{1 + C \int_0^{\infty} \langle \rho_D(t|B) \rangle \chi(t|\mathbf{r}'_1, \mathbf{r}'_2) dt} \quad (1)$$

As noted above, in the course of the calculations performed, a strong increase in the amplitude of modulation of the magnetic field effect was found with a change in the radius of the nanosphere region towards its compaction. Thus, with a decrease in R from 20 nm to 8 nm, the relative increase in $\gamma(B)$ is ~ 4.6 times (Fig. 2a).

$$\gamma_{\max}(R) = \gamma_{\max}^0 \exp(-R/R_0) + \gamma_{\max}^1 \exp(-R/R_1) + \gamma_{\max}^{\text{offset}} \quad (2)$$

$$\gamma_{\max}(\rho) = \gamma_{\max}^0 \exp(-\rho/\rho_0) + \gamma_{\max}^{\text{offset}} \quad (3)$$

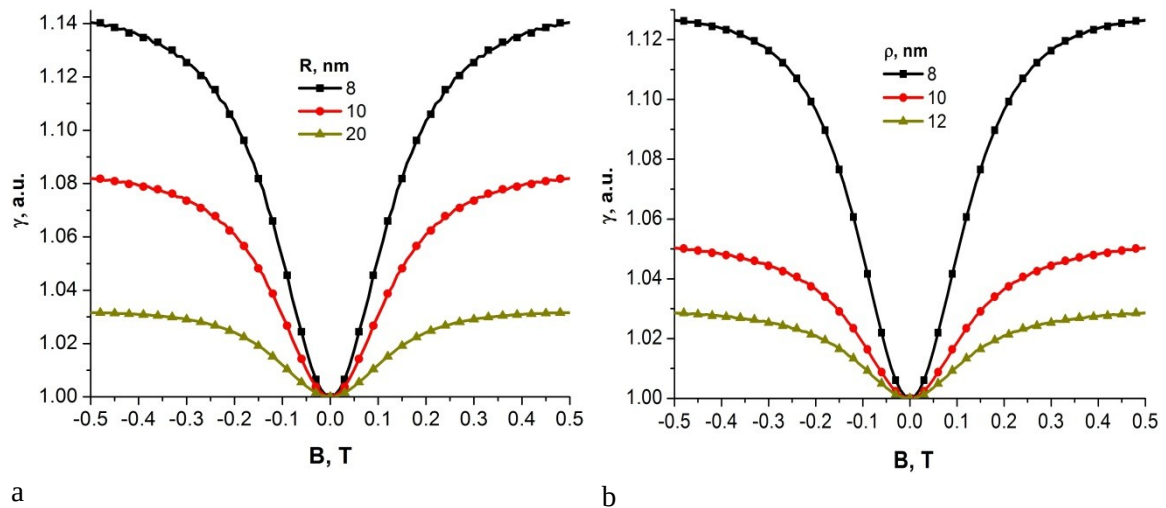
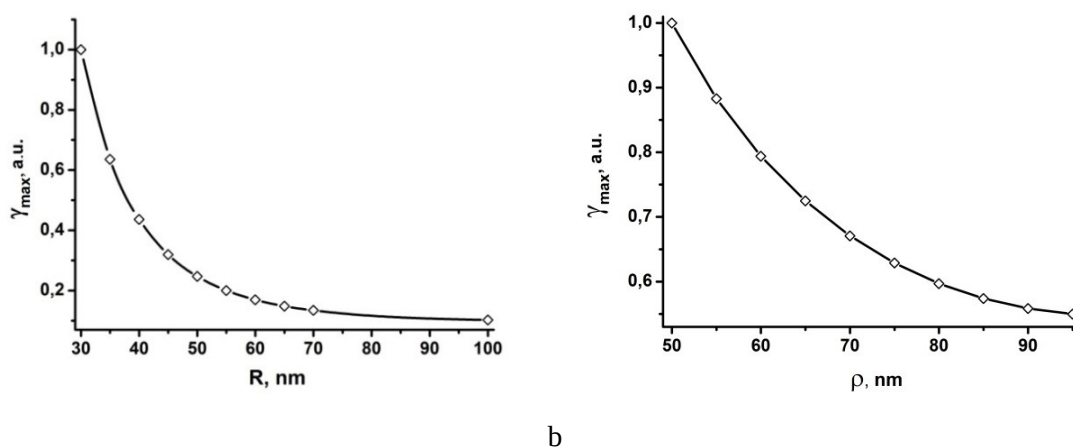


Fig. 2 Magnetic-field dependences of the rate of T-D quenching a) at different values of the radius R of the nanoparticle-reactor; b) at different values of the initial distance $\rho = |\mathbf{r}'_1 - \mathbf{r}'_2|$ between the reagents.

In order to reveal this dependence in more detail, calculations of magnetic field spectra were performed for the reactor size range of 30 - 100 nm. From the set of obtained spectra,

information on the depth of velocity modulation γ_{\max} was extracted to plot the dependence $\gamma_{\max}(R)$ (Fig. 3a, Table 1). The form of this dependence turned out to be close to exponential, but the coefficient of determination equal to one is achieved only when the curve is approximated by the sum of two exponentials (2). A similar behavior of the scale of the effect - the depth of modulation of the reaction rate is observed for the dependence of the magnetic field effect on the initial distance $\rho = |\mathbf{r}'_1 - \mathbf{r}'_2|$ between the reagents “triplet exciton - quencher” in a T – D pair. Thus, with a decrease in the initial distance between the reagents from 12 nm to 8 nm, the relative increase in the rate $\gamma(B)$ is ~ 4.1 times (Fig. 2b). The approximation of the dependence $\gamma_{\max}(\rho)$, with the coefficient of determination $\theta^2 = 0.99977$, allows the use of the exponential function (3) (Fig. 3b, Table 1). The results of calculations for various values of the parameters R and ρ allow us to speak of an increase in the magnetic sensitivity and the efficiency of the reaction of quenching a triplet exciton by a doublet acceptor-sink with a decrease in the values of these parameters.



a b
Fig. 3 Dependence of the amplitude of the magnetic field modulation of the T-D quenching rate a) from the radius R of the nanoparticle; b) on the starting distance $\rho = |\mathbf{r}'_1 - \mathbf{r}'_2|$ between the triplet exciton and the D quencher.

Table 1 - Coefficients for the approximating curves in Fig. 3 determined based on (2) and (3).

	γ_{\max}^0	γ_{\max}^1	γ_{\max}^{offst}	R_0 , nm	R_1 , nm	ρ_0 , nm	ρ_1 , nm
$\gamma_{\max}(R)$	76	5.1	0.1	5.5	14	-	-
$\gamma_{\max}(\rho)$	7.5	0	0.5	-	-	18.5	-

The results presented by the radial dependences of Figs. 3a and 3b demonstrate a higher amplitude of magnetic modulation of the rate of quenching of a triplet exciton by a doublet sink in the bulk of a nanoparticle as compared to the case of an unbounded medium. In this case, with a decrease in the nanoparticle size, the reaction efficiency increases, which leads to an increase in the modulation amplitude of the magnetic field spectra. In addition, a power-law approximation of the dependence by a function of hyperbolic type is obviously possible.

The study was carried out with the financial support of the Ministry of Science and Higher Education of the Russian Federation within the framework of scientific project No. FSGU-2020-0003.

References

1. P. Avakian, R.E. Merrifield. *Mol. Cryst.*, 5, N 1(1968) 37-77.
2. A. Suna. *Phys. Rev. B.*, 1. N 4 (1970) 1716-1738.
3. A.I. Shushin. *J. Chem. Phys.*, 101, N 10 (1994) 8747-8756.
4. M.G. Kucherenko, S.A. Penkov. *Chemical physics and mesoscopy*, 17, № 3 (2015) 437-448.
5. M.G. Kucherenko. *OSU bulletin*, 207, №7 (2017) C. 97.
6. M.G. Kucherenko, S.A. Penkov. *Chemical physics and mesoscopy*, 21, № 2 (2019) 278-289.

3B3b

Direct Suzuki–Miyaura Cross-Coupling Reactions of 1,8-Diaminonaphthalene (dan)-substituted Organoboron Compounds

Mikinao Koishi,¹ Hiroto Yoshida¹¹ Graduate School of Advanced Science and Engineering, Hiroshima University

Suzuki–Miyaura cross-coupling (SMC) reaction with organoboron compounds is indispensable carbon–carbon bond-forming reaction in modern synthetic organic chemistry because of their high versatility, ease of handling and low toxicity¹. Diverse organic molecules, which support our everyday life, such as losartan, an antihypertensive agent, boscalid, an agricultural chemical, and liquid crystalline compounds have been efficiently synthesized through SMC reaction (**Figure 1**).

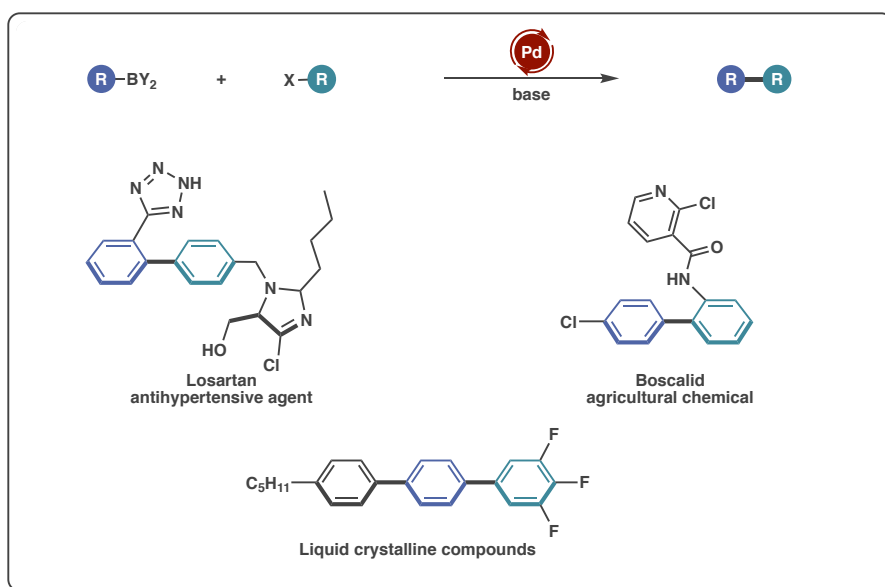


Figure 1. Diverse organic molecules synthesized through SMC reaction.

The catalytic cycle of SMC is commenced with oxidative addition of aryl halides to a Pd(0) complex to generate an Ar–Pd(II)–X species. Subsequent transmetalation between the resulting Ar–Pd(II)–X with an aryl borate derived from an aryl boron compound and a base gives an Ar–Pd(II)–Ar complex, which finally undergoes reductive elimination to form Ar–Ar with regeneration of the Pd(0) (**Figure 2**). The use of a base is crucial for the transmetalation to proceed, in which nucleophilicity of an aryl moiety on a boron center is enhanced by the formation of a borate through coordination of a base to a 2p empty orbital of the boron. In 2007, Suginome and co-workers reported site-selective SMC using two types of boron moieties with different Lewis acidities, one of whose substituents was 1,8-diaminonaphthalene (dan) (**Figure 3**).² The Lewis acidity of a dan-substituted boron moiety [B(dan)] is highly decreased because of its planar six-membered ring structure that leads to ideal B(sp²) hybridization, and sufficient electron donation from adjacent nitrogen atoms (**Figure 4**).

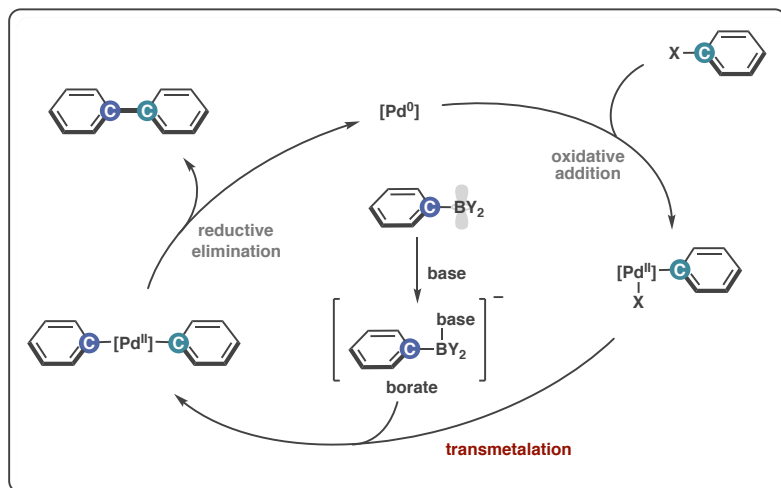


Figure 2. Catalytic cycle of SMC.

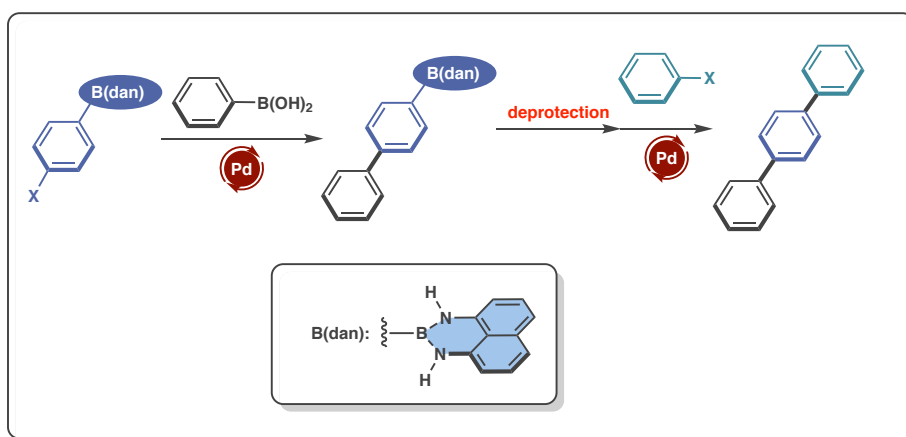


Figure 3. Site-selective SMC with two types of boron moieties.

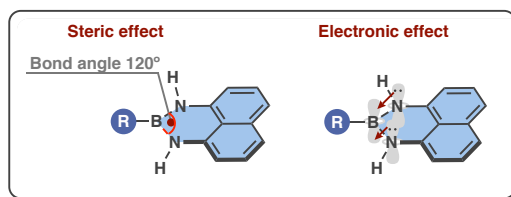


Figure 4. Lewis acidity-decreased B(dan).

The highly decreased Lewis acidity prevents the B(dan) moiety from forming a borate species even under strongly basic conditions (e.g. NaOH_{aq}), which results in its inactivity toward the transmetalation, and therefore deprotection of the B(dan) moiety under strongly acidic conditions was necessary in using for SMC until quite recently. On the other hand, dan-substituted organoboron compounds [(R-B(dan))] have one of the most air- and water-resistant properties. For example, 2-pyridylboronic acid is well-known to be unstable and difficult to handle under aqueous conditions with a half-life of only 26 seconds, being in stark contrast to extreme stability of 2-pyridyl-B(dan) (**Figure 5**).

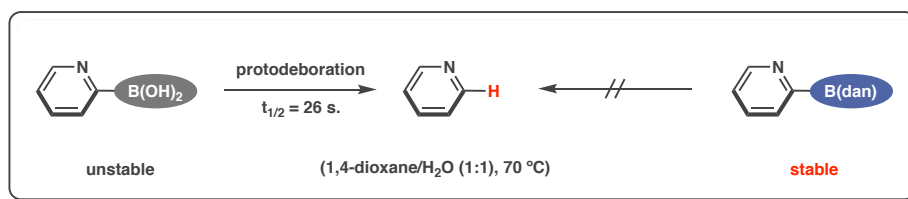


Figure 5. Enhanced stability of 2-pyridyl-B(dan).

Hence, SMC with 2-pyridylboron compounds has been recognized to be one of the most tough processes, and this is commonly known as “2-pyridyl problem”. In this context, we envisaged that the use of the highly stable 2-pyridyl-B(dan) may be a promising option for this problem, however, we have to deal with a dilemma between the decreased Lewis acidity-derived stability and inactivity toward SMC. In this study, we present unprecedented “direct” SMC using various R-B(dan) without any need for prior acidic deprotection.

As depicted below, the use of *t*BuOK as a base turned out to be the key to the direct SMC (Figures 6 and 7). The substrate scope on aryl-B(dan) has proven to be amply broad; 4-tolyl-Br was successfully cross-coupled with aryl-B(dan) having 2-*i*Pr (1), 4-CF₃ (2), irrespective of their electronic and steric environment. 9-Phenanthryl- (3) and various 2-pyridyl-B(dan) (4) were also convertible into the respective biaryls, and the chemo-selective SMC of 4-bromochlorobenzene (5) at the Aryl-Br bond over the Aryl-Cl bond took place solely. Furthermore, the use of XPhos as a supporting ligand enabled electron-rich and -deficient aryl chlorides to participate in the direct SMC, furnishing good to high yields of 6–8.

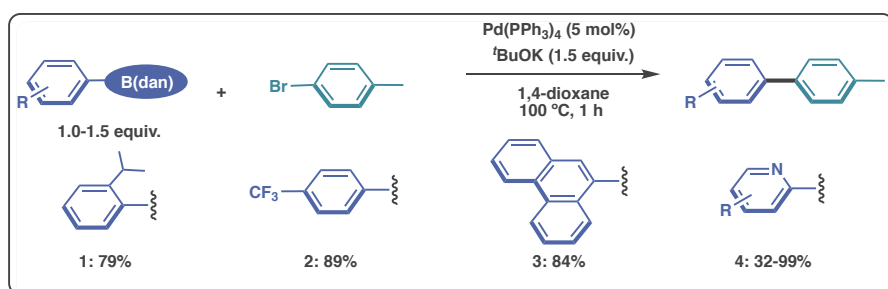


Figure 6. Substrate scope on aryl-B(dan).

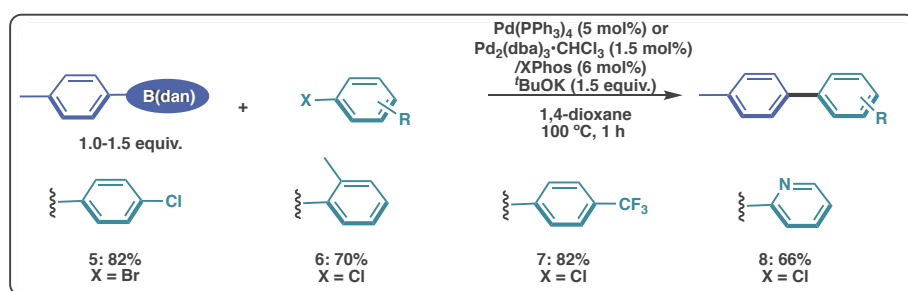


Figure 7. Substrate scope on aryl halides.

We then applied the above successful procedure to alkyl-B(dan) having C(sp³)-B bonds, which are considered to be much more robust than aryl-B(dan). Thus, we tried the direct SMC with cyclopropyl-B(dan) as a first trial, since its C-B(dan) bond holds a higher s-character than those

of usual unstrained alkyl–B(dan), which may lead to increase in reactivity. In fact, the reaction was found to smoothly proceed in 81% yield with 1-bromonaphthalene (**9**) as a coupling partner (**Figure 8**).

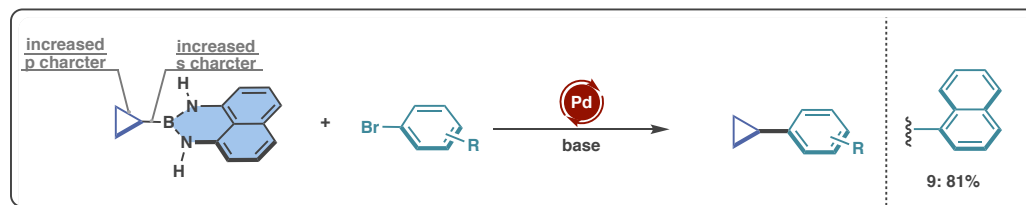


Figure 8. Direct SMC with cyclopropyl–B(dan).

In conclusion, we have demonstrated that various $C(sp^2/sp^3)$ –B(dan), which were previously thought to be totally inactive toward SMC because of their highly decreased Lewis acidity, can be effectively activated by using t BuOK as a base, without any need for acidic deprotection, which provides a promising solution to “2-pyridyl problem” (**Figure 9**).

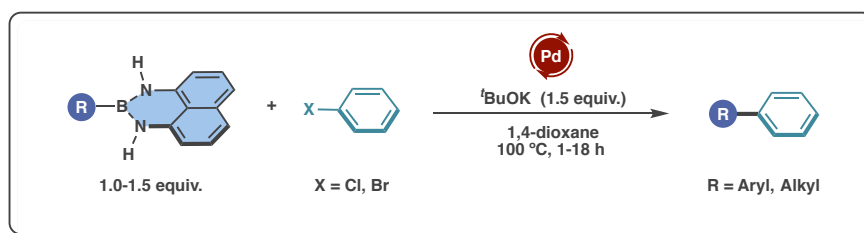


Figure 9. Summary.

Reference

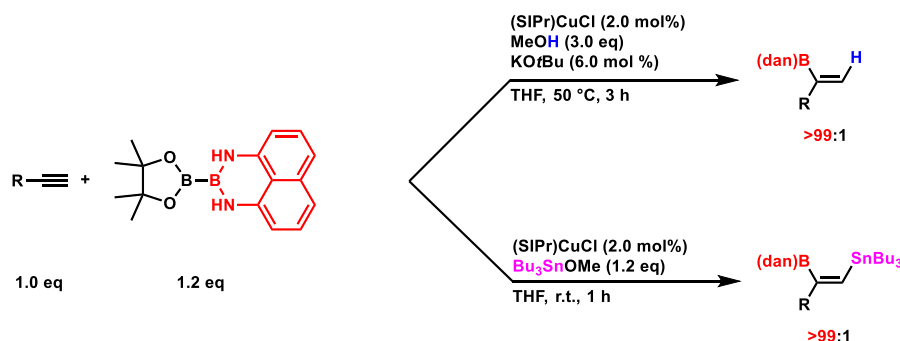
- (1) (a) Meijere, A., Brašė, S., Oestreich, M., Eds., Wiley-VCH: Weinheim, **2014**, 65–132. (b) Lennox, A. J. J., Lloyd-Jones, G. C., *Chem. Soc. Rev.* **2014**, *43*, 412–443.
- (2) Iwadate, N., Suginome, M., *Org. Lett.* **2009**, *11*, 1899–1902.
- (3) Yoshida, H., Seki, M., Kamio, S., Tanaka, H., Izumi, Y., Li, J., Osaka, I., Abe, M., Andou, H., Yajima, T., Tani, T., Tsuchimoto, T., *ACS Catal.* **2020**, *10*, 346–351.

3B4b

Internal Selective Borylations of Terminal Alkynes
with Lewis Acidity-Decreased Boron ReagentsTatsuya Kanasaki,¹ Hiroto Yoshida¹¹ Graduate School of Advanced Science and Engineering, Hiroshima University

Most borylation reactions of unsaturated carbon linkages of terminal alkynes and alkenes proceed with “terminal” selectivity, where a boron moiety is regioselectively installed into a less substituted carbon. A typical and well-recognized example is *anti*-Markovnikov selectivity in hydroboration, being due to inherent Lewis acidity of a boron center which favors generation of a more stable carbocationic transition state via the boron attachment at a terminal position. Hence, development of direct and efficient ways of installing boron functionalities into a more substituted carbon of terminal alkynes/alkenes with “internal” selectivity has continued to be a challenging subject in synthetic organic chemistry. We, therefore, envisaged that decreasing boron-Lewis acidity with a suitable substituent may alter the regiochemical trends to lead to internal selective borylations of terminal alkynes/alkenes. In this regard, our attention was focused on the use of 1,8-diaminonaphthalene (dan) as a substituent on a boron center, because the boron moiety, B(dan), was demonstrated to be unreactive under standard Suzuki–Miyaura coupling (SMC) conditions,^[1] owing to its highly decreased Lewis acidity.^[2]

We have already disclosed that internal selective hydroboration of terminal alkynes occurs almost in a perfect regioselectivity by use of dan-substituted unsymmetrical diboron [(pin)B–B(dan)] under (SIPr)CuCl catalysis, affording a variety of branched alkenylboron compounds straightforwardly (Scheme 1).^[3]



Scheme 1 Internal selective borylations with B(dan)

Furthermore, this system was extended to internal selective borylstannylation by simply changing a third component from MeOH to Bu₃SnOMe,^[4] however, the resulting alkenyl–B(dan) bonds cannot directly be utilized for carbon–carbon bond-forming processes via SMC as described above, which would impair their synthetic value to some extent. Then, we turned our attention to other Lewis acidity-decreased boron moieties, especially endowed with activity toward SMC as well as the internal selectivity, and found that an anthranilamide-substituted boron moiety [B(aam)] was well-suited for these purposes (Figure 1).

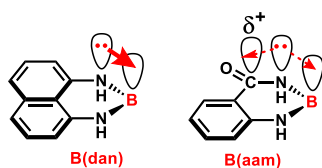
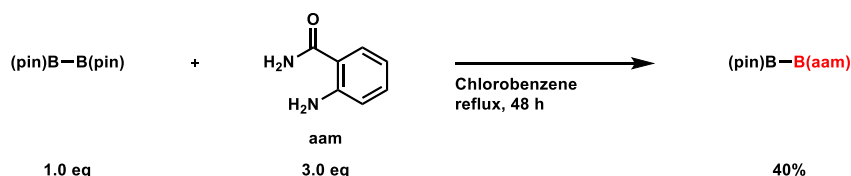


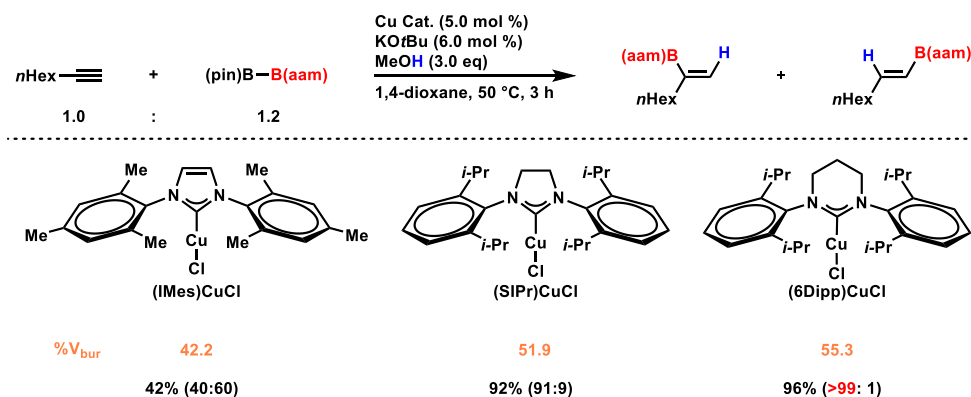
Figure 1 Structure of B(dan) and B(aam)

We synthesized aam-substituted unsymmetrical diboron [(pin)B-B(aam)]. A new B(aam)-containing diboron, (pin)B-B(aam), which could be utilized for internal selective borylations, was readily synthesized by treating (pin)B-B(pin) with aam in refluxing chlorobenzene (Scheme 2).^[5]



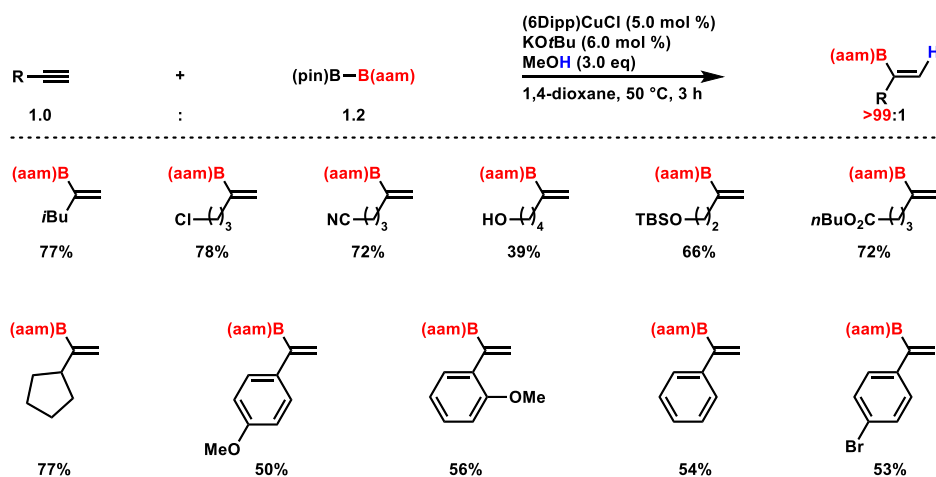
Scheme 2 Synthesis of (pin)B-B(aam)

With the aam-substituted unsymmetrical diboron in our hands, we carried out the three-component hydroboration with terminal alkynes and MeOH to observe chemoselective installation of the B(aam) moiety into a carbon-carbon triple bond (Scheme 3).



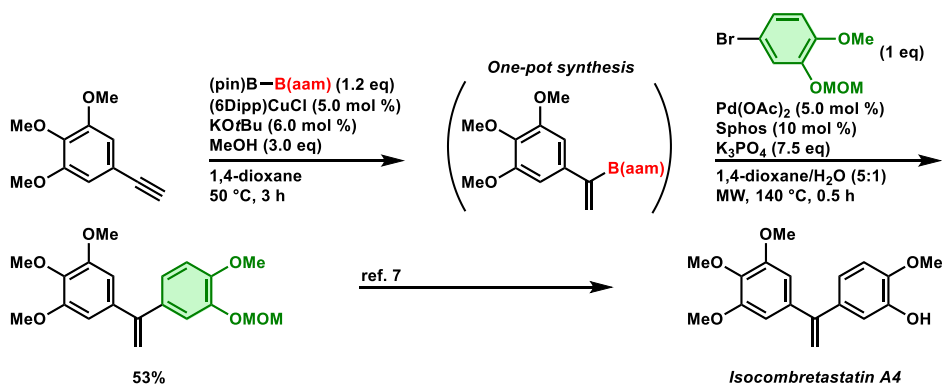
Scheme 3 Relationship between % V_{bur} and regioselectivity in hydroboration

It should be noted that the regioselectivities were strongly correlated to steric bulkiness of *N*-heterocyclic carbene (NHC) ligands employed; a branched alkenylboron compound was preferentially generated through the B(aam)-attachment to the internal carbon in the presence of (SIPr)CuCl (% V_{bur} = 51.9), whereas the reaction with less sterically congested (IMes)CuCl (% V_{bur} = 42.2) resulted in reversed regioselectivity. Moreover, the use of (6Dipp)CuCl, being more sterically demanding than (SIPr)CuCl as evident from its % V_{bur} value was found to be optimal, thus enabling diverse terminal alkynes to be converted into the respective alkenylboron compounds with perfect internal selectivity (Scheme 4).



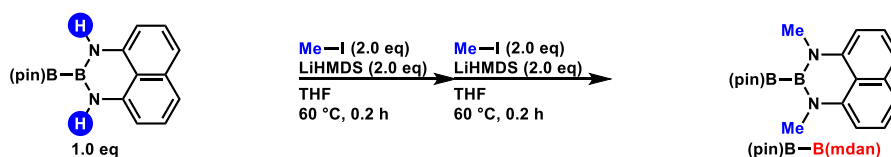
Scheme 4 Substrate scope of hydroboration with (pin)B–B(aam)

I performed a conversion reaction of alkenylboron in one spot synthetic utility of the internal borylation with B(aam) combined with direct SMC^[6] was demonstrated by formal total synthesis of isocombretastatin A4. Thus the hydroboration of 3,4,5-trimethoxyphenylacetylene gave a branched alkenylboron, which was convertible in one pot into a 1,1-diarylalkene by direct SMC at the B(aam) moiety. The resulting alkene was reported to be transformed into isocombretastatin A4 upon deprotection of the MOM group^[7] (Scheme 5).



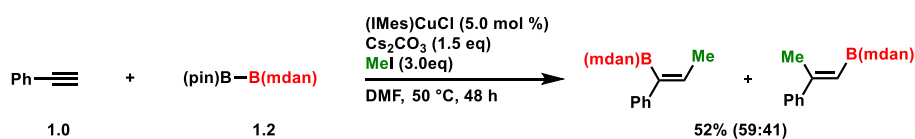
Scheme 5 Sequential internal borylation/direct SMC

Although the copper-catalyzed three-component borylations of alkynes have been also demonstrated to be applicable to carbon electrophiles to lead to a wide range of carboborations,^[8,9] there has been only one example on its internal selective version by use of *aliphatic* terminal alkynes.^[10] In addition, internal selective carboboration of more challenging *aromatic* terminal alkynes has no precedent, to the best of our knowledge. Based upon the above internal selective hydroborations even with aromatic terminal alkynes, we tried the carboborations of phenylacetylene with (pin)B–B(dan/aam), however only hydroboration occurred instead of desired carboboration. The results may imply that the hydrogens on the nitrogen atoms preferentially act as a proton source under the carboboration conditions, and thus we expected that this challenging carboboration may be feasible by replacing the H atoms on the nitrogen with methyl groups. As shown in Scheme 6, (pin)B–B(dan) was facily transformable into its dimethylated variant [(pin)B–B(mdan)] by sequentially reacting with lithium bis(trimethylsilyl)amide and iodomethane.



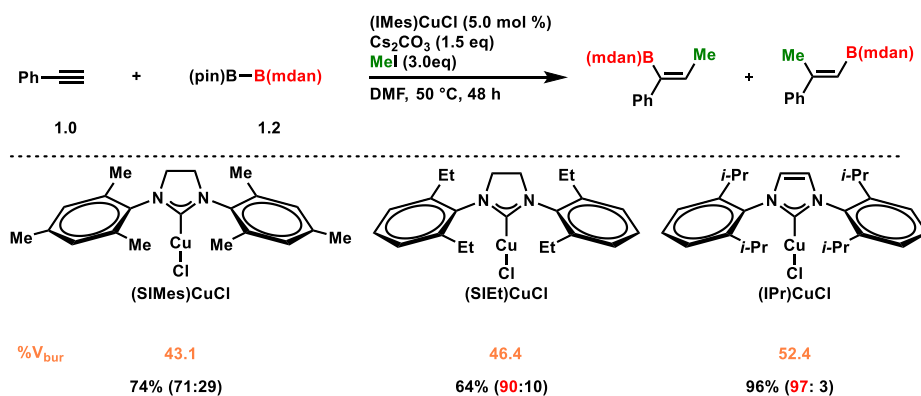
Scheme 6 Synthesis of (pin)B–B(mdan)

This novel unsymmetrical diboron turned out to be effective for the internal selective carboboration: the reaction with phenylacetylene and iodomethane catalyzed by (IMes)CuCl in the presence of Cs₂CO₃ mainly provided a carboboration product having the B(mdan) moiety at the internal carbon without formation of a hydroboration product, although the regioselectivity was unsatisfactory (Scheme 7).



Scheme 7 Carboboration with (pin)B–B(mdan)

It is worthy of note that the more sterically demanding NHC ligands (IMes < SIMes < SIET < IPr) were employed, the better internal regioselectivity was, albeit at the cost of the product yields. Studies on developing an optimal ligand that can achieve both of internal regioselectivity and yield are in progress (Scheme 8)



Scheme 8 Relationship between %V_{bur} and regioselectivity in carboboration

References

- [1] H. Noguchi, K. Hojo, M. Suginome, *J. Am. Chem. Soc.* **2007**, *129*, 758–759
- [2] H. Noguchi, T. Shioda, C.-M. Chou, M. Suginome, *Org. Lett.* **2008**, *10*, 377–380
- [3] H. Yoshida, Y. Takemoto, K. Takaki, *Chem. Commun.* **2014**, *50*, 8299–8302
- [4] H. Yoshida, Y. Takemoto, K. Takaki, *Chem. Commun.* **2015**, *51*, 6297–6300
- [5] S. Kamio, I. Kageyuki, I. Osaka, S. Hatano, M. Abe, H. Yoshida, *Chem. Commun.* **2018**, *54*, 9290–9293
- [6] S. Kamio, I. Kageyuki, I. Osaka, H. Yoshida, *Chem. Commun.* **2019**, *55*, 2624–2627

- [7] Y. Malysheva, S. Buchvalova, E. Svirshchevskaya, V. Fokin, A. Fedorov, *Synlett* **2013**, *14*, 1772–1776
- [8] R. Alfaro, A. Parra, J. Aleman, J. Ruano, M. Tortosa, *J. Am. Chem. Soc.* **2012**, *134*, 15165–15168
- [9] H. Yoshida, I. Kageyuki, K. Takaki, *Org. Lett.* **2013**, *15*, 952–955
- [10] W. Su, T. Gong, Q. Zhang, Q. Zhang, B. Xiao, Y. Fu, *ACS Catal.* **2016**, *6*, 6417–6421

Photoinactivation of *Salmonella* bacteria in organic dye solutions

Dorofeef D.V.,¹ Emel'yanova A.A.,² Galaktionova L.V.,² Letuta S.N.,¹
Nikiyan A.N.,¹ Tsyurko D.E.¹

Faculty

²Faculty of Chemistry and Biology, Orenburg State University

The search for new methods for the destruction of pathogenic microorganisms has become especially relevant after the appearance of a large number of reports on the development of bacterial resistance to traditional antimicrobial drugs [1]. The situation is complicated by the fact that many microorganisms at the growth stage form biofilms (BF), rather complexly organized microbial communities, the properties of which differ from those of plankton cells, especially in greater resistance to chemical and physical influences. It has now been established that microorganisms in their natural habitat exist mainly in the form of BF, which are highly resistant to antibodies, antibiotics and antiseptics.

An effective way of influencing living microorganisms is photodynamic treatment [2-3]. The attractiveness of this method of damage bacteria is that it is impossible to develop immunity against it. However, the photodynamic effect is applicable only for aerated peripheral layers of the BF [4], since sensitizers and exciting light practically do not penetrate into the deep layers of the BF.

The superficial layers of BF are metabolically active and may be primarily exposed to antibiotics. In this case, BF can be destroyed in layers by conventional antibiotics. However, antibiotic therapy only damages, but does not destroy, these cells. Continuous consumption of nutrients protects the underlying layers from the effects of drugs, thereby leaving them in a stage of resistant dormancy.

The difficulties of influencing bacteria in deep layers of solutions and BF can be overcome by acting on microorganisms mechanically, for example, by shock waves. Obviously, such an effect will be effective if the wave creates a pressure drop sufficient for destruction on a scale comparable to the size of a microorganism (~ 1-5 microns). Shock waves can be generated by fast (~ 1-10 ns) local heating of the medium. The length of the front of such a wave is ~ 1.5 μm , which at sufficient amplitude is detrimental to microorganisms.

It is convenient to carry out local heating with nanosecond laser pulses using intermediates - thermal sensitizers (TS). Organic molecules or nanoparticles with a high extinction coefficient and readily soluble in a medium with microorganisms can serve as TS. This work demonstrates damage to planktonic bacteria by shock waves generated by organic dyes. The mechanisms of bacterial inactivation are discussed.

Depending on the concentration of dye molecules and the power density of the excite radiation, bacteria in solutions may be damaged by one of the following mechanisms [5]:

- photodynamic damage by reactive oxygen species (ROS) arising as a result of quenching the triplet states of dyes (photosensitizers (PS)) by molecular oxygen (reactive singlet oxygen or anion radical is formed);

- hyperthermia due to the conversion of absorbed light energy into heat by dye molecules (TC) associated with the walls of bacteria or located inside cells;
- damage to the walls of bacteria or intracellular elements by shock waves generated during rapid local heating of the medium (if the temperature of the medium exceeds the boiling threshold, then shock waves are generated by the arising vapor bubbles);
- damage to wall of cells or intracellular substrate under nonradiative energy transfer from high electronically excited levels of sensitizers.

The objects of research were non-spore-bearing bacteria *Salmonella*. The xanthene dye erythrosine, which does not interacting with *Salmonella* bacteria and has a large (about unity) quantum yield to the triplet state, as a PS was used. The generation of singlet oxygen by erythrosine was recorded by the kinetics of delayed fluorescence arising from the annihilation of singlet oxygen migrating in solution with another dye molecule in the triplet state.

The dye rhodamine C with a low quantum yield to the triplet state, but actively interacting with bacteria, was chosen as TS. Rhodamine C molecules form dimers (or larger aggregates), the fluorescence quantum yield of which is much lower than that of monomers; therefore, a significant part of the absorbed energy is converted into heat directly in bacteria.

Note that any other molecules with similar properties can be used instead of the listed dyes.

The dye molecules were excited by the second harmonic pulses of a YAG:Nd laser. Excitation parameters: pulse duration 15 ns, excitation wavelength 532 nm, power density (0.1 - 50) MW/cm².

It has been shown that ROS, local hyperthermia and shock waves very effectively inactivate microorganisms. But we failed to establish reliably the damage to bacteria due to nonradiative energy transfer.

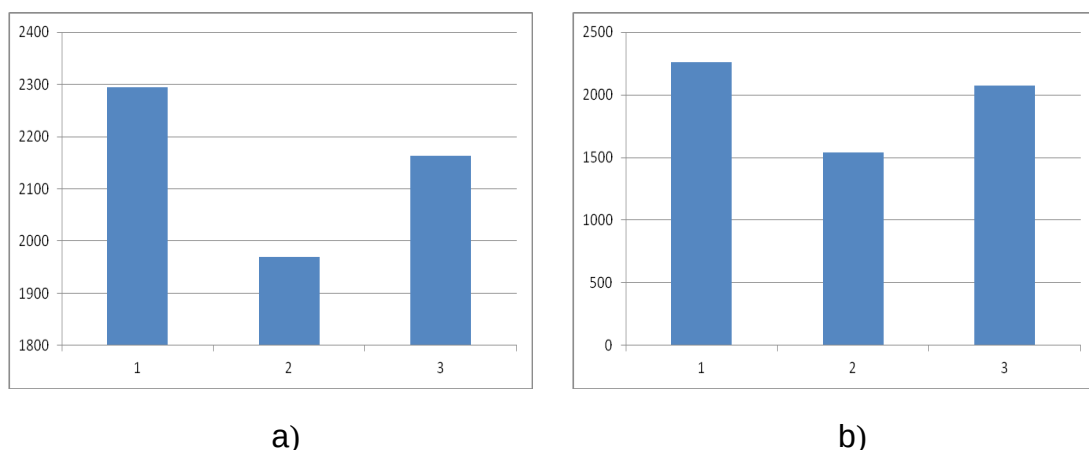


Figure: 1. CFU histograms of *Salmonella* cells taken from solutions in the presence of erythrosine (a) and rhodamine C (b) before and after irradiation with light of wavelength $\lambda = 532$ nm with a power density of 15 MW/cm².

To assess the survival of bacteria after exposure to visible light in the presence of sensitizers, the colony forming units (CFU) counting method was used. In fig. 1

shows histograms of CFU of Salmonella cells before irradiation (in Fig. 1, designated by the number 1) and after irradiation of solutions of bacteria and sensitizers with light of a wavelength of 532 nm with a power density of 15 MW/cm².

The CFU of bacteria taken directly from the excitation area (in Fig. 1 are designated by number 2), both in the case of using erythrosine and rhodamine C, sharply decrease in comparison with the unirradiated solution. Number 3 in Fig. 1 denotes CFU of cells taken from the same solution at a distance of 1.5 cm from the excitation area.

When the power density of the exciting radiation is higher than 10 MW/cm², as a result of stepwise absorption of two (or more) quanta by molecules, their highly excited electronic states (HEES) are effectively populated. Taking into account that in solvents with fully saturated bonds, the efficiency of energy transfer to the surrounding molecules is extremely low [6], and the quantum yield of fluorescence from HEES does not exceed 10⁻⁵ [7], the energy absorbed by the dye is almost completely transformed into heat within a few picoseconds. As a result of very rapid heat release, shock acoustic waves are formed in the medium, which damage bacteria not only directly in the excitation area, but also at a distance of up to several centimeters from one.

In a solution of erythrosine, in addition to shock waves directly in the excitation zone bacteria are damaged also by ROS, and in solutions of rhodamine C the dimers are formed, the nonradiative relaxation of which contributes to the local hyperthermia of cells. Therefore, the survival rate of bacteria taken from the excitation area is significantly lower than at a distance of 1.5 cm, where cells are damaged only by shock waves.

Study was supported by the Ministry of Education and Science of the Russian Federation, project number FSGU-2020-0003.

References

1. J. O'Neill Tackling a global health crisis: initial steps. The Review on Antimicrobial Resistance Chaired by Jim O'Neill, 2015.
2. M.R. Hamblin Antimicrobial photodynamic inactivation: a bright new technique to kill resistant microbes // *Curr Opin Microbiol*, 2016, 33, 67–73.
3. N. Kashef et al. Advances in antimicrobial photodynamic inactivation at the nanoscale. Review article. // *Nanophotonics*, 2017, 6(5), 853-879.
4. C.A. Fux, J.W. Costerton, P.S. Stewart, P. Stoodley Survival strategies of infectious biofilms // *Trends Microbiol*, 2005, 13, 34–40.
5. S.N. Letuta, S.N. Pashkevich, A.T. Ishemgulov and A.N. Nikiyan Photothermal Inactivation of Microorganisms under Relaxation of Highly Excited States of Sensitizers // *Biophysics*, 2020, 65 (4), 599–605.
6. V.A. Smirnov, V.B. Nazarov, V.I. Gerko, M.V. Alfimov Triplet-triplet energy transfer from aromatic to saturated compounds // *Chem. Phys. Lett.*, 1975, 34(3), 500-502.
7. Lin H.-B., Topp M.R. Low quantum-yield molecular fluorescence: polarization in khanthene dyes // *Chem. Phys. Lett.*, 1977, 47(3), 442-447.